IMPERIAL COLLEGE LONDON

CONTROLLED TRANSLATION AND OSCILLATION OF MICRO-BUBBLES NEAR A SURFACE IN AN ACOUSTIC STANDING WAVE FIELD

by

Xiaoyu Xi

A thesis submitted to the Imperial College London for the degree of

Doctor of Philosophy

Department of Mechanical Engineering

Imperial College London

London SW7 2AZ

August 2012

Declaration of originality

The material presented in this thesis 'Controlled translation and oscillation of microbubbles near a surface in an acoustic standing wave field' is entirely my own research work under the supervision of Dr. Frederic Cegla and Prof. Michael Lowe. All published and unpublished material referred in this thesis has been given full acknowledgement.

Name: Xiaoyu Xi

Date:

Signed:

Abstract

The removal of contamination particles from silicon wafers is critical in the semiconductor industry. Traditional cleaning techniques encounter difficulties in cleaning micro and nanometer-sized particles. A promising method that uses acoustically-driven micro-bubbles to clean contaminated surfaces has been reported. However, little is understood about the microscopic interaction between the micro-bubble and particle. This thesis explores the mechanism underlying the ultrasonic cleaning using micro-bubbles at the micrometer scale. The investigation was carried out from the perspective of bubble dynamics near a surface and bubble-particle interaction. Prior to contributing to the particle removal, micro-bubbles normally need to be transported to a target surface. The motion of a bubble was analyzed based on a force balance model for single and multi-bubble translations respectively. A good agreement is found between the observed bubble movement trajectories and the theoretical predictions. After arriving on a surface, a micro-bubble starts to disturb the flow field near the boundary through its oscillation. The characteristics of the flow field are closely related to the bubble oscillation modes. The influence of a wall on the change of bubble oscillation mode during its translation toward the boundary was studied. The relationship between bubble oscillation modes and the corresponding microstreaming around the bubble was established. The experimental results of bubble oscillation modes and the flow motion are quantitatively in good agreement with the simulation results. From a mechanic point of view, a possible ultrasonic cleaning mechanism is explained by exploring the relationship between different torques that are exerted on micro and sub-micrometer-sized particles. This estimation provides a qualitative insight into the ultrasonic cleaning process at a moderate pressure amplitude. The experimental investigation of the complicated particle detachment process requires improved test equipment to be developed in the future.

Acknowledgments

I would like to express my deepest thanks to my supervisors Dr. Frederic Cegla and Prof. Michael Lowe for their excellent guidance through this work. My thanks go to Prof. Peter Cawley for all the invaluable discussions. I am truly grateful to be given the opportunity to work at the Non-Destructive Testing group over the past three years.

My gratitude to Dr. Robert Mettin, Dr. Andrea Thiemann, Mr. Till Nowak from the Christian Doppler Laboratory for Cavitation and Micro-Erosion at the Georg-August-Universität Göttingen, Germany, and Dr. Frank Holsteyns and Mr. Alexander Lippert from the Lam Research AG, Austria are also expressed for their assistances with the experimental setup and all the wonderful time at Göttingen.

I would like to specially thank Dr. Zheng Fan, Dr. Jian Ma, and Dr. Shuofei Dong for their valuable advices not only on my work, but also on the life experience in London. I would also like to extend my thanks to all my current and former colleagues for their help, especially Dr. Thomas Clarke for his help with the finite element modelling, and Mr. David Tomlin for the construction of the test rig. My thanks go to Dr. Koucheng Zuo, Dr. Liliang Wang, Dr. Madis Ratassepp, Mr. Grzegorz Ptaszek, and Mr. Vatche Attarian for all the wonderful sports activities.

Finally, I could not enjoy my Ph.D so much without the unyielding support from my family, my father Naiyin Xi, my mother Shuqing Pan, and Miss. Zhenyu Yan. To them I dedicated this thesis.

Contents

List of Figures

Nomenclature

T	Kinetic energy
U	Potential energy
L	Lagrangian of a system
q	Generalized coordinate
ρ	Liquid density
φ	Velocity potential
V	Volume
r	Radial distance in polar coordinate system
θ	Angle in polar coordinate system
R	Bubble radius
p_{sc}	Scattered pressure
F_{ex}	External forces in the x axis
F_{ey}	External forces in the y axis
P_0	Hydrostatic pressure
R_0	Bubble radius at equilibrium
c	Sound speed
σ	Surface tension
γ	Polytropic exponent of gas
η	Shear viscosity of liquid
P_{sw}	Standing wave
P_a	Pressure amplitude
ω	Angular frequency
k	Wavenumber
d	Distance from a pressure anti-node
$F_{Bjerknes}$	General form of Bjerknes force
$F_{primary}$	Primary Bjerknes force
F_{buoy}	Buoyancy force
F_{vx}	Drag force in the x axis
F_{vy}	Drag force in the y axis
ρ_{gas}	Gas density

Continued on next oage...

– Continued from previous page

u	Liquid velocity
ψ	Streaming function
Ω	Vorticity
ϵ	Streaming amplitude
ϕ	Phase
$P_{threshold}$	Pressure threshold of non-spherical oscillation mode
f_{res}	Resonance frequency of a free bubble
f_n	Resonance frequency of a non-spherical oscillation mode
η_d	Dynamic viscosity
β_{tot}	Damping factor
V_3	Voltage
I_3	Current
A	Area
Z_{piezo}	Impedance of a piezoelectric disk
d_{piezo}	Thickness of a piezoelectric disk
k_{piezo}	Wavenumber of a piezoelectric disk
C_0	Clamped capacitance
h_{x1}	Transmitting constant
Z_L	Impedance of a matching layer
d_L	Thickness of a matching layer
k_L	Wavenumber of a matching layer
T	Transfer matrix
F_{vdw}	van der Waals force
F_p	Acoustic pressure force
F_{if}	Interface sweeping force
F_d	Dynamic pressure force
$R_{particle}$	Particle radius
A_H	Hamaker constant
$Z_{particle}$	Bubble-particle separation distance
$a_{particle}$	Particle-substrate contact radius
τ_a	Adhesion torque
τ_p	Acoustic pressure torque

Continued on next oage...

– Continued from previous page

τ_{if}	Interface sweeping torque
τ_d	Dynamic torque
τ_{ds}	Dynamic torque from the spherical oscillation
τ_{dn}	Dynamic torque from the non-spherical oscillation
d_{bp}	Bubble-particle separation distance

Chapter 1

Introduction

1.1 Motivation

The removal of contamination particles from silicon wafers is one of the major challenges in the semiconductor industry. It was estimated that over 50 % of yield losses in the semiconductor manufacturing were caused by micro-contaminations [1]. Conventional cleaning procedures, however, encounter difficulties in removing sub-micro and nanometer-sized particles for the new generation of micro-devices. The challenges mainly arise from two aspects: strong particle-substrate bonding of small contamination particles and the fragility of thin semiconductor structures.

It is well-known that the strength of particle-substrate adhesion is inversely proportional to the cube root of the particle diameter [2]. Thus, a smaller particle size results in a stronger bonding with a substrate. Also, sub-micro and nanometer-sized particles are protected by the boundary layer in the vicinity of a solid surface [3]. Fig. 1.1 shows that the flow velocity near a surface approximates to zero, and hence the forces acting on the particle also vanish. For conventional etching method, for example, the inefficient diffusion process within the boundary layer prohibits the interactions between the chemical cleaning solvent and contamination particles [4]. Violent cleaning procedures, however, are likely unsuccessful and perhaps even counterproductive. For example, the conventional high power megasonic cleaning process was reported to cause damage on semiconduction structures due to the weak

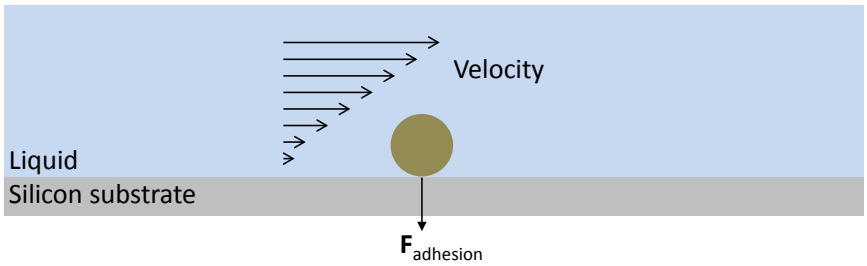

Figure 1.1: A diagram demonstrates the particle adhesion force and boundary layer condition near a substrate. A small particle is held onto a surface by a strong adhesion force. The liquid velocity in the vicinity of the substrate surface is almost zero. Small-sized contamination particles are protected by the boundary layer and particle adhesion force from being removed.

mechanical strength of the micro-devices [5].

To overcome the mentioned issues, many strategies have been proposed for the cleaning of small size particles over the past two decades [6–12], and one of them uses acoustically-driven micro-bubbles as the cleaning agent. The advantages of micro-bubble assisted cleaning methods are easy utilization, no introduction of new contaminations, and low cost [13, 14]. However, apart from the macroscopic cleaning effects [5, 15–23], little is known about the microscopic mechanism underlying the bubble-particle interactions owing to the complicated bubble dynamics near a surface and limited optical investigation techniques. Only recently, the removal torques exerted on contamination particles [24] and the dynamic features of micro-bubble induced cleaning flow [25] were reported. It was, hence, the purpose of this thesis to explore the mechanism of ultrasonic cleaning at the micrometer scale.

Usually, micro-bubbles are generated in the far field away from a surface. In order to achieve the cleaning effect, the micro-bubbles are first required to be transported to an appointed target region in a controlled manner. Additionally, it is commonly accepted that though cavitation bubbles could assist in many bioengineering applications with elastic membranes [26–34], they could also cause erosions and fatal damage on surfaces [35–40]. An example of the interaction between cavitation bubbles and a thin aluminium foil is displayed in Fig. 1.2. The cavitation bubbles were provided by a conventional ultrasonic cleaner (2510E-MT Bransonic ultrasonic cleaner, Branson Ultrasonics Corporation, USA). A clear damage effect (in the form of holes) is seen on the foil surface after the ultrasonic treatment. Thus, this thesis

focuses on the behavior of moderately oscillating bubbles instead. The investigation of ultrasonic cleaning mechanism in this work was, then, carried out in two steps: the first one was to study the bubble translation mechanism under various conditions; the second one was to explore the bubble behavior near a surface and the influence of bubble induced hydrodynamic forces on the particle removal process (Fig. 1.3).

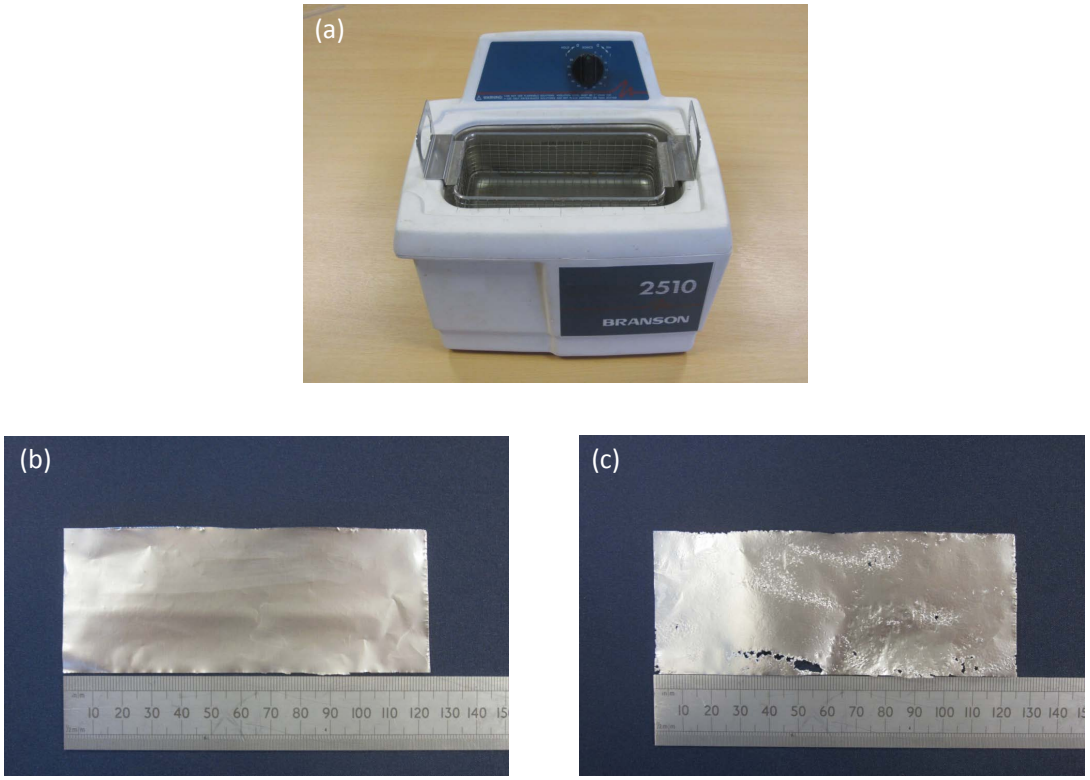

Figure 1.2: An example of erosions caused on a thin aluminium foil (thickness of 0.01 mm) after a violent ultrasonic treatment. (a) a commercial ultrasonic cleaner (2510E-MT Bransonic ultrasonic cleaner, Branson Ultrasonics Corporation, USA). (b) a piece of intact thin aluminium foil before the ultrasonic operation. (c) damaged sample after being inserted into the ultrasonic cleaner. The operation time was 5 minutes.

The motion of an object is the outcome of the competition of different forces exerted on it. In a bulk medium with a weak sound field, the bubble's motion is influenced by the force generated by the acoustic field (primary Bjerknes force), the buoyancy force from the surrounding liquid and the viscous drag force. A gas bubble driven below its resonance frequency moves towards the pressure anti-node, while a bubble driven above its resonance frequency moves towards the pressure node instead. This effect is attributed to the primary Bjerknes force on a bubble and has been studied

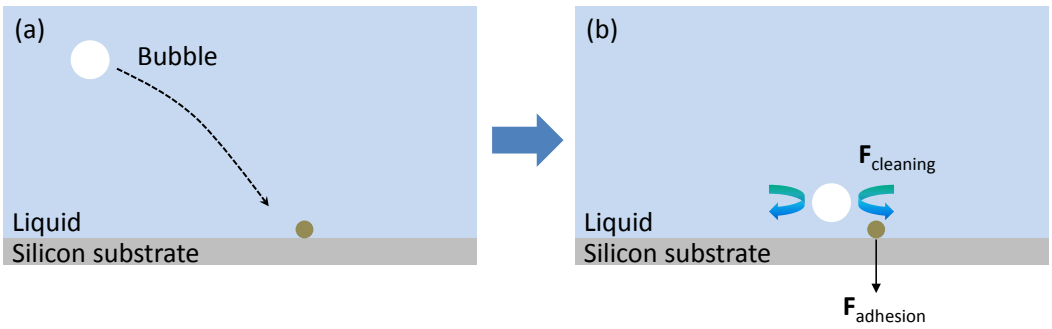

Figure 1.3: A schematic diagram of the ultrasonic cleaning mechanism study. (a) the first step is to investigate the bubble translation mechanism. (b) the second step is to explore the bubble behavior and bubble-particle interactions, particularly the relationship between cleaning forces and particle adhesion force.

extensively by many authors [41–46]. On the other hand, in a high intensity acoustic field, two types of bubble translational instabilities have been recognized. The first one, also known as 'dancing' motion, refers to the bubble erratic behaviors when bubbles travel in a sound field. It was first observed by Gaines [47], Strasberg et al [48] and Eller et al [49] and later on investigated by Mei et al [50], Feng et al [51] and Doinikov [52] in more detail. A generally accepted explanation for this phenomenon attributes the bubble surface oscillation modes, which come into existence once the acoustic pressure amplitude exceeds a threshold value, as the main cause. The second type of translational instability results from the fact that the primary Bjerknes force acting on a bubble changes sign at a higher acoustic pressure [53, 54]. This change is a result of the increased phase shift between bubble volumetric pulsation and the driving pressure. This behavior was reported by Miller [55], Khanna et al [56], and Kuznetsova et al [57]. Theoretical investigations were carried out by Abe et al [58], Watanabe et al [59] and more recently were extended by Doinikov [60] and Mettin et al [61].

Apart from the bulk medium case, a bubble's motion is also influenced by the nearby boundary conditions and neighboring bubbles in a multi-bubble environment. The boundaries and neighboring bubbles exert secondary Bjerknes forces on the target bubble. The secondary Bjerknes force takes significant effect between two nearby bubbles because the force is inversely proportional to the square of the separation distance between two bubbles [62, 63]. A bubble can exert either an attractive or a repulsive secondary Bjerknes force on the other one, depending on the driving

frequency and the bubble sizes [64]. There is a lack, however, of experimental works on the bubble translation in a multi-bubble environment and the mechanism of multi-bubble transportation has not yet been completely understood. Moreover, unlike solid particles, the translation of a bubble is coupled to its oscillation which makes the bubble dynamics even more complicated.

The study of bubble oscillation dates back to the beginning of last century when Rayleigh firstly derived his famous equation which explains the bubble radial pulsation in an unbounded medium [65]. After that, the bubble oscillation has been extensively investigated theoretically and experimentally. Two types of bubble oscillation modes have been recognized: spherical and non-spherical surface pulsations. At a low pressure amplitude, a bubble undergoes a spherical pulsation and the corresponding wall displacement results in a monopole emission in the far field. Plesset [66] expanded Rayleigh's equation by including the effects of liquid viscosity and surface tension. Later on, Gilmore [67] considered the sound radiation from a bubble surface into a liquid medium and proposed a more advanced model to explain the bubble spherical oscillation at a large pressure amplitude. Keller et al [68] also investigated the spherical pulsation at a large pressure amplitude, but their work introduced a retarded time into the equation. Experimental work has also been carried out by many researchers. Direct observations of bubble oscillation were made by Holt et al [69], Tian et al [70], Geisler et al [71], Gompf et al [72], and Matula et al [73]. More comprehensive reviews on this topic have been given by Plesset et al [74], Feng et al [75], and more recently by Lauterborn et al [76].

In addition to the exploration of spherical pulsation, extensive effort has also been devoted to investigate the non-spherical behavior owing to its importance in understanding bubble sonoluminescence. The theoretical analysis of spherical shape stability was first given by Plesset [77]. The viscous effect in the vicinity of a bubble wall was considered by Prosperetti and co-workers [78–80]. However, due to the intrinsic difficulty in calculating a full scale viscous stress, a boundary layer approximation solution was developed which only takes the local vorticity into account [81–83]. This solution has been widely used to explain the bubble break-up and sonoluminescence [84]. Moreover, the non-spherical oscillation can also be coupled to the translation motion. This coupling effect between different modes was reported

by Longuet-Higgins [85, 86], Feng et al [51, 75], Shaw [87], and Doinikov [52]. Numerous experiments were also carried out to visualize the non-spherical oscillation of micro-bubbles, particularly the non-spherical shapes of Ultrasound Contrast Agents (UCAs) [88–93].

Various oscillation modes result in different characteristics of the flow field around a bubble, consequently different removal forces are exerted on contamination particles. A bubble's surface displacement normally leads to a flow motion in the vicinity of its wall. The disturbed flow motion, hence, is transmitted to a solid surface to which particles are attached. The local velocity creates a pressure gradient on particles and various forms of this force were reported in the literature [94–99]. The study of cleaning mechanism is now converted to understand the flow behavior near the micro-bubbles and particles. It is well-known that the flow velocity can be expressed in a form of Stokes streaming function [100], and the rectified component of the flow motion is known as microstreaming. Microstreaming is important in mass transfer [101], electrodeposition [102], and metal erosion [103]. Extensive theoretical investigations of microstreaming generated by various surface shapes have been carried out over the past few decades. The viscous streaming from a sphere with Reynolds number smaller than unity was given by Riley [104]. Amin et al [105] considered the case where the Reynolds number is larger than unity. For a gaseous cavity or a spherical solid particle, its lateral oscillation and the induced streaming were discussed by Davidson et al [106] and Zhao et al [107]. Both of their works assumed the spherical shape remained unchanged. This assumption, however, was pointed out by Longuet-Higgins [108] not to be accurate in representing the microstreaming from a real cavitation bubble because the microstreaming is significantly enhanced by the additional radial oscillation and the streaming pattern is radically changed. Wu et al [109] and Liu et al [110] also investigated the microstreaming from an isolated bubble with radial oscillation and lateral translation. Their works, however, are only valid for fluids with very low viscosity and were extended by Doinikov [111] for more general cases. More details of the theoretical studies have been summarized in several reviews [112–114].

In contrast to the numerous theoretical studies, only few experimental reports aiming to visualize the microstreaming are found in the literature. Kolb et al [115] and

Elder [116] are among the first few to directly observe the flow around a cavitation bubble sitting on a surface. More recently, with more advanced optical systems, detailed observations of streaming patterns become possible. The microstreaming around cavitation bubbles were reported by Tho et al [117], Collis et al [118] and Kröninger [119] using Particle Image Velocimetry (PIV). Apart from the cavitation microstreaming, microstreaming around moderately oscillating bubbles are investigated by more and more researchers. Marmottant et al explored the microstreaming from an spherically oscillating bubble at a low pressure amplitude [120, 121]. The flow fields around Ultrasound Contrast Agents (UCAs) were observed by Gomley et al [122]. However, the direct relationship between microstreaming (or cleaning force) and the bubble oscillation, particularly the non-spherical oscillation mode, has not yet been quantified. Moreover, little is known about the influence of the bubble induced microstreaming on the particle removal process.

In general, the study of the mechanism underlying ultrasonic cleaning requires the investigation of bubble dynamics near a surface and bubble induced hydrodynamic forces on contamination particles. In a bulk medium, a bubble's motion is controlled by the primary Bjerknes force, buoyancy force and drag force. When the bubble approaches a surface, it also experiences a secondary Bjerknes force from the boundary. Meanwhile, the bubble translation is closely linked to its surface oscillation. Different oscillation modes result in different flow motion around the bubble, and consequently generate different hydrodynamic forces on the particles.

1.2 Objective of the thesis

As mentioned in the previous section, in real life application, micro-bubbles are normally generated in the far field from a contaminated substrate, and hence need to be transported to the target surface before contributing to the particle removal. The bubble motion is not only influenced by the acoustic field, but also by the boundary condition and neighboring bubbles which complicate the analysis of bubble translation. However, the mechanism of bubble transportation near a surface in an acoustic standing wave field has not been fully understood. After arriving on a surface, a bubble's oscillation mode determines the characteristics of the flow

field around it. However, the influence of a wall on the bubble oscillation mode, particularly the non-spherical oscillation mode, is still unknown yet. Meanwhile, the cleaning hydrodynamic forces exerted on contamination particles are also closely related to the bubble oscillation modes. However, the influence of bubble induced cleaning forces on the particle detachment process has not been fully explained.

Therefore, the primary objective of this thesis is to explain the mechanism of ultrasonic cleaning at the micrometer scale. This was addressed from the perspective of bubble dynamics near a surface and bubble induced hydrodynamic forces on the contamination particles. In this thesis, a multi-layered resonator was designed to control the bubble motion within an acoustic standing wave field. Using the test rig, it was possible to control the bubble motion near a wall in a controlled manner, and hence study the interaction between bubble and particle in more detail. The main issues to be investigated in this thesis are:

- The mechanisms of single bubble and multi-bubble translations near a surface.
- The bubble behavior near a surface and the characteristics of the flow motion around a bubble.
- The influence of bubble induced hydrodynamic forces on the particle detachment process.

The multi-layered resonator was fabricated and tested by Xiaoyu Xi at the Non-destructive testing group, Imperial College London. The optical observations of bubble dynamics were carried out by Xiaoyu Xi at the Christian Doppler Laboratory for Cavitation and Micro-Erosion at the Georg-August-Universität Göttingen where a high speed camera system could be used.

1.3 Outline of the thesis

Chapter 2 presents the design of an acoustic standing wave field using a multi-layered stack. To control the bubble motion in a liquid medium, an acoustic standing wave field is designed based on a one-dimensional transducer model. The impedance and

pressure distribution along a multi-layered stack are successfully simulated by the transducer model.

Chapter 3 reviews the theoretical background of bubble translation in a liquid medium. The bubble translational behavior is governed by the translation equation that is derived from the Lagrangian formulism and the modified Keller-Miksis equation. The influence of a nearby wall on the translation and radial equations is shown.

In chapter 4, the mechanism of single bubble translation is shown. The designed test rig, which creates a one-dimensional uniform pressure field across the cross section of the whole stack, is used for testing the effects of an acoustic field on the bubble motion. The bubble trajectories obtained by a high speed camera system are in good agreement with the predictions of bubble translation model. The influence of external factors, such as different pressure amplitudes or different bubble sizes, on the bubble translational trajectory, is also discussed.

Chapter 5 furthers the bubble translation study by exploring the mechanism of multi-bubble transportation. The collective bubble dynamics near a surface in a weak acoustic standing wave field is shown. The bubble motions that are modeled by a coupled modified Keller-Miksis equation and a bubble translation equation are in good agreement with the experimental results. A parametric study that aims to explore the influence of pressure amplitude and bubble size on the multi-bubble translation is given.

Chapter 6 studies the bubble behavior near a surface, and analyzes the characteristics of the flow field around a bubble. Various bubble oscillation modes are shown under different conditions using the high speed camera system. The conditions to excite the non-spherical bubble oscillation are identified. The microstreaming around an oscillating bubble is investigated by using Particle Image Velocimetry. The observed far-field microstreaming shows good agreement with the theoretical predictions that are derived based on the modified Navier-Stokes equation.

Chapter 7 explains a possible cleaning mechanism based on a linear torque balance model. The feasibility of using the test cell for ultrasonic cleaning is verified. By analyzing the relationship between different torques exerted on a particle, the influential

factors that are responsible for the particle detachment in the near field are found. These simulation results give a qualitative insight into the the bubble-particle interaction in the linear regime. The experimental investigation of the bubble-particle interaction, especially the direct measurement of microstreaming around the particles and the particle-substrate bonding force at the nanometer scale, requires improved equipment to be developed in the future.

The main findings of this thesis and suggestions for future work are summarized in chapter 8.

All of the video results of bubble dynamics shown in this thesis are provided on the attached CD.

Chapter 2

Acoustic standing wave generator

To investigate the bubble translation and oscillation, a bubble's motion should be manipulated in a controlled manner. However, little effort has been devoted to developing a reliable test rig for bubble motion control. In this chapter, the design and construction of a multi-layered resonator that was used to transport bubbles towards a target surface is presented. Although similar resonator devices have been used by many authors to study particle manipulation [123–127] and cell localization [128–131], they have not been applied in the study of ultrasonic cleaning processes. The characteristics of the acoustic field is predicted by a one dimensional transducer model. The experimental validation of this model is also shown.

2.1 Theory

In this thesis, the bubble motion is controlled by an acoustic standing wave field that was fabricated based on a layered resonator. The main part of the resonator is a piezoelectric material which is bonded to several matching layers. Acoustical standing waves can be generated in a liquid layer (matching layer) which is terminated by a reflector.

A one-dimensional equivalent network model (1D model) has been widely used for predicting the acoustic responses of such multi-layered structures [132–134]. In the 1D model, a transducer is treated as a purely electrical circuit and can be

analyzed by conventional circuit analysis techniques. The characteristics of a sound field including pressure profile and amplitude are calculated based on the properties of the matching layers. At a certain frequency, the pressure distribution of an acoustic field can then be determined. The 1D model has been verified to accurately predict acoustic responses of multi-layered structures within the first few resonance frequencies.

The basic idea of this approach is shown in Fig. 2.1. The piezoelectric layer is represented as a three-port electrical network which is described by the matrix Eq.2.1 [135].

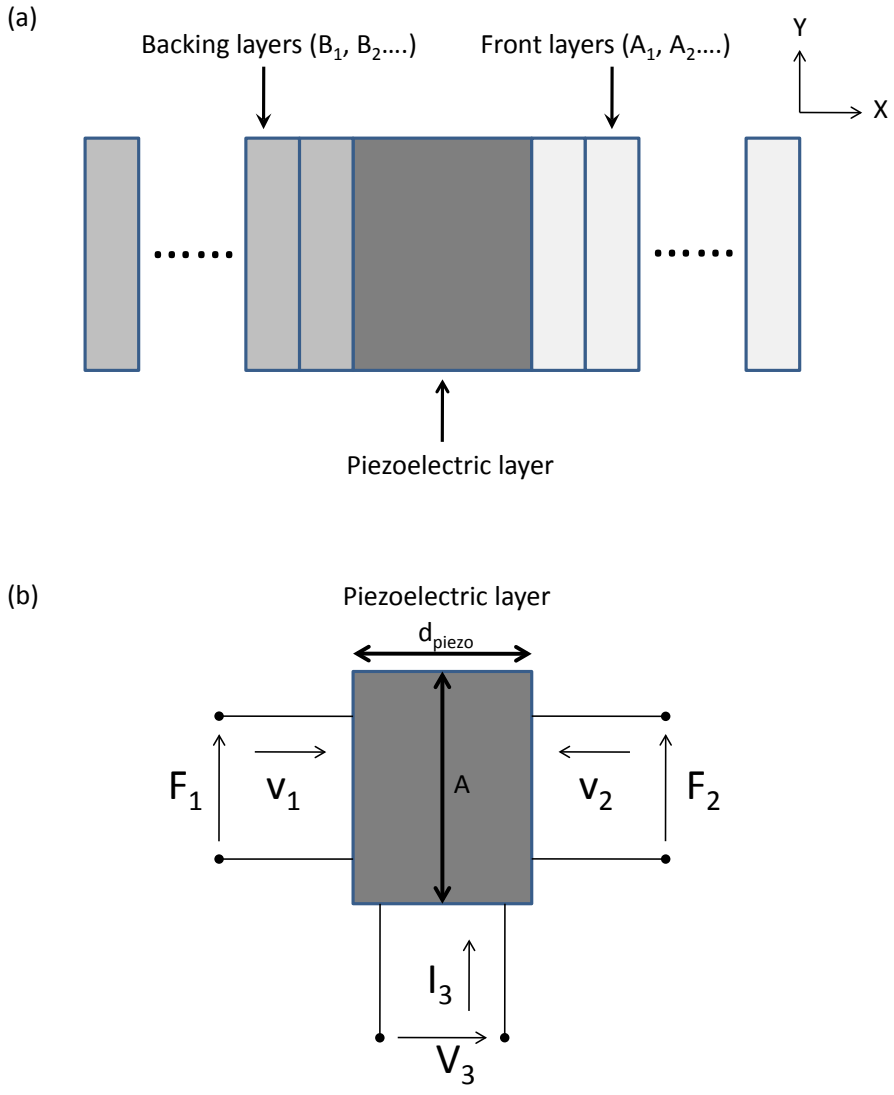

Figure 2.1: (a) A diagram of a physical acoustic standing wave generator; (b) The piezoelectric layer is represented by a three-port network.

$$\begin{pmatrix} F_1 \\ F_2 \\ V_3 \end{pmatrix} = -i \begin{pmatrix} AZ_{piezo}cotk_{piezo}d_{piezo} & AZ_{piezo}csck_{piezo}d_{piezo} & h_{x1}/\omega \\ AZ_{piezo}csck_{piezo}d_{piezo} & AZ_{piezo}cotk_{piezo}d_{piezo} & h_{x1}/\omega \\ h_{x1}/\omega & h_{x1}/\omega & 1/\omega C_0 \end{pmatrix} \begin{pmatrix} v_1 \\ v_2 \\ I_3 \end{pmatrix} \quad (2.1)$$

where F_i and v_i (i is the index) are the force and particle velocity at the two acoustic ports. V_3 and I_3 are the voltage and current applied to the electric port of the piezoelectric material. A, Z_{piezo}, d_{piezo}, and k_{piezo} are the area, characteristic impedance, thickness, and acoustic wave number of the piezoelectric layer respectively. h_{x1} is the transmitting constant of the piezoelectric material in the x direction (longitudinal direction). C_0 is the clamped (zero strain) capacitance. ω is the angular frequency.

For a non-piezoelectric layer, the input force and velocity (F_1 and v_1) are related to the output force and velocity (F_2 and v_2) by a matrix [135]

$$\begin{aligned} \begin{pmatrix} F_2 \\ v_2 \end{pmatrix} &= \begin{pmatrix} cosk_L d_L & -iAZ_L sink_L d_L \\ -(i/AZ_L)sink_L d_L & cosk_L d_L \end{pmatrix} \begin{pmatrix} F_1 \\ v_1 \end{pmatrix} \\ &= T_L \begin{pmatrix} F_1 \\ v_1 \end{pmatrix} \end{aligned} \quad (2.2)$$

where Z_L, d_L, and k_L are the characteristic impedance, thickness, and acoustic wave number of the layer respectively. A is the area of the layer which is the same as the piezoelectric one, T_L is the transfer matrix of this non-piezoelectric layer.

As the acoustic generator in Fig. 2.1 (a) is represented by a number of cascaded two-port (non-piezoelectric layer) networks and a three-port (piezoelectric layer) one, it is possible to calculate the acoustic response of the whole stack by reducing the continuous networks to a single two-port one. The 3 by 3 matrix in equation (1) is replaced by an equivalent symmetrical one for the sake of simplicity and the notations in Wilcox's work are used here [132].

$$\begin{pmatrix} F_1 \\ F_2 \\ V_3 \end{pmatrix} = \begin{pmatrix} Z_{11} & Z_{12} & Z_{13} \\ Z_{21} & Z_{22} & Z_{23} \\ Z_{31} & Z_{32} & Z_{33} \end{pmatrix} \begin{pmatrix} v_1 \\ v_2 \\ I_3 \end{pmatrix} \tag{2.3}$$

The ratios -F_1/v_1 and -F_2/v_2 are represented by Z'_B and Z'_A respectively, and Eq.2.3 can be reduced to a 2 by 2 matrix Z_{PZ} using Z'_B

$$\begin{aligned} \begin{pmatrix} F_2 \\ V_3 \end{pmatrix} &= \begin{pmatrix} Z_{22} - \frac{Z_{12}Z_{21}}{Z'_B+Z_{11}} & Z_{23} - \frac{Z_{21}Z_{13}}{Z'_B+Z_{11}} \\ Z_{32} - \frac{Z_{12}Z_{31}}{Z'_B+Z_{11}} & Z_{33} - \frac{Z_{13}Z_{31}}{Z'_B+Z_{11}} \end{pmatrix} \begin{pmatrix} v_2 \\ I_3 \end{pmatrix} \\ &= \begin{pmatrix} Z'_{22} & Z'_{23} \\ Z'_{32} & Z'_{33} \end{pmatrix} \begin{pmatrix} v_2 \\ I_3 \end{pmatrix} \\ &= Z_{pz} \begin{pmatrix} v_2 \\ I_3 \end{pmatrix} \end{aligned} \tag{2.4}$$

Then using Z'_A, the electrical input impedance of the transducer Z_{IN}=V_3/I_3 can be found by

$$Z_{IN} = Z'_{33} - \frac{Z'^2_{23}}{Z'_A + Z'_{22}} \tag{2.5}$$

The input electrical quantities (V_3, I_3) can be related to the output quantities (F_2, v_2) by a transfer matrix T_{PZ}, which is derived by rearranging Eq.2.4.

$$\begin{aligned} \begin{pmatrix} F_2 \\ v_2 \end{pmatrix} &= \begin{pmatrix} \frac{Z'_{22}}{Z'_{32}} & Z'_{23} - \frac{Z'_{22}Z'_{33}}{Z'_{32}} \\ \frac{1}{Z'_{32}} & -\frac{Z'_{33}}{Z'_{32}} \end{pmatrix} \begin{pmatrix} V_3 \\ I_3 \end{pmatrix} \\ &= T_{pz} \begin{pmatrix} V_3 \\ I_3 \end{pmatrix} \end{aligned} \tag{2.6}$$

Also, the transfer matrices for the matching layers are represented by T_{Ln}(n=1,2...) which are similar to the T_L in Eq.2.2. n is the layer index. To calculate the transfer matrix (T) which represents the system, the transfer matrix T_{PZ} is pre-multiplied by the T_{Ln} and the system transfer matrix T is found

$$T = T_{Ln}...T_{L2}T_{L1}T_{PZ} \tag{2.7}$$

For a transducer, T relates the voltage/current (V_3 and I_3) of the input signal to the force/velocity (F_{out} and v_{out}) in the output medium through Eq.2.8.

$$\begin{pmatrix} F_{out} \\ v_{out} \end{pmatrix} = T \begin{pmatrix} V_3 \\ I_3 \end{pmatrix} \tag{2.8}$$

2.2 Validation of the 1D model

To verify the feasibility of using a multi-layered resonator to generate an acoustic standing wave field, a typical test cell that was designed based on the 1D model is used in this section for demonstration purpose.

An acoustical standing wave field is generally established along the structure (axial direction). The sound field is believed to be uniformly distributed in the radial direction (or directions normal to the axis for non-cylindrical shape structure) and this assumption is only valid when the length of the structure is larger than its width and the width is less than half of the standing wave wavelength (the use of isotropic materials is assumed). As the sound field within the multi-layered structure only varies in the axial direction, the 1D model can accurately predict the acoustic responses of such resonators.

Fig. 2.2 displays a picture of the test rig (front view). The acoustic standing wave generator consists of a round transducer, a square liquid (deionized water) layer of 5 mm thickness held in a brass block (5 mm by 5 mm by 5 mm) and a round borosilicate glass plate of 0.1 mm thickness (VWR, UK). To fit the two glass windows on the water sides for the following optical observations, the cross section of the liquid layer was chosen as a square shape (5 mm by 5 mm). The transducer was fabricated out of a lead zirconate titanate (PZT) disk (PCM 51, EP Electronic Components Ltd, UK), a backing brass bar, a front brass bar with thickness of 2 mm, 3 mm and 9 mm respectively. The diameter of the transducer is 5 mm. The other parameters of the test rig is shown in Table 2.1.

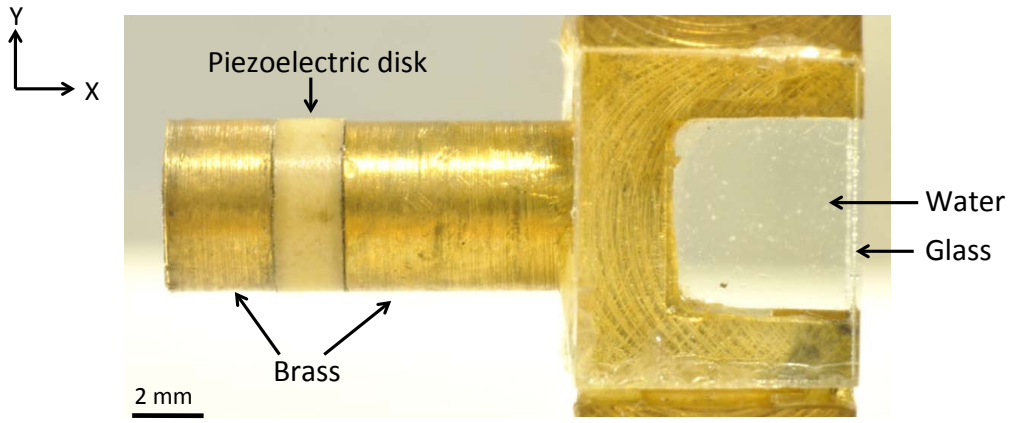

Figure 2.2: A picture of test rig for studying the bubble translation mechanism.

Table 2.1: Property of material

Layer	Density (kg/m^3)	Sound speed (m/s)	Young's modulus (GPa)	Poissons ratio	Q-factor
Brass	8400	3700	120	0.35	–
PZT	7700	3000	60	0.3	80
Water	1000	1480	–	–	30

The choices of sample dimension and operating frequency were mainly based on the frame rate of the high speed camera used in the experiment. To capture the details of bubble motion near a wall, the frame rate of the high speed camera should be chosen to be faster than the driving frequency. However, due to the storage capacity limit of the high speed camera, increasing the camera frame rate results in a decrease of viewing window size. Hence, the camera frame rate should be optimized to be faster than the driving frequency, and also be able to provide an adequately large viewing area. Based on this requirement, it was found in the experiment that a frame rate of 525 k frames/s, for example, was suitable to provide a viewing area of 1.2 mm by 0.3 mm for observing the bubble dynamics near a surface with a resolution of 128 by 48 (the bubble radii are less than 100 μm in the tests). At this frame rate, the driving frequency was chosen to be below 50 kHz (46.8 kHz used in the experiment) in order to use the camera to record at least 10 frames per driving cycle. The dimension of the test cell was then designed based on this consideration.

The choice of the thickness of the glass plate was based on the dimension of real industrial test samples. The thickness of silicon wafers that are to be cleaned in the industrial applications is less than millimetre. Also, with the present optical microscope, it is preferable to use an optical transparent medium to investigate the cleaning efficiency. For example, the contaminated area on a glass plate can be easily observed with the microscope before and after the ultrasonic cleaning. Thus, glass plates of 0.1 mm thickness were chosen as the target surface. This test cell is used in the study of single bubble translation in chapter 4.

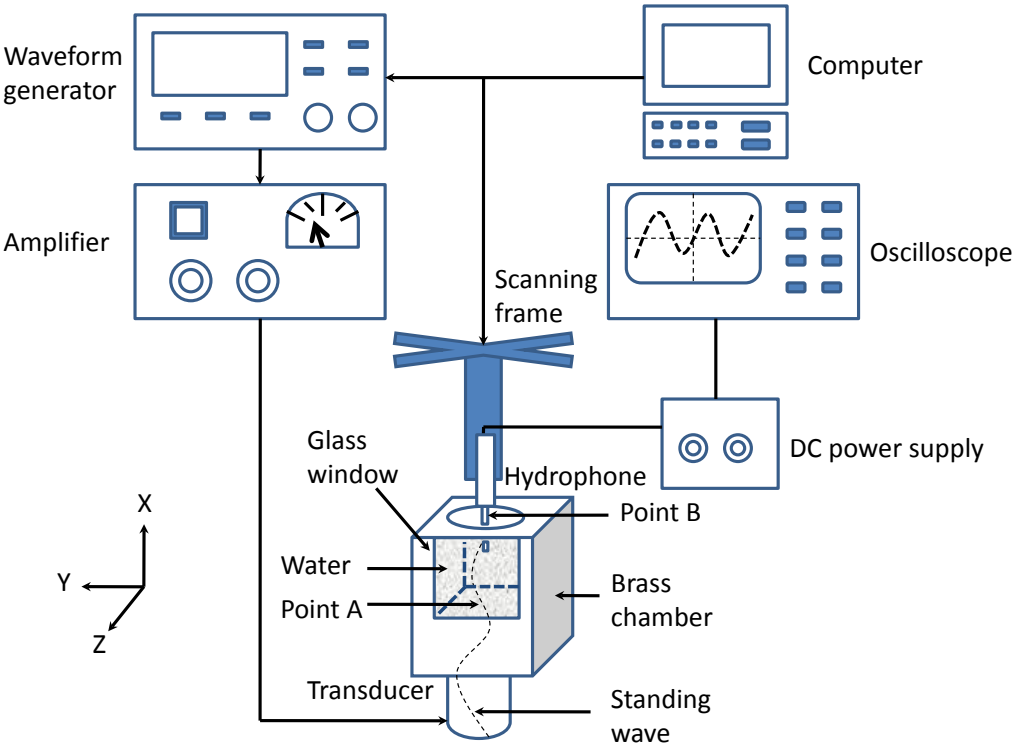

Figure 2.3: A schematic diagram of the pressure measurement for the test cell using a hydrophone.

To examine the validity of the 1D model, the pressure field in the water layer at a driving frequency of 108 kHz was measured by a calibrated needle hydrophone (HPM1/1, Precision Acoustics, UK) and compared with the result obtained from the 1D model. A diagram of the testing setup is shown in Fig. 2.3. The hydrophone is fixed on a three dimension scanning frame (3 axis motorized scanning system, Time and Precision Industries Ltd, UK) which is controlled by a computer. The hydrophone is powered by a DC power supply (DC3, Precision Acoustics, UK) and is used to measure the pressure profile in the x, y and z directions in the water

layer. The origin of the coordinate system is set at the transducer-water boundary ($x = 0$, $y = 0$, $z = 0$). The pressure amplitudes along the x axis are measured from point A (see Fig. 2.3) at the center of the base of the water column to point B (see Fig. 2.3), which is at the center of the top of the water column with a step size of 0.5 mm. The difference between the test cells shown in Fig. 2.3 and Fig. 2.2 is that the glass plate which is used as a reflector in Fig. 2.2 is removed in the hydrophone measurement case. It needs to be pointed out that the purpose of the hydrophone measurement is to solely examine the 1D model predictions so that confidence in its validity can be obtained. As the 1D model treats each matching layer in the same way, it is reasonable to accept that the pressure profile of a testing cell with the thin glass plate (sound soft boundary) can be accurately predicted by the 1D model which is verified in the case without the additional glass plate.

As bubbles only move in the water layer, the focus of the validation is mainly on the pressure profile in the water column. Fig. 2.4 shows the comparison between the calculated impedance of the test cell without the glass plate and that of the cell with the glass layer. It can be seen from Fig. 2.4 that the addition of the glass plate shifts the resonance frequencies of the structure down to lower frequencies.

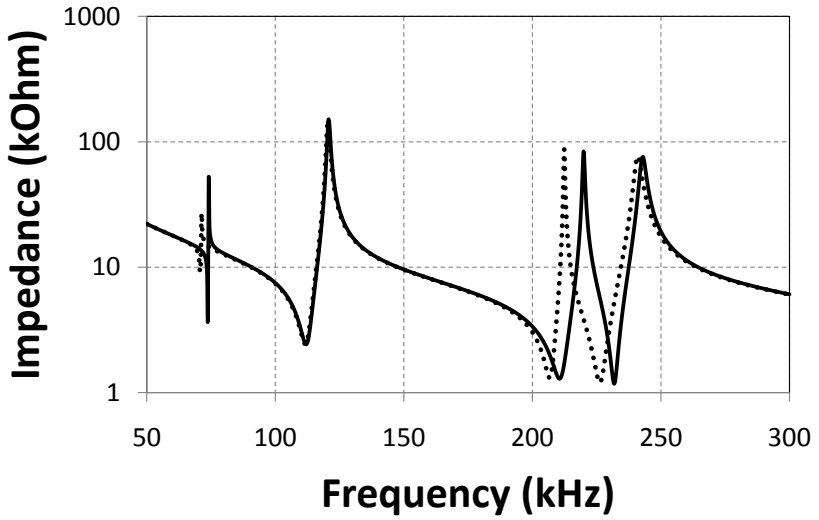

Figure 2.4: Calculated impedance of test cell without (solid line) and with (dotted line) the glass plate. The frequencies used in the calculation are from 50 kHz to 300 kHz.

A measured pressure distribution in the water along the x axis (as shown in Fig. 2.2) and a simulated one at 108 kHz are shown in Fig. 2.5. The input signal amplitude

was chosen as 1.8 V (peak). A pressure amplitude maximum (11.4 kPa) and an amplitude minimum (3 kPa) are located at x = 1.7 mm and x = 5 mm respectively as indicated in the figure. The simulated pressure distribution was normalized with respect to the measured pressure amplitude in the test. As seen in Fig. 2.5, there is a discrepancy between the theoretical prediction and the test. Two possibilities were recognized that could influence the accuracy of the pressure measurements. The first one results from the movement of the hydrophone. The volume in the water layer occupied by the hydrophone changes each time during the pressure measurement. That means the thickness of the water layer changes with the hydrophone movement (the cross section of the water layer is kept the same). This variation of water thickness shifts the impedance of the test rig. Therefore, the measured pressure amplitude at each point could be different from that in the absence of the hydrophone. The second factor may come from the 1D assumption used in the model. The 1D theory has been verified as a suitable model for providing a quantitative prediction of the multi-layered resonator [133]. However, the behaviour of a real 3D test cell could be different from the simple 1D assumption. For example, in order to create a 1D sound field in the lateral direction within low frequency range, the length of the structure was designed to be larger than its width and the width was less than half of the standing wave wavelength (the use of isotropic materials is assumed). On the other hand, at high frequency, the width could be larger than half of wavelength, so standing waves can be established in the radial direction. However, the resonance frequency of standing wave in the radial direction cannot be simulated by the 1D model. This could contribute to the discrepancy between the theory and test in Fig. 2.5.

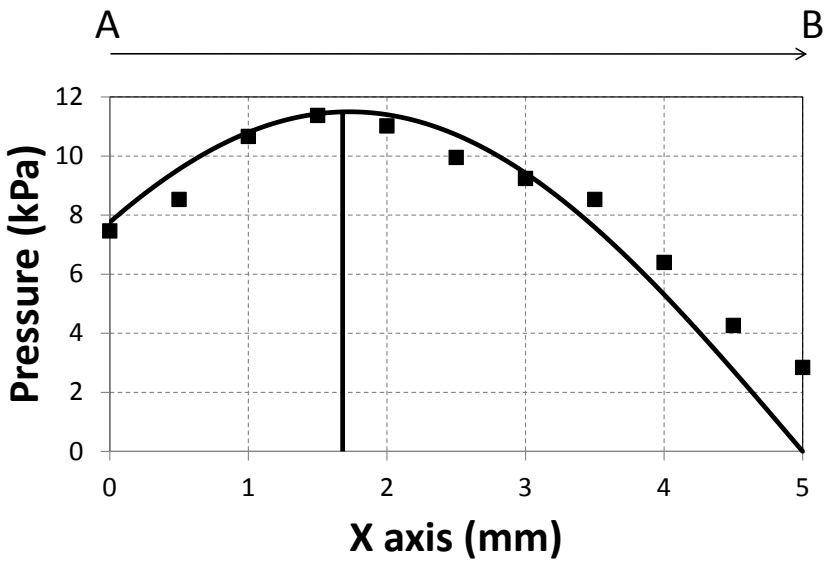

Figure 2.5: Measured (square blocks) and simulated (solid line) pressure profiles in the water layer at 108 kHz. The pressure distribution is measured from the center of the base of the water column (A) to the center of the top of the water column (B) as shown in Fig. 2.3. The input signal amplitude is 1.8 V. The solid vertical line on the left side indicates the position (x = 1.7 mm) where the y and z directions measurement shown in Fig. 2.6 was carried out.

Only a small difference between the 1D model prediction and the measured result is seen in Fig. 2.5. Uniform pressure distributions along the y axis and z axis are assumed here. This assumption is validated by the measurement of pressure field in the y and z directions in the water layer (Fig. 2.6). The pressure profiles were measured in the y axis and z axis directions at x = 1.7 mm. It can be seen from Fig. 2.6 that slight variations existed in the y and z directions. These variations, however, were small (within ±10%) so that the one-dimension assumption used in the 1D model is considered still to be valid.

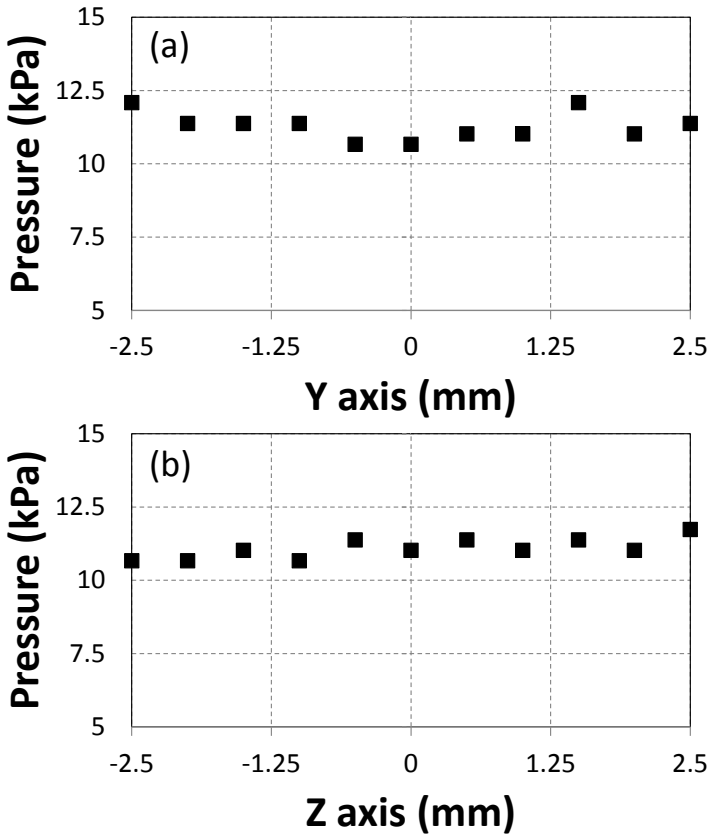

Figure 2.6: Pressure profiles measured by the hydrophone in the y axis and z axis at 108 kHz for input signal of 1.8 V and x = 1.7 mm. (a) measured pressure profile in the y axis; (b) measured pressure profile in the z axis.

2.3 Summary

In this chapter, the design of an acoustic standing wave field using a multi-layered stack was discussed. The acoustic standing wave field within a multi-layered stack is designed based on a one-dimensional transducer matrix model. The 1D model treats each layer as an individual matrix which includes the information of the layer thickness, density, impedance and wave number. The input voltage/current are related to the output force/velocity through a total transfer matrix, which is obtained by multiplying the transfer matrix of each layer. The 1D model can accurately predict the impedance of the test cell as well as the pressure distribution within the whole assembly.

Chapter 3

Theory of bubble translation

Prior to cleaning a contaminated surface, micro-bubbles are first needed to be transported to a target region in a controlled manner. This chapter presents a review of the background theory of single and multi bubble translations in an acoustic standing wave field .

3.1 Bubble translation

The dynamics of a system or an object can be represented by its kinetic (T) and potential (U) energy. The kinetic and potential energy are linked through the Lagrangian, L [100]:

$$L = T - U \tag{3.1}$$

The motion of an object can be obtained by substituting its Lagrangian into the classic Euler-Lagrange equation [136]:

$$\frac{d}{dt}\frac{\partial L}{\partial \dot{q}_i} - \frac{\partial L}{\partial q_i} = 0 \tag{3.2}$$

where q_i is the generalized coordinate, i is the ith degree of freedom.

Eq.3.2 is the basis of the following bubble motion analysis. For a bubble, the study of its dynamic features is now converted to explore its kinetic and potential energy components in a liquid system. The kinetic energy is normally written as [100]:

$$T = \frac{\rho}{2} \int |\nabla\varphi|^2 dV \tag{3.3}$$

where ρ is the liquid density, φ is the velocity potential, V is bubble volume.

Let us start from a simple one dimensional case where a bubble undergoes radial pulsation and translation in an incompressible liquid in the x direction. The velocity potential (φ) at the bubble surface in a polar coordinate system (r, θ) is given by [136]:

$$\frac{\partial\varphi}{\partial r} = \dot{R} + \dot{x}cos\theta \tag{3.4}$$

where R is the bubble time-varying radius. The overdot denotes the time derivative. Eq.3.4 is valid for both the traveling wave and standing wave cases. Since the bubble motion is controlled by a standing wave in this thesis, the sound field is assumed to be established in the x direction here.

Because the velocity potential (φ) satisfies the Laplace equation [136]

$$\Delta\varphi = 0 \tag{3.5}$$

By assuming the liquid is incompressible, a solution of the velocity potential as:

$$\varphi = -\frac{\dot{R}R^2}{r} - \frac{\dot{x}R^3cos\theta}{2r^2} \tag{3.6}$$

On the other hand, the potential energy of a bubble in a sound field is [100]

$$U = -p_{sc}V - xF_{ex} \tag{3.7}$$

where p_{sc} is the scattered pressure at the bubble surface. F_{ex} are total external forces in the x direction. By taking incident wave, surface tension and viscosity into account, the scattered pressure p_{sc} is given by [137]:

$$p_{sc} = (P_0 + \frac{2\sigma}{R_0})(\frac{R_0}{R})^{3\gamma} - \frac{2\sigma}{R} - \frac{4\eta\dot{R}}{R} - P_0 - P_{sw} \tag{3.8}$$

where P_0 is the hydrostatic pressure, R_0 is the bubble equilibrium radius. c is the sound velocity in a liquid. σ is the bubble surface tension, γ is the polytropic exponent of the gas within the bubble, and η is the liquid viscosity. Since the bubble volume V and spatial position x are time-varying parameters, Eq 3.7 and 3.8 take the non-equilibrium form here. P_{sw} is the external driving signal which is defined as a standing wave:

$$P_{sw} = P_a sin(\omega t) sin(kd) \tag{3.9}$$

where P_a is the pressure amplitude, ω is the angular frequency, and k is the wave number. As only a one dimensional standing wave is considered here, d is the separation distance between the bubble center and a pressure node in the x direction.

Substituting Eq.3.3 - 3.9 into Eq.3.1, and then applying the result to Eq.3.2, a pair of coupled x direction translation and oscillation equations are obtained [60]:

$$R\ddot{R} + \frac{3}{2}\dot{R}^2 - \frac{p_{sc}}{\rho} = \frac{\dot{x}^2}{4} \tag{3.10}$$

$$\ddot{x} + \frac{3\dot{R}\dot{x}}{R} = \frac{3F_{ex}}{2\pi\rho R^3} \tag{3.11}$$

The translation and oscillation of a bubble are not independent of each other, rather, they are closely linked through a coupled term $\dot{x}^2/4$ on the right hand side of Eq.3.10.

Similarly, in a two dimensional system (x - y), the translation in the y direction is:

$$\ddot{y} + \frac{3\dot{R}\dot{y}}{R} = \frac{3F_{ey}}{2\pi\rho R^3} \tag{3.12}$$

where F_{ey} are the external forces in the y direction.

It needs to be pointed out that Eq 3.10 is the Rayleigh-Plesset (RP) equation that represents the bubble radial pulsation at small pressure amplitude. The RP equation given in Eq 3.10 includes the effect of surface tension, viscous damping, and an incident wave. However, it neglects the acoustic radiation from the bubble. It was found in Lauterborns simulation work [138] that the RP equation yields unreasonable large amplitude solutions without the acoustic radiation term [68]. Also, at large amplitude, the assumption used in the derivation of the RP equation that the velocity of radial oscillation is smaller compared to the sound speed in liquid is no longer valid [60]. Both these reasons render the RP equation unsuitable for simulating large bubble oscillation. In contrast, Keller and Miksis proposed an equation that takes the acoustic radiation from the bubble into account. This Keller-Miksis equation has been verified to be able to model large bubble oscillation [76]. Therefore, the Rayleigh-Plesset equation is replaced by the Keller-Miksis equation and a new oscillation equation is found [139]:

$$(1 - \frac{\dot{R}}{c})R\ddot{R} + (\frac{3}{2} - \frac{\dot{R}}{2c})\dot{R}^2 - \frac{1}{\rho}(1 + \frac{\dot{R}}{c})p_{sc} - \frac{R}{\rho c}\dot{p}_{sc} - \frac{\dot{x}^2}{4} = 0 \tag{3.13}$$

Eq 3.11, 3.12,and 3.13 are the fundamentals of the bubble motion analysis. With a given sound field, the only unknown parameters are the external forces in the x and y directions. The next step is then to investigate the influence of these external forces on the bubble translations.

3.2 Single bubble translation in a bulk medium

The bubble translation analysis starts from a simple bulk medium case. When a bubble moves within an acoustic standing wave field in a bulk medium, the dominating forces exerted on it are the primary Bjerknes force ($F_{Primary}$), the buoyancy force (F_{buoy}), and the viscous drag forces (F_{vx}, F_{vy}) as shown in Fig. 3.1.

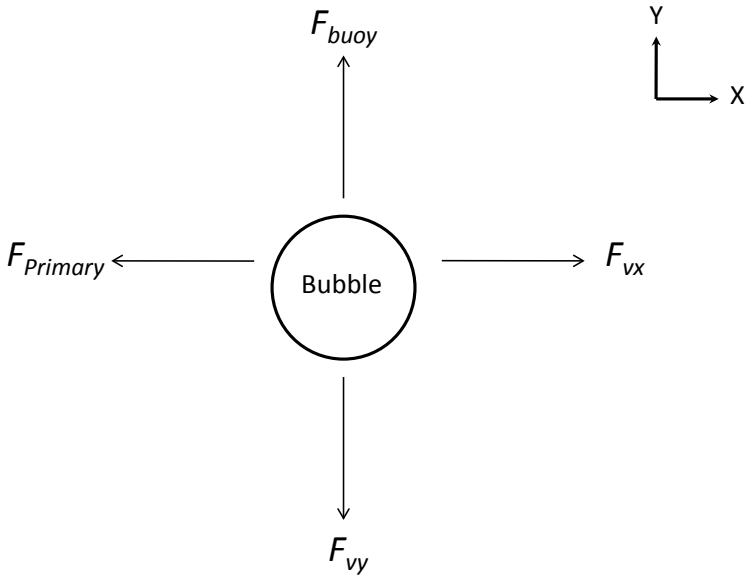

Figure 3.1: A diagram of forces exerted on a bubble in a bulk medium

The primary Bjerknes force is the derivation of Bjerknes force in an acoustic standing wave field. A well-known form of the Bjerknes force ($F_{Bjerknes}$) is [137]:

$$F_{Bjerknes} =< -V \nabla P > \tag{3.14}$$

where ∇P is the pressure gradient, <> denotes the time average. Suppose that an acoustic standing wave field (P_{sw} in Eq.3.9) is established in the x axis and is uniformly distributed in the y axis, the primary Bjerknes force ($F_{primary}$) then takes the form of [60]:

$$F_{primary} = - < \frac{4\pi}{3} R^3 k P_a sin(\omega t) cos(kd) > \tag{3.15}$$

It is worth mentioning that Eq 3.15 results in a non-zero primary Bjerknes force because the parameter R is a time-varying term. Over a cycle, for example, the time average of $Rsin(\omega t)$ is non-zero [137].

From a physical point of view, the primary Bjerknes force arises from the pressure difference across a bubble surface and its influence on the bubble translation depends on the pressure amplitude. In a weak sound field, the net primary Bjerknes force

is linked to the bubble volume variation over one driving cycle (Eq.3.14). Fig. 3.2 shows the responses of a bubble driven below resonance frequency (a1 - a4), and a bubble driven above resonance frequency (b1 - b4) to the acoustic field at four different time $t = 0, \frac{T}{8}, \frac{3T}{8}$, and $\frac{T}{2}$ (T is the duration of one driving cycle). Considering a bubble smaller than its resonance size and the driving signal wavelength, the minimum bubble volume is achieved at a maximum pressure amplitude (Fig. 3.2 a1). Accordingly, the bubble is pushed towards the point A (pressure node) owing to the pressure difference across the bubble surface. It can be seen from Fig. 3.2 a2 - a4 that a decrease of pressure amplitude leads to a growth of bubble volume. The bubble volume, for example, reaches its maximum at a minimum pressure amplitude in Fig. 3.2 a4. In this case, the overall pressure difference on the bubble surface forces the bubble to move towards the point B (pressure anti-node) instead. Also, since V is larger in Fig. 3.2 a4 than in a1, the Bjerknes force ($V\nabla P$) in Fig. 3.2 a4 then outweighs its counterpart in Fig. 3.2 a1. Therefore, the average $V\nabla P$, over an acoustic cycle, directs the bubble to move towards the pressure anti-node. Similarly, a bubble larger than its resonance size would move towards the pressure node because of the different response of the bubble volume to the sound field (Fig. 3.2 b1 - b4).

At a large pressure amplitude, the primary Bjerknes force behaves in a different manner (see Fig.3.3). The radial pulsation becomes nonlinear in an intense sound field which would result in a bubble collapse [54]. During the break-up, the bubble surface experiences a longer expansion time than in a weak sound field. That means there is more time for the primary Bjerknes force to grow. As seen in Fig.3.3, this growth momentum of primary Bjerknes force on a bubble driven below resonance is maintained even when the sound field starts the compression phase. Compared to the low pressure case, the average $V\nabla P$ would eventually change its sign when the expansion time is long enough. Thus, the primary Bjerknes force creates new equilibrium positions between pressure nodes and anti-nodes where bubbles may rest. Since only low pressure amplitudes are used in this thesis, the larger pressure amplitude case is not considered in the following chapters.

The buoyancy force in the y axis (Fig. 3.1) is [137]

$$F_{buoy} = \frac{4\pi}{3} R^3 (\rho - \rho_{gas}) \tag{3.16}$$

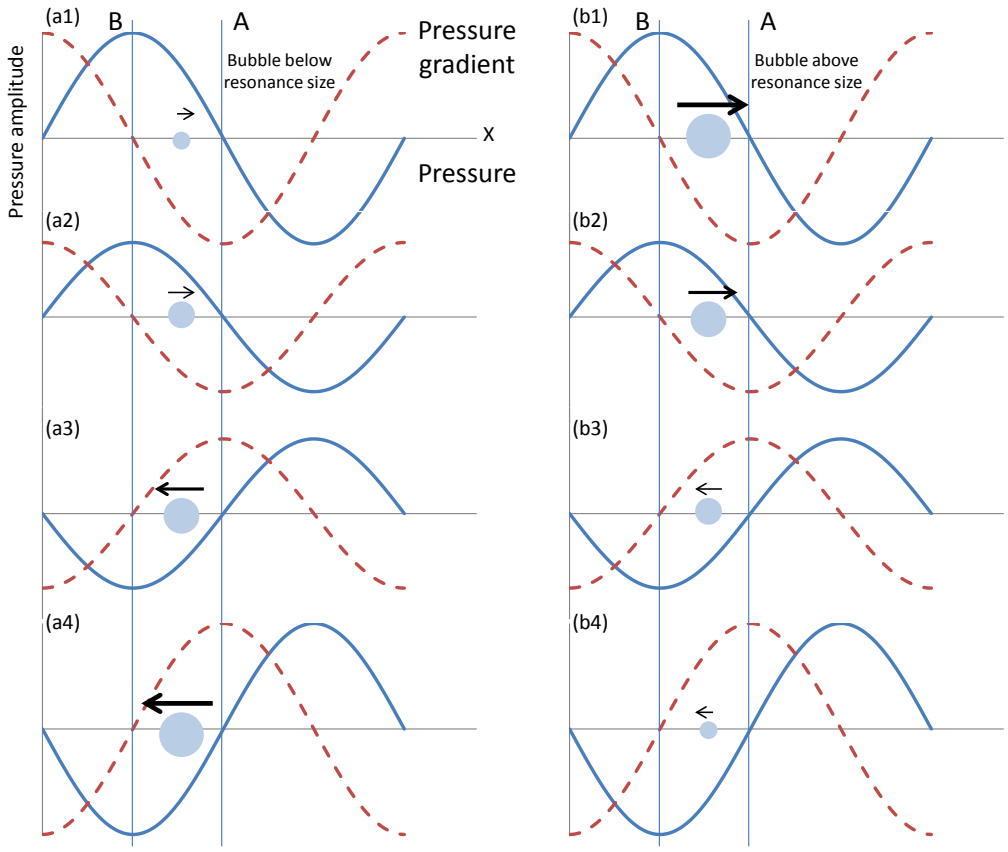

Figure 3.2: Primary Bjerknes force acting on a bubble in a weak sound field at four different time $t = 0, \frac{T}{8}, \frac{3T}{8}$, and $\frac{T}{2}$. (a1 - a4) Bubble driven above its resonance frequency. The bubble volume grows as the pressure amplitude falls. The $V\nabla P$ in a1 is less than its counterpart when the bubble reaches its maximum size (a4). Thus, the average force exerted on the bubble leads the bubble to move towards the pressure anti-node (point B). (b1 - b4) Similarly, bubble driven below its resonance frequency is pushed towards the pressure node instead (point A). The solid lines represent the pressure profiles, and the dashed lines are pressure gradient.

where ρ_{gas} is the density of gas inside the bubble.

The bubble also experiences viscous drag forces in a liquid medium. The drag forces in the x (F_{vx}) and y (F_{vy}) axes are given by [60]:

$$F_{vx} = -12\pi\eta R(\dot{x} - v_e) \tag{3.17}$$

$$F_{vy} = -12\pi\eta R\dot{y} \tag{3.18}$$

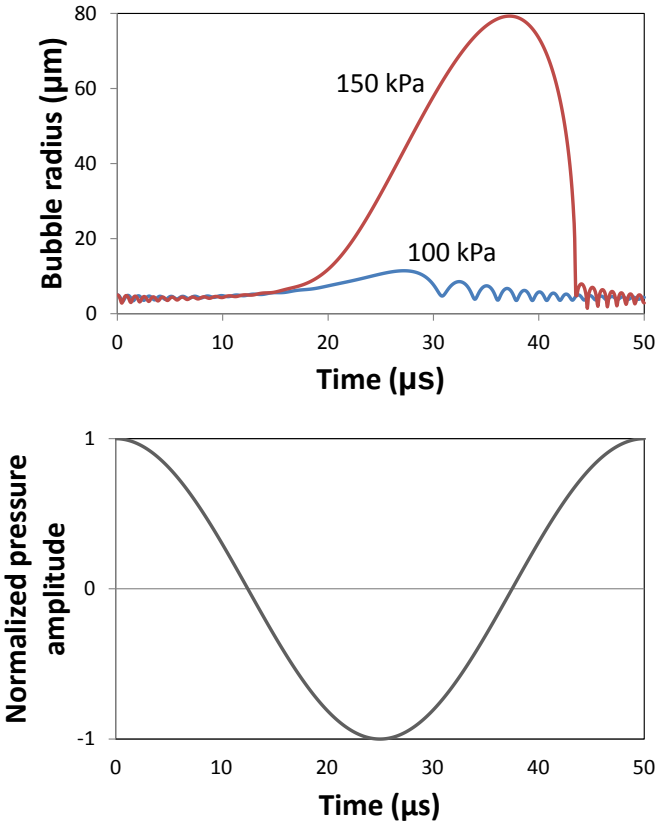

Figure 3.3: The response of a bubble to a strong acoustic field. The primary Bjerknes force can change the sign when the bubble undergoes non-linear oscillation. The simulation is based on the Keller-Miksis equation (Eq.3.13) for a bubble of 5 μm radius driven at 20 kHz. The pressure amplitudes are 100 (blue line) and 150 kPa (red line) respectively.

where v_e is the liquid velocity that is generated by the imposed acoustic field at the center of the bubble

$$v_e = \frac{P_a}{\rho c} cos(\omega t) cos(kd) \tag{3.19}$$

Eq 3.17 and 3.18 are the viscous drag forces on a non-oscillating bubble at large Reynolds number. At moderate Reynolds number, a non-oscillating bubble is supposed to experience a weaker drag force. Mei et al [140] proposed an empirical drag coefficient for a non-oscillating bubble at finite Reynolds number. However, it was found in the experiment presented in Chapter 4 that Mei's drag coefficient underestimates the drag force on the target bubble because it neglects the bubble's radial pulsation. It has been recognized that a bubble cannot only translate in an

acoustic standing wave field, but also oscillate during its translation. Magnaudet and Legendre [141] theoretically studied the drag force on a pulsating bubble, and found out that the radial pulsation increases the viscous drag force on a bubble. At moderate Reynolds number, the maximum drag coefficient for an oscillating bubble is 12 which is the same as for a non-oscillating bubble at high Reynolds number. Therefore, Eq 3.17 and 3.18 provide a qualitatively good approximation of the drag force here.

3.3 Multi-bubble translation in a bulk medium

In a multi-bubble environment, in addition to the primary Bjerknes force, buoyancy force, and viscous drag forces, a bubble experiences secondary Bjerknes forces generated by nearby bubbles.

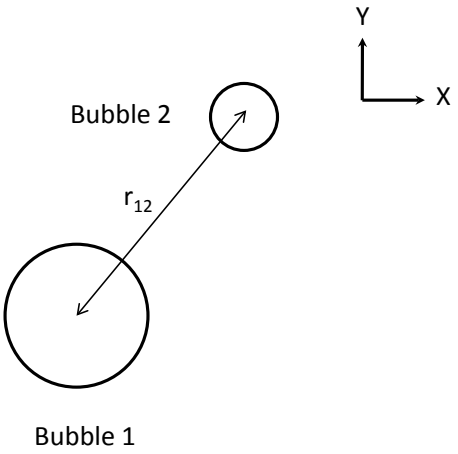

Figure 3.4: A diagram of a bubble and a neighboring bubble.

It is well-known that a neighboring bubble emits a sound field that creates a pressure gradient on the original bubble. From the definition of Bjerknes force in Eq. 3.14, the target bubble experiences a Bjerknes force due to this pressure difference, known as secondary Bjerknes force. For a pair of bubbles, if the bubble shapes are assumed to remain spherical for all time with the radii R_1 and R_2 respectively, the respective pressure, for example, generated from bubble 2 on bubble 1, is given by [64]:

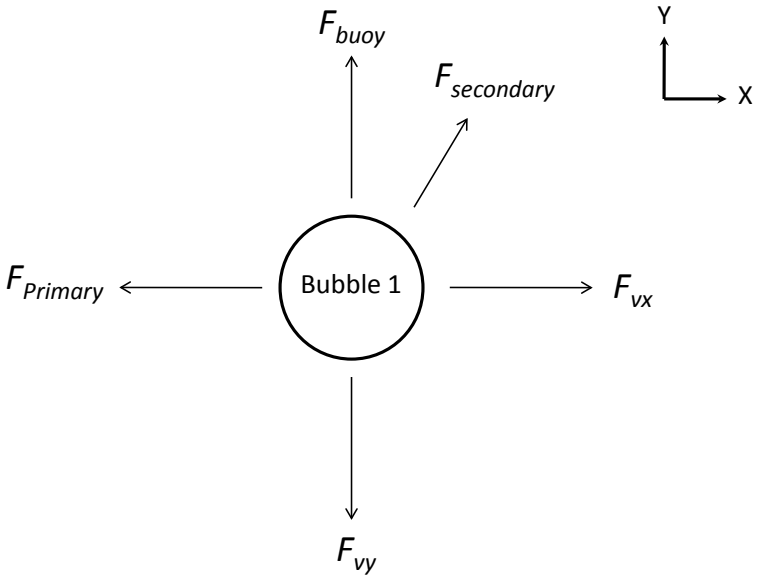

Figure 3.5: The relationship between different external forces on bubble 1 (Fig. 3.4).

$$p_{12} = \frac{\rho}{r_{12}} \frac{d R_2^2 \dot{R}_2}{dt} \tag{3.20}$$

where r_{12} is the separation distance between the two bubbles (Fig. 3.4).

The secondary Bjerknes force exerted on bubble 1 (Fig. 3.5) is [64]:

$$\begin{aligned} F_{secondary} &= - < V_1 \nabla p_{12} > \\ &= < V_1 \frac{\rho}{r_{12}^2} \frac{d}{dt} (R_2^2 \dot{R}_2) > \\ &= \frac{\rho}{4\pi r_{12}^2} < V_1 \frac{d^2 V_2}{dt^2} > \end{aligned} \tag{3.21}$$

where V_1 and V_2 are the volume of bubble 1 and 2 respectively.

Integrating the above equation over one driving cycle and using partial integration, the secondary Bjerknes force is given by:

$$F_{secondary} = -\frac{\rho}{4\pi r_{12}^2} < \dot{V}_1 \dot{V}_2 > \tag{3.22}$$

3.4 Multi-bubble translation near a surface

In a more complicated system, a bubble's motion is also influenced by a nearby wall in addition to neighboring bubbles. To model this, the boundary can be replaced by an imaginary bubble on the other side of the wall (see Fig. 3.6). The imaginary bubble oscillates in phase with the original one at the same amplitude [142]. Similar to the previous multi-bubble case, the imaginary bubble exerts a secondary Bjerknes force on the target bubble and its influence can also be expressed with Eq.3.21. The forces relationship of a bubble (bubble 1) near a surface is demonstrated in Fig. 3.7.

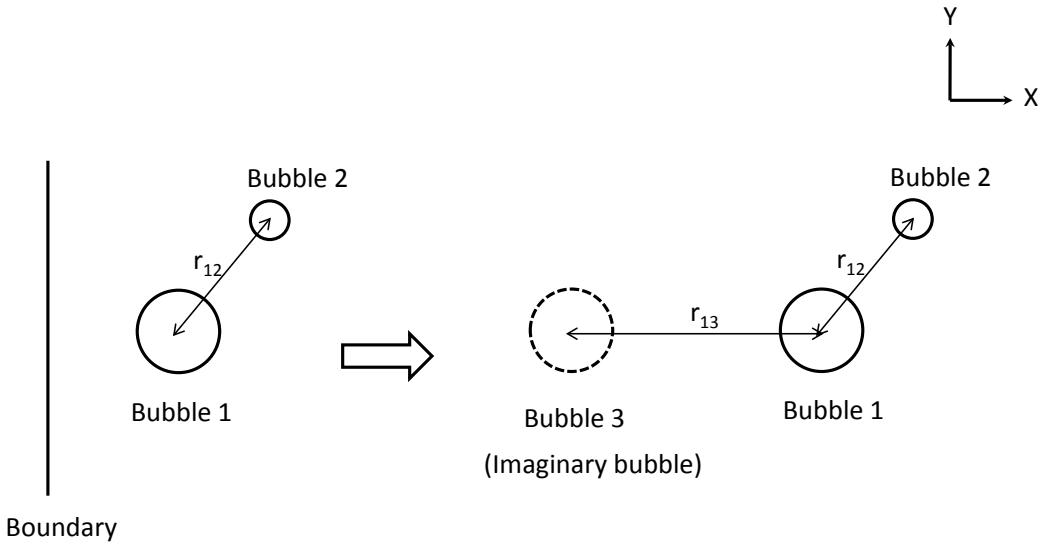

Figure 3.6: A diagram of a bubble, its imaginary counterpart, and a neighboring bubble.

Due to the boundary layer condition near the wall surface, the flow velocity gradually drops to zero on a solid surface. When a bubble approaches a wall, it experiences the asymmetric flow field which generates a lift force on the bubble surface [143]. The lift force on a non-oscillating bubble moving next to a wall has been studied experimentally and theoretically [144–146]. It has been recognized that the wall induced lift force takes effect within a short range from the wall surface because it varies as a function of (d_{wall}/R), where d_{wall} is the separation distance between the bubble center and the surface. The lift force is negligible when $d_{wall}/R > 10$ (assuming Reynolds number $Re < 100$)

At moderate Reynolds number ($Re < 100$), the lift force is given by [145]:

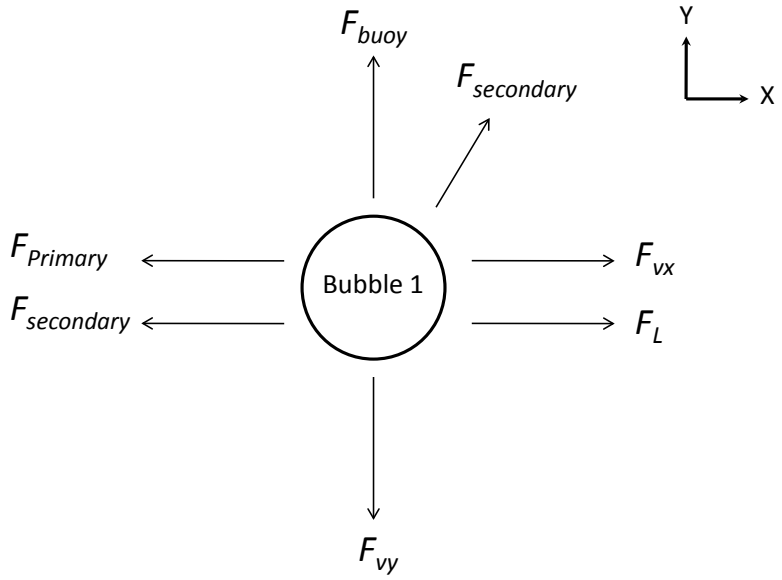

Figure 3.7: The relationship between different external forces on bubble 1 (Fig. 3.6) near a surface.

$$
\begin{aligned}
F_L &= \frac{C_L \pi R^2 \rho \dot{y}^2}{2} \\
C_L &= b^2 C_{L0} (r_{13}/3R)^{-2tanh(0.01Re)} + (1 - exp(-0.22Re^0.45)) C_{L\inf} \\
b &= 1 + 2 * tanh(0.17Re^0.4 - 0.12Re^0.05) \\
C_{L0} &= 8.94 * (2/3)^2 (r_{13}/2\dot{y}\rho/\mu)^{-2.09} \\
C_{L\inf} &= -\frac{3}{8}(\frac{2R}{r_{13}})^4 1 + \frac{1}{8}(\frac{2R}{r_{13}})^3 + \frac{1}{6}(\frac{2R}{r_{13}})^5 + O(\frac{2R}{r_{13}})^1 0
\end{aligned}
\tag{3.23}
$$

where $Re = 2\dot{y}R\rho/\nu$.

Furthermore, in a multi-bubble environment, the bubble radial equation (Eq.3.13) needs to be expanded to include the influences from the nearby boundaries and neighboring bubbles. By incorporating Eq.3.21 into the scattered pressure (P_{sc}) in Eq.3.13 and neglecting coupling terms of higher orders, the oscillation of the ith bubble is obtained:

$$(1-\frac{\dot{R}_i}{c})R_i\ddot{R}_i+(\frac{3}{2}-\frac{\dot{R}_i}{2c})\dot{R}_i^2-\frac{1}{\rho}(1+\frac{\dot{R}_i}{c})P_{sc}-\frac{R_i}{\rho c}\dot{P}_{sc}= \frac{\dot{x}_i^2}{4}-\sum_{\substack{j=1\\j\neq i}}^{I}\frac{1}{r_{ij}}(2\dot{R}_j^2R_j+R_j^2\ddot{R}_j) \tag{3.24}$$

$$p_{sc}=(P_0+\frac{2\sigma}{R_{i0}})(\frac{R_{i0}}{R_i})^{3\gamma}-\frac{2\sigma}{R_i}-\frac{4\eta\dot{R}_i}{R_i}-P_0-P_{ex} \tag{3.25}$$

where R_{i0} is the equilibrium radius of the ith bubble and an ensemble of I bubbles is considered. r_{ij} is the distance between the center of the ith and jth bubbles.

The left terms of Eq.3.24 are the modified Keller-Miksis equation [68] for the ith bubble. This modified Keller-Miksis equation is coupled to the velocity of the ith bubble through the first term on the right, and to the pressure emitted or scattered by the neighboring bubbles through the second term on the right.

3.5 Summary

In this chapter, the theory of bubble translation in a liquid medium was revisited. Based on the Lagrangian formulism, a pair of bubble translation and radial oscillation equations are obtained. The bubble translation in a sound field is the outcome of the competition between different forces exerted on it. In a bulk medium, a bubble experiences the primary Bjerknes force, the buoyancy force, and the viscous drag forces. Additionally, the translation of a bubble is also linked to its oscillation through a coupled term which represents the time varying velocity. In a multi-bubble environment, besides the mentioned forces, the nearby boundaries and neighboring bubbles also exert secondary Bjerknes forces on the target bubble.

Chapter 4

Single bubble translation

The transportation of micro-bubbles to a contaminated substrate is important in ultrasonic cleaning. Most of the previous studies focused on the interaction between a surface and cavitation bubbles. Little attention has been given to understand the translation of moderately oscillating bubbles near a boundary. The influence of factors, such as external pressure amplitude, bubble size, and driving frequency etc, on the translation of micro-bubbles in a weak acoustic standing wave field is still unclear. In this chapter, the mechanism of single bubble translation in a weak acoustic standing wave field is explained based on the force balance model, and is examined experimentally with a high speed camera system. A good agreement is found between the observed bubble movement trajectories near a surface and the theoretical predictions.

4.1 Experimental configuration

To investigate the single bubble translation, three tools: a bubble generator, an acoustic standing wave generator, and an optical observation system were used in the experiment. A bubble generator which is based on the principle of electrolysis was used. A standing wave field was generated by a multi-layered structure and the characteristics of this field were simulated by the 1D model. Details of bubble translational and oscillatory motion were recorded by the optical observation system.

Using these three tools, the bubble trajectories within the test cell were determined. The bubble generator and acoustic standing wave generator were constructed at the Non-destructive testing group, Imperial College London. The optical observation system was kindly provided by the Christian Doppler Laboratory for Cavitation and Micro-Erosion at the Georg-August-Universität Göttingen, Germany. The same physical arrangement is also applied in chapter 5 - 6.

4.1.1 Bubble generator

Bubbles used in this study are generated by an electrolysis method. Two wires (tin-coated copper) are connected to a DC power supply (TNG 35, Voltcraft, Germany) and the electrical potential is set to 5 V. The free ends of the wires are placed at x = 3 mm (the origin of the coordinate system is set at the center of the transducer-water boundary as shown in Fig. 4.1). Hydrogen gas bubbles are generated at the tip of the negative electric wire and escape from there afterwards. The bubble diameter varies from 10 μm when there is no ultrasound, up to 200 μm when the ultrasound device is switched on. The large bubbles are the outcomes of bubble coalescence processes which are significantly enhanced in the presence of ultrasound.

4.1.2 Acoustic standing wave generator

The detail of the acoustic standing wave generator is given in chapter 2 section 2.2. To clearly illustrate the bubble transport mechanism, it is favorable to design a simple standing wave field with one pressure node and one pressure anti-node along the axial direction in a liquid medium (matching layer) and with little variations in the radial direction. Within this acoustic field, the bubble migrating direction can be easily categorized either towards the pressure node or pressure anti-node based on bubble size and acoustic pressure amplitude. The bubble generator produces bubbles of about 100 μm (radius) indicating resonance frequencies of about 30 kHz. Therefore, in order to ensure operation above the resonance frequencies of the bubbles, a driving frequency of 108 kHz was designed.

A schematic diagram of the setup is shown in Fig. 4.1. A continuous sinusoidal

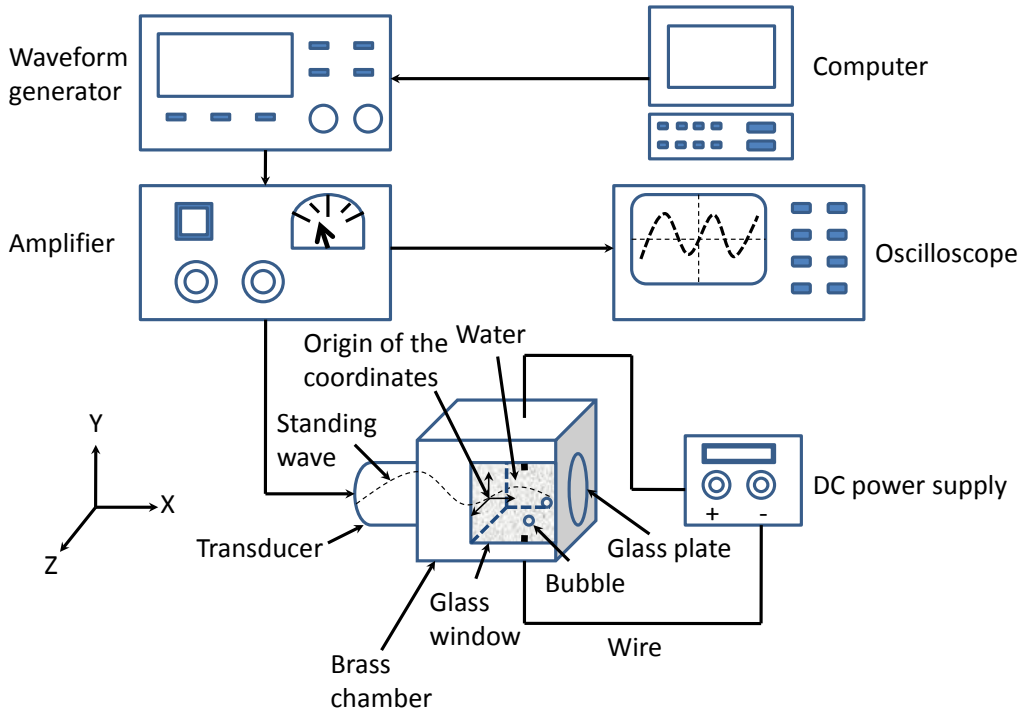

Figure 4.1: A schematic diagram of the acoustic standing wave generator.

wave is transmitted from a waveform generator (AFG 3021, Tektronix, USA) to a transducer via an amplifier (HSA 4101, NF corporation, Japan). The input signal is monitored by an oscilloscope (TDS 220, Tektronix, USA). A standing wave is established in the stack along the x axis and has negligible variations in the y and z directions (see chapter 2 section 2.2 for more details). The origin of the coordinates is set at the center of the transducer-water boundary (x = 0, y = 0, z = 0). A water layer constrained within a brass chamber is placed between the transducer and a glass plate (from x = 0 to 5 mm). To allow light to pass through the water layer for optical observations, two glass windows are fit on the sides of the brass chamber. Bubbles escape from the wire connected to the negative port of the DC power supply and migrate in the water medium. The wires connected to the DC power supply are positioned at x = 3 mm.

4.1.3 Optical observation system

A high speed camera (FastCam SA5, Photron, USA) was used to investigate the bubble trajectory and oscillatory motion. The maximum frame rate of the camera

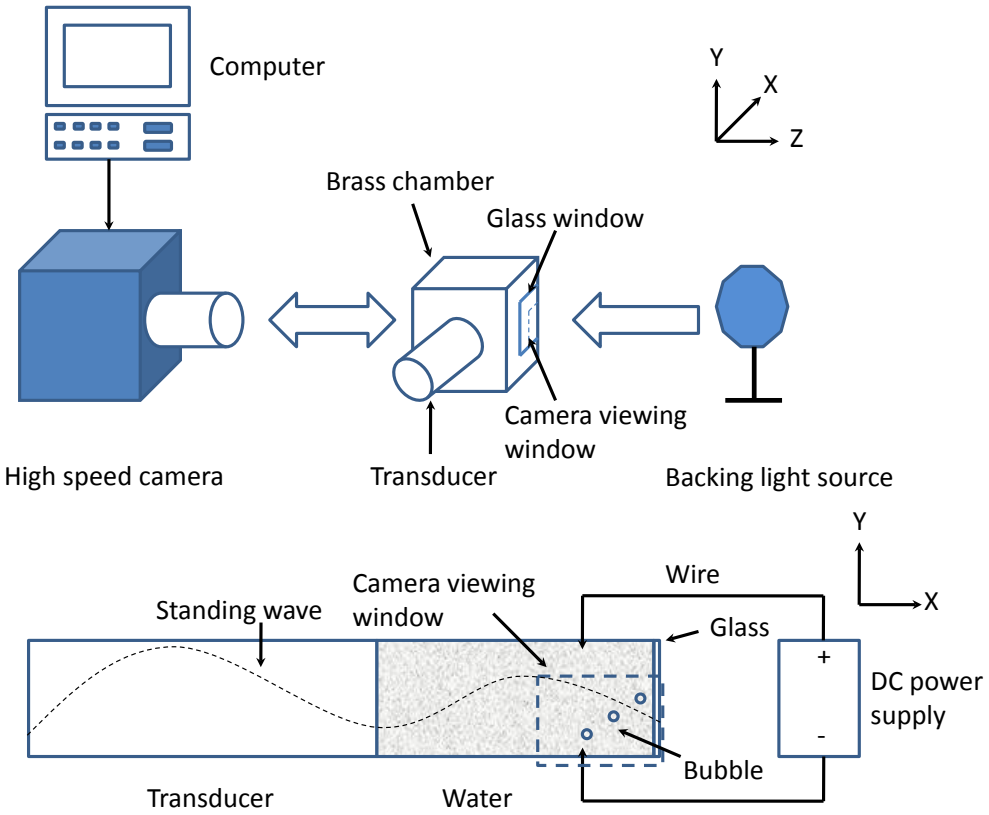

Figure 4.2: A schematic diagram of the optical observation system.

is 1 Mega frames/s and is therefore suitable for analyzing bubble motion in pressure fields oscillating at hundreds of kilo-Hertz. Fig. 4.2 shows the schematic diagram of the measurement setup. A backing light source is positioned opposite to the high speed camera with the standing wave generator in the middle. A viewing window of 3.9 mm by 3.8 mm is chosen to cover the glass plate and the bubble injection point at the same time. Recorded videos are transmitted back to a computer and are analyzed by an object tracking program written in Matlab (Mathworks Inc, USA). In the Matlab program, the center of a bubble is tracked in each frame and a plot of the bubble center positions with respect to time is obtained. The dimensions of objects in a video are calibrated with a standard 300 μm width stick.

4.2 Results

In this section, the experimental results of single bubble translation in an acoustic standing wave field are presented. The values of the physical parameters used in

this study are f = 108 kHz, ρ = 1000 kg/m^3, P_0 = 101.3 kPa, c = 1480 m/s, σ = 0.072 N/m, γ = 1, η = 0.001 Pa*s. Since the investigation of bubble trajectory only requires the recording of bubble motion as a whole rather than observing the oscillation of every driving cycle, a frame rate of 10000 frames/s was used and was verified to be suitable for this case.

4.2.1 Acoustic standing wave field

The 1D model was used to predict the pressure distribution in the x axis direction of a multi-layered structure with an additional glass plate at the end. A typical result calculated from Eq.2.1-2.8 at 108 kHz is shown in Fig. 4.3. The input signal amplitude is 2 V (peak). A minimum pressure amplitude (1.2 kPa) and a maximum pressure amplitude (11.4 kPa) in the water layer are seen at the x = 5 mm and x = 2 mm respectively. Based on the previous discussion, bubbles are anticipated to migrate from the initial injection point (x = 3 mm) to the glass plate (x = 5 mm) if the bubble sizes are larger than their resonance sizes. On the other hand, smaller bubbles move towards the pressure anti-node (x = 2 mm) instead. Based on Eq.6.2, the bubble resonance frequency as a function of bubble radius is displayed in Fig. 4.4. At 108 kHz, the bubble resonance radius is 30 μm. The theory predicts that bubbles of radii larger than 30 μm should move towards the pressure node located at x = 5 mm and bubbles smaller than this resonance size should move towards the pressure anti-node at x = 2 mm.

4.2.2 Bubble trajectory in the water layer

The trajectory of a bubble moving from the injection point towards the glass plate is shown in Fig. 4.5. The radius of the bubble was 100 μm and the driving pressure amplitude was 9.6 kPa.

Initially, a bubble is generated at the bubble injection point at 0 ms. After that, the bubble starts to escape from the bubble injection point and moves towards the glass plate. However, the bubble trajectory is not a perfect straight line but a curved one. At 164 ms, the angle between the bubble trajectory line and the glass plate

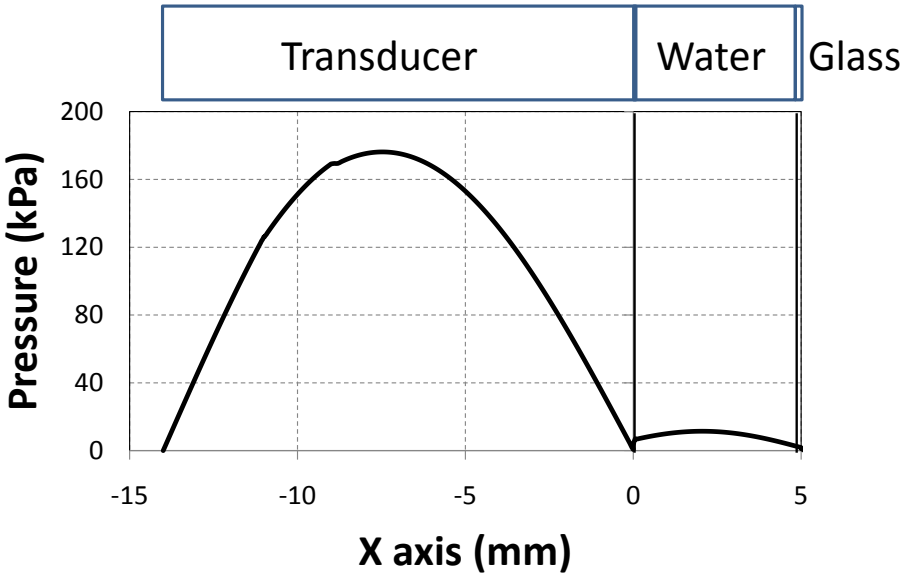

Figure 4.3: A simulated pressure distribution of the multi-layered structure (with the glass layer) at 108 kHz for input signal of 2 V.

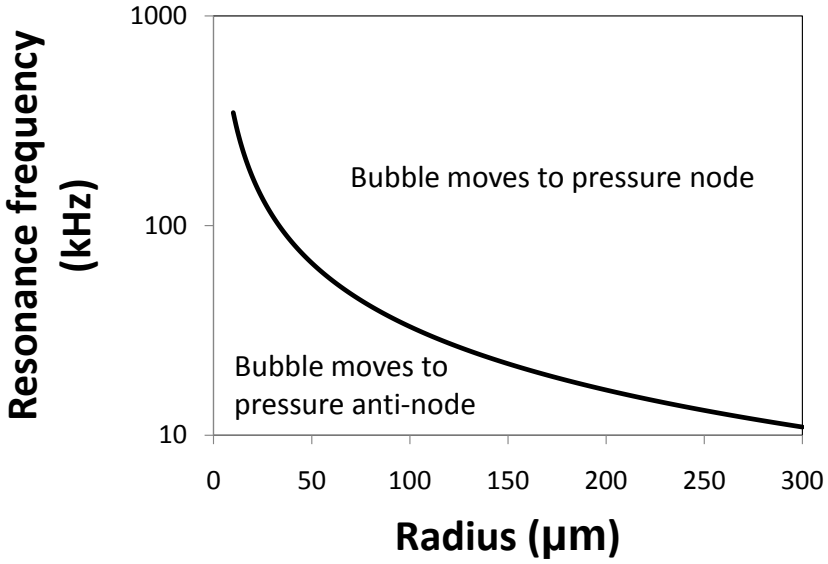

Figure 4.4: The relationship between bubble resonance frequency and bubble radius. Bubble radius ranges from 10 μm to 300 μm.

is smaller than that at 72 ms, while larger than that at 253 ms. The smaller the distance between the bubble and the glass plate, the smaller the angle between the bubble trajectory and the glass plate.

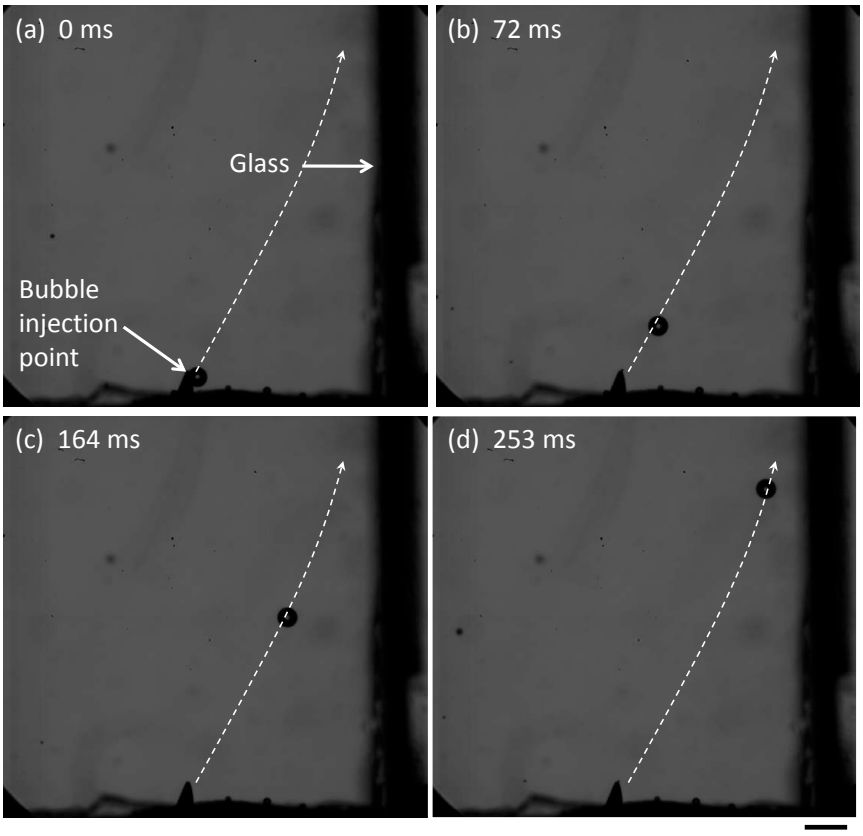

Figure 4.5: Four photo images of an experimental video result. The trajectory of a bubble moving from the injection point towards the glass plate at 108 kHz. The bubble radius is 100 μm and the pressure amplitude is 9.6 kPa. A scale bar indicating a 500 μm length in the images is displayed. (a) at 0 ms; (b) 72 ms; (c) 164 ms; (d) 253 ms.

4.3 Discussion of the experimental results

Large bubbles

Simulated trajectories are compared with the experimentally obtained ones (square dotted line) in Fig. 4.6. It may be argued that it would be elegant to show several repeatable test results rather than one trajectory for each pressure amplitude. However, the bubble size varies each time due to the coalescence of bubbles at the

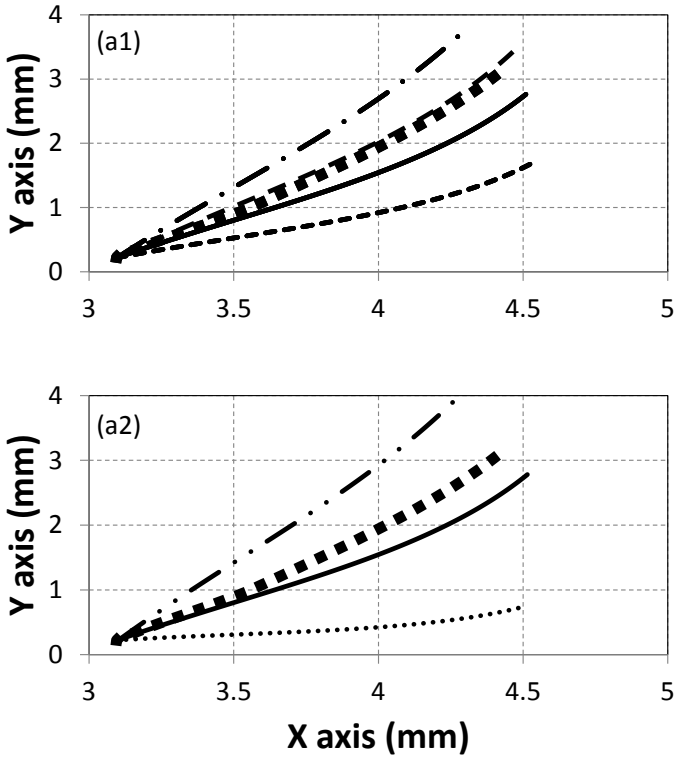
(a1)
Y axis (mm)
4
3
2
1
0
3
3.5
4
4.5
5

(a2)
Y axis (mm)
4
3
2
1
0
3
3.5
4
4.5
5
X axis (mm)

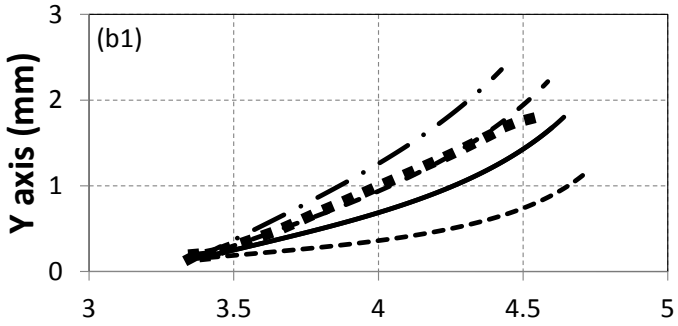
(b1)
Y axis (mm)
3
2
1
0
3
3.5
4
4.5
5

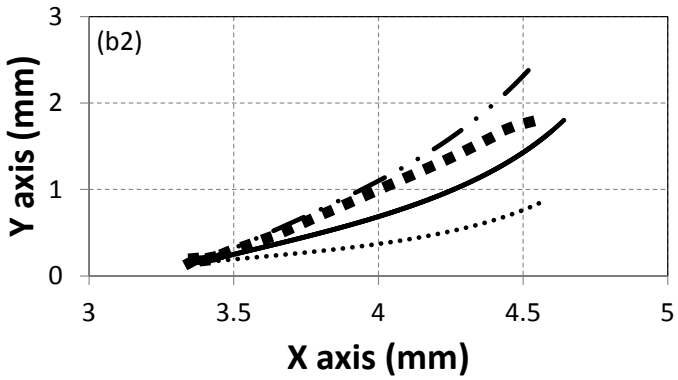
(b2)
Y axis (mm)
3
2
1
0
3
3.5
4
4.5
5
X axis (mm)

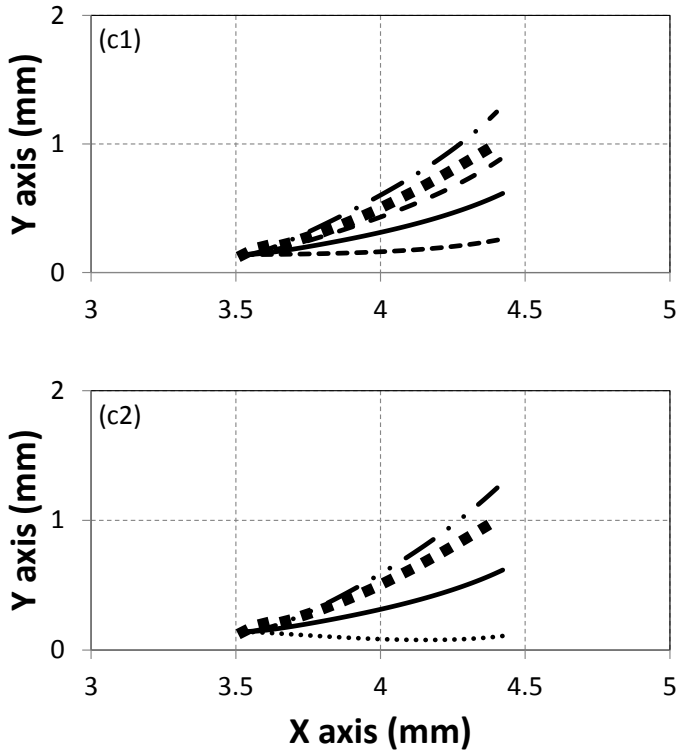

Figure 4.6: Bubble trajectories at different pressure amplitudes and the influences of pressure amplitude and bubble size on the bubble trajectory. (a1) for a large bubble (bubble radius = 100 μm), the pressure amplitudes applied are 11.52 kPa (- - -), 9.6 kPa (—), 8.64 kPa (– –) ,7.68 kPa (– · –), and 9.6 kPa for the experimental result (■); (a2) at 9.6 kPa, bubble radii are 130 μm (– · · –), 100 μm (—), 70 μm (· · ·), and 100 μm for the experimental result (■); (b1) for a large bubble (bubble radius = 167 μm), the pressure amplitudes applied are 23.04 kPa (- - -), 19.2 kPa (—), 17.28 kPa (– –) ,15.36 kPa (– · –), and 19.2 kPa for the experimental result (■); (b2) at 19.2 kPa, bubble radii are 200 μm (– · · –), 167 μm (—), 140 μm (· · ·), and 167 μm for the experimental result (■); (c1) for a large bubble (bubble radius = 217 μm), the pressure amplitudes applied are 34.56 kPa (- - -), 28.8 kPa (—), 25.92 kPa (– –), 23.04 kPa (– · –), and 28.8 kPa for the experimental result (■); (c2) at 28.8 kPa, bubble radii are 280 μm (– · · –), 217 μm (—), 160 μm (· · ·), and 217 μm for the experimental result (■). Driving frequency = 108 kHz.

injection point. It is impossible to repeatedly generate bubbles of exactly the same size every time with the present setup. Therefore, bubbles used in each experiment are different but one can still predict the bubble motion based on these results.

To illustrate the influence of pressure amplitude on the bubble trajectory, four simulated trajectories, for example, at 11.52 kPa, 9.6 kPa, 8.64 kPa and 7.68 kPa, are shown in Fig. 4.6 (a1). Increased pressure amplitudes force the bubble to move at a faster speed towards the glass plate before finally hitting it and lower the height of the bubble-glass contact point. Fig. 4.6 (a1) shows that at x = 4 mm the height of the bubble trajectory can be lowered from 2.71 mm down to about 1 mm when the pressure is increased from 7.68 kPa up to 11.52 kPa. A similar trend is also observed in Fig. 4.6 (b1) and (c1) for bubbles of radii of 167 μm and 217 μm respectively.

It is arguable that the drag force used in the present study may be different from the experiment and therefore contributes to the discrepancy between the bubble moving trajectories predicted by the theory and that of the test. The drag forces in Eq.3.17 and 3.18 are valid for estimating the dissipative force in the asymptotic limit of high Reynolds numbers. Mei et al [140] proposed an empirical drag law that matches the asymptotic limits of high and low Reynolds numbers. It was found that the use of Mei's drag law can hardly change the bubble moving trajectories but is able to shorten the time for the bubbles to move from the injection point to the target. The traveling time obtained from the test, for example, for the bubble of radius of 167 μm and driven at 19.2 kPa, is about 100 ms, which is closer to the result (90 ms) predicted by Levich's drag law [94] than that obtained from Mei's empirical equation (50 ms). The Levich's drag force is therefore used for all the calculations in this paper. Furthermore, as the bubble traveling time is sensitive to the changes of drag force, this test cell could be used for testing the effects of drag force on the bubble motion. However, the discussion of that topic is beyond the scope of the present study and more investigations could be carried out in the future.

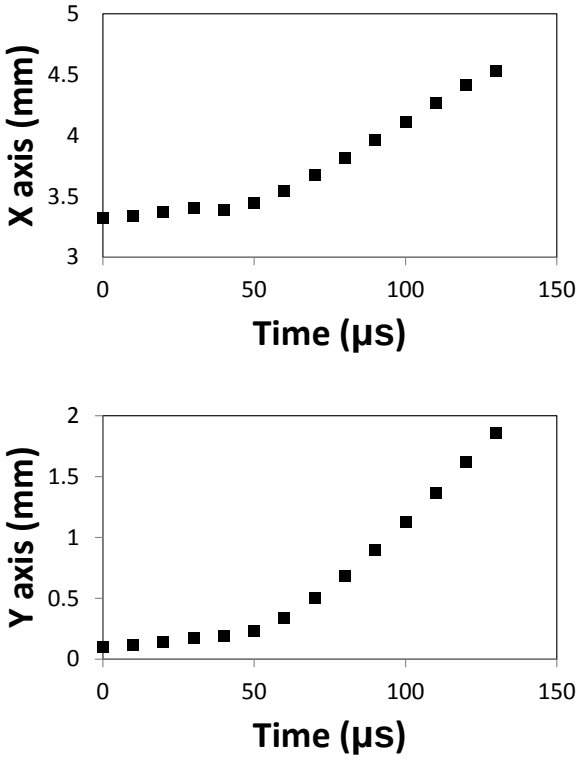

Figure 4.7: A sample trajectory of bubble in Fig. 4.6 (b1) in the x and y axes. The time step is 10 μs.

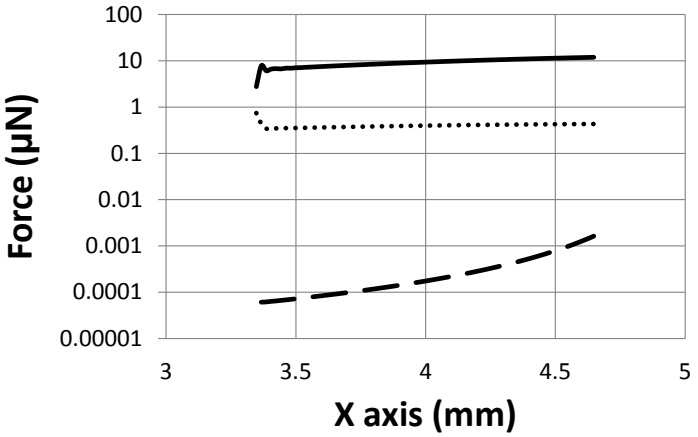

Figure 4.8: The relationship between primary Bjerknes force (—), secondary Bjerknes force ($\cdots$), and lift force ($- - -$) of bubble in Fig. 4.6 (b1).

The influence of wall on the bubble translation is also considered here. A sample trajectory of bubble in Fig. 4.6 (b1)is shown in Fig. 4.7. Besides the primary Bjerknes force, the nearby wall can exert secondary Bjerknes force and lift force on the

bubble. The relationship between these three forces with respect to x axis is shown in Fig. 4.8. It can be seen from Fig. 4.8 that the primary Bjerknes force outweigh the other two forces during the bubble's translation. This is because the secondary Bjerknes force is directly related to the bubble volume change rate ($\frac{dV}{dt}$) which is reduced at the glass surface (minimum pressure amplitude as seen in Fig. 4.3), while the lift force takes effect within a short range from the glass surface. So, their influences on the bubble translation are neglected here.

It should be noted here that the discrepancy between the experimental result and the predicated one, for example, at 9.6 kPa, may result from the viscous drag force. The main factors that influence the single bubble translation is the primary Bjerknes force and viscous drag force. As pointed out by Magnaudet and Legendre [141] that the radial pulsation increases the drag force on a bubble at moderate Reynolds number. For bubbles shown in Fig. 4.6, they are not only oscillating but also translating near a surface. The additional translation is hypothesised to increase even more drag force on the bubbles, and hence, may contribute to the discrepancy between the theory and test in Fig. 4.6. However, no current theory has included the bubble translation and oscillation at the same time in the derivation of drag force. This topic could be investigated in the future to quantify the influence of drag force on the bubble translation.

Another factor that may contribute to the observed discrepancy is hypothesized to result from the deviations of pressure amplitude calibration for the present rig. The driving frequency used here is close to the lower cutoff frequency of the hydrophone. That means the sensitivity of the hydrophone around this driving frequency is lower than that within the higher frequency range. Therefore, the measured pressure amplitude may deviate from its actual value. It can be seen from Fig. 4.6 (a1) that a predicted trajectory can be perfectly matched with the experimental result by lowering the predicted pressure by 10%, from 9.6 kPa to 8.64 kPa in this case. Similar effects can also be seen in Fig. 4.6 (b1, c1) where the experimental results are well predicted by trajectories at 10% lower pressure amplitude than the calibrated one.

As the bubble trajectory not only depends on the pressure amplitude in the water but also on the bubble size, the influence of bubble size on the bubble trajectory are

shown in Fig. 4.6 (a2, b2, c2). It can be seen from Fig. 4.6 (a2), for example, that increasing bubble radius at a fixed pressure amplitude (9.6 kPa) from 70 μm up to 130 μm results in the increase of the height of bubble trajectory at x = 4 mm from 0.42 mm to 3 mm. The original experimental result and the simulated one (for the bubble of radius of 100 μm) are also shown in the same plot for comparison.

Small bubbles

Bubbles of size smaller than their resonance size, on the other hand, are forced to move towards the pressure anti-node. Fig. 4.9 (a1), for example, shows that a bubble of radius of about 20 μm was forced to move from the injection point to the pressure anti-node at 12.8 kPa. Good agreement is also found here in Fig. 4.9 (a1) between the experimental result (square dotted line) and simulated one (solid line). The discrepancies between the theoretical predictions and experimental results can be attributed to the possible deviations in the measurement of pressure profile by the hydrophone and in the calibration of bubble size in the test. Similar to the large bubble case, the influences of pressure amplitude and bubble size on the bubble trajectory are shown in Fig. 4.9. On the one hand, the bubble trajectories are almost the same, for example, when the pressure amplitude is increased from 10.24 kPa to 15.36 kPa as shown in Fig. 4.9 (a1). On the other hand, varying bubble radius from 5 μm up to 20 μm at 12.8 kPa (Fig. 4.9 (a2)) also has limited effects on the bubble trajectories.

Moreover, it has been observed that the small bubble trajectory is not constant especially when the coalescence of small bubbles occurs along the journey. Small bubbles can combine with others and start to migrate towards the glass plate instead of the pressure anti-node when the size of the newly formed large bubble becomes large enough. As seen in Fig. 4.10, a bubble of initial radius of 17 μm moves towards the pressure anti-node before merging with another bubble to generate a new large one (bubble radius = 38 μm). The new bubble immediately reverses its moving direction and starts to travel towards the glass plate. The input pressure amplitude is 4.8 kPa. Previous studies [43, 61] have shown that the change of small bubble trajectory is due to the fact that the Bjerknes force changes its sign when the bubble size is larger than its resonance size. Coalescence processes, however, are

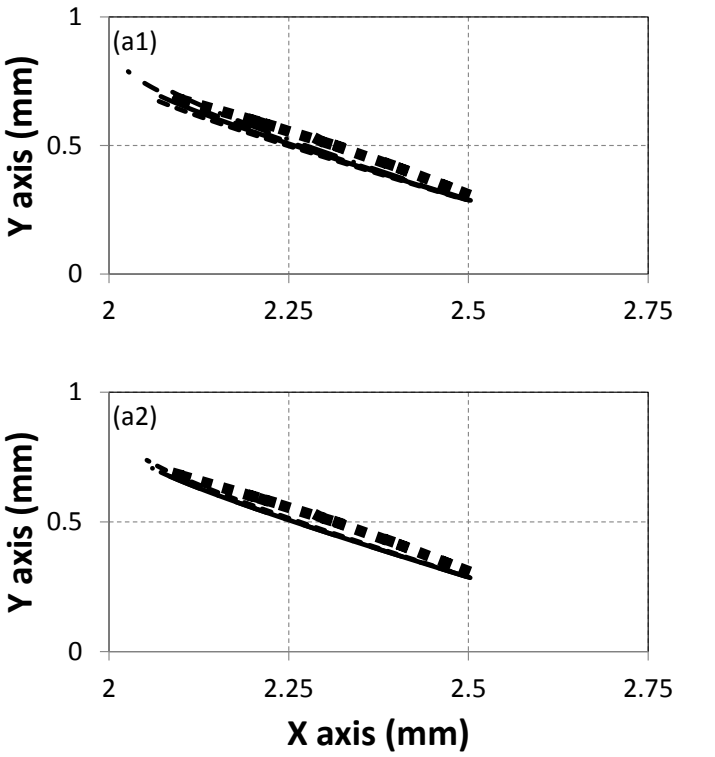
(a1)
(a2)
Y axis (mm)
X axis (mm)
1
0.5
0
2
2.25
2.5
2.75

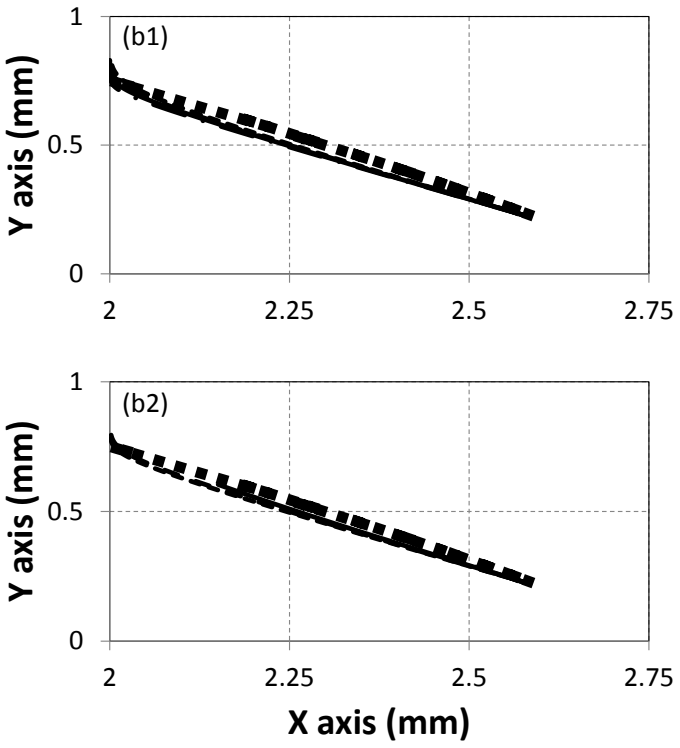
(b1)
(b2)
Y axis (mm)
X axis (mm)
1
0.5
0
2
2.25
2.5
2.75

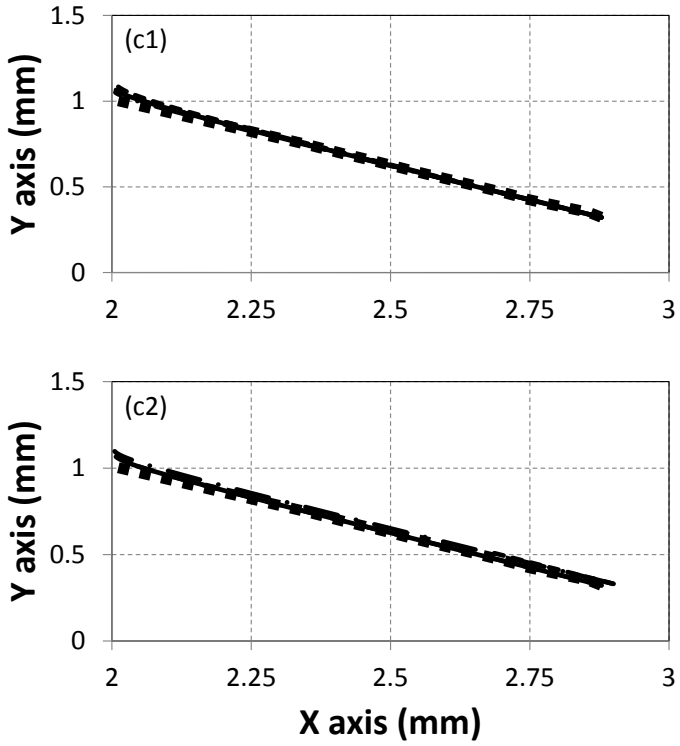

Figure 4.9: Bubble trajectories at different pressure amplitudes and the influences of pressure amplitude and bubble size on the bubble trajectory. (a1) for a small bubble (bubble radius = 20 μm), the pressure amplitudes applied are 15.36 kPa (- - -), 12.8 kPa (—), 11.52 kPa (– –) ,10.24 kPa (–·–), and 12.8 kPa for the experimental result (■); (a2) at 12.8 kPa, bubble radii are 20 μm (–··–), 10 μm (—), 5 μm (···), and 20 μm for the experimental result (■); (b1) for a small bubble (bubble radius = 20 μm), the pressure amplitudes applied are 23.04 kPa (- - -), 19.2 kPa (—), 17.28 kPa (– –) 15.36 kPa (–·–), and 19.2 kPa for the experimental result (■); (b2) at 19.2 kPa, bubble radii are 20 μm (–··–), 10 μm (—), 5 μm (···), and 20 μm for the experimental result (■); (c1) for a small bubble (bubble radius = 20 μm), the pressure amplitudes applied are 26.88 kPa (- - -), 22.4 kPa (—), 20.16 kPa (– –) ,17.92 kPa (–·–), and 22.4 kPa for the experimental result (■); (c2) at 22.4 kPa, bubble radii are 20 μm (–··–), 10 μm (—), 5 μm (···), and 20 μm for the experimental result (■). Driving frequency = 108 kHz.

not included in the bubble behavior simulations.

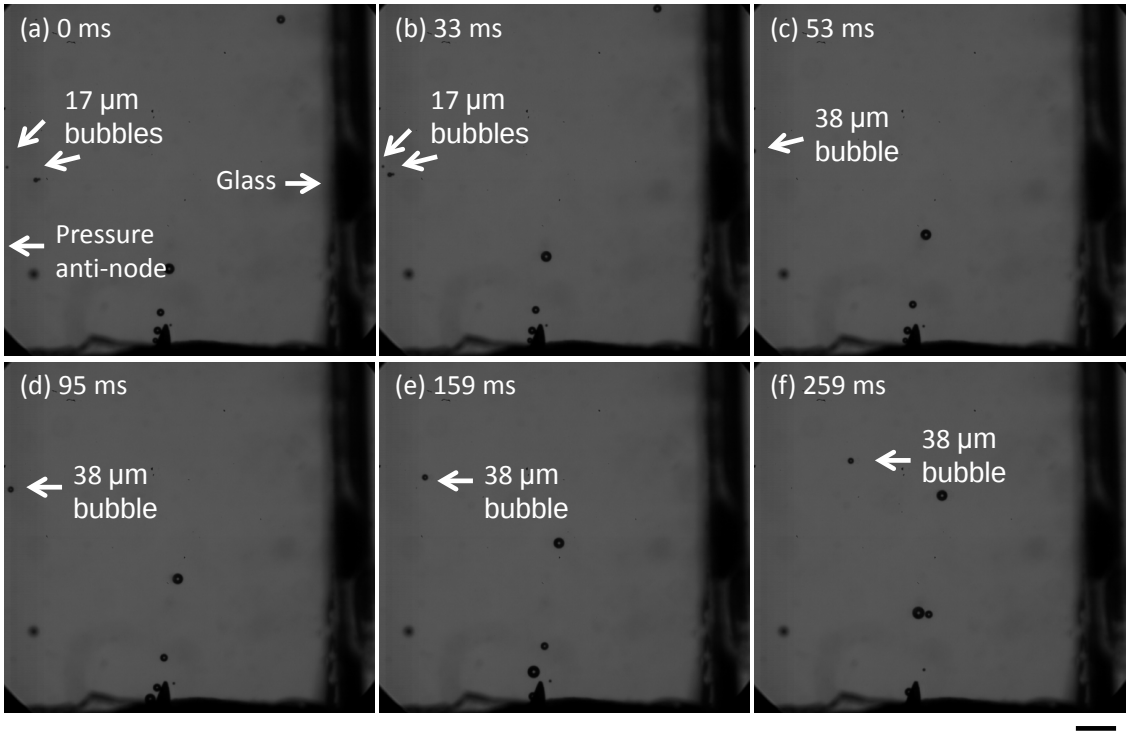

Figure 4.10: A small bubble changed its migrating direction after merging with another bubble at 108 kHz. Input pressure amplitude is 4.8 kPa. A scale bar indicating a 500 μm length in the images is displayed. (a)0 ms; (b)33 ms; (c)53 ms; (d)95 ms; (e)159 ms; (f)259 ms.

4.4 Conclusion

This chapter discussed the mechanism of single bubble transportation in a weak acoustic standing wave field. The designed test cell, which creates a one-dimensional uniform pressure field across the cross section of the whole stack, is ideal for testing the effects of an acoustic field on the bubble motion, which can be manipulated in a very controlled manner since the pressure field can be accurately predicted by a 1D matrix model.

As the pressure field within the test cell can be accurately quantified, it was possible to use the test cell to test the theory of bubble motion (e.g modified Keller-Miksis equation and Newton's second law) and predict the influence of factors, such as different pressure amplitudes or different bubble sizes, on the bubble translational

trajectory. Good agreement was found between the theory and the experiment. It was observed, on the one hand, that the trajectories of bubbles driven above resonance were strongly influenced by the pressure amplitude and bubble size. Both an increase of pressure amplitude and a decrease of bubble size forced the bubbles to arrive at the target plate at lower heights. On the other hand, the trajectories of bubbles driven below resonance stayed constant and only little differences of the bubble trajectories were found as a function of pressure amplitude or bubble size. Moreover, as the traveling time of bubbles moving from the injection point to the target plate is sensitive to the changes of drag force, it is possible to use the test cell to quantify the drag force and study its effects on the bubble motion. This was only illustrated in this chapter but could be comprehensively studied in the future.

Chapter 5

Multi-bubble translation

In real life ultrasonic cleaning process, a large quantity of micro-bubbles need to be transported to a contaminated surface. Previous works, however, mainly focused on the single bubble translation case. In the multi-bubble transportation, neighboring bubbles interact with each other during their translations. The complicated bubble-bubble interactions make it difficult to understand the multi-bubble translation in an acoustic standing wave field. The mechanism of multi-bubble translation is still unknown. Therefore, this chapter discusses the multi-bubble transportation near a surface, and establishes a model which explains the multi-bubble translation by expressing the balance between Bjerknes forces and hydrodynamic forces on a bubble in a liquid medium. The observed bubble movement trajectories are quantitatively in good agreement with the theoretical predictions.

5.1 Experimental configuration

An improved test rig was designed for the multi-bubble translation study. The main parts of the resonator were a liquid (deionized water) cube held in a brass block (Length $*$ Width $*$ Thickness = 10 mm by 10 mm by 8 mm) and a round transducer with diameter of 10 mm (Fig. 5.1). The origin of the coordinate system (x = 0 mm, y = 0 mm, z = 0 mm) was set at the center of the transducer-liquid interface. In order to make it possible to optically observe the inside of the cell, the cross section

of the water layer was chosen as a square shape (10 mm by 10 mm) and two glass windows were fitted on both sides of the liquid medium. Since the aim of the present work is to investigate the bubble behavior near a surface, a round borosilicate glass plate (glass 1) of 0.1 mm thickness (VWR, UK) was placed at x = 4 mm as the target surface and another glass plate (glass 2 at x = 8 mm) was used to confine the liquid within the structure. The transducer was fabricated out of a lead zirconate titanate (PZT) disk (PCM 51, EP Electronic Components Ltd, UK), a backing brass bar, a front brass bar with thickness of 4 mm, 13 mm and 15 mm respectively.

An electrolysis method was used to generate bubbles of radii ranging from 10 to 50 μm. Two wires (tin-coated copper) were connected to a DC power supply (TNG 35, Voltcraft, Germany) and the electrical potential was set to 5 V. The free ends of the wires were placed at x = 5 mm as shown in Fig. 5.1. It was found that when the sound field was switched off, bubbles could freely float away from the tip of the tin-coated copper wire and form a chain of bubbles. However, in the presence of an acoustic field, the bubbles accumulate at the wire tip. To prevent the coalescence of bubbles, the bubbles used in the experiments were generated before the sound field was on.

The bubble motion was recorded by a high speed camera (FastCam SA5, Photron, USA) at a frame rate of 100,000 frames/second. A viewing window with size of 3 mm by 1.8 mm was chosen to cover the cross section of glass 1 (x = 4 mm) and the bubble injection point (x = 5 mm) at the same time. The recorded bubble translation as a function of time was analyzed by an object tracking algorithm written in Matlab (Mathworks Inc, USA). The dimensions of objects in a video were calibrated with a standard 300 μm width stick.

5.2 Results

5.2.1 The acoustic standing wave field

It has been shown in the previous chapter that the one-dimensional equivalent electrical network of a transducer (1D model) is suitable for quantifying the pressure

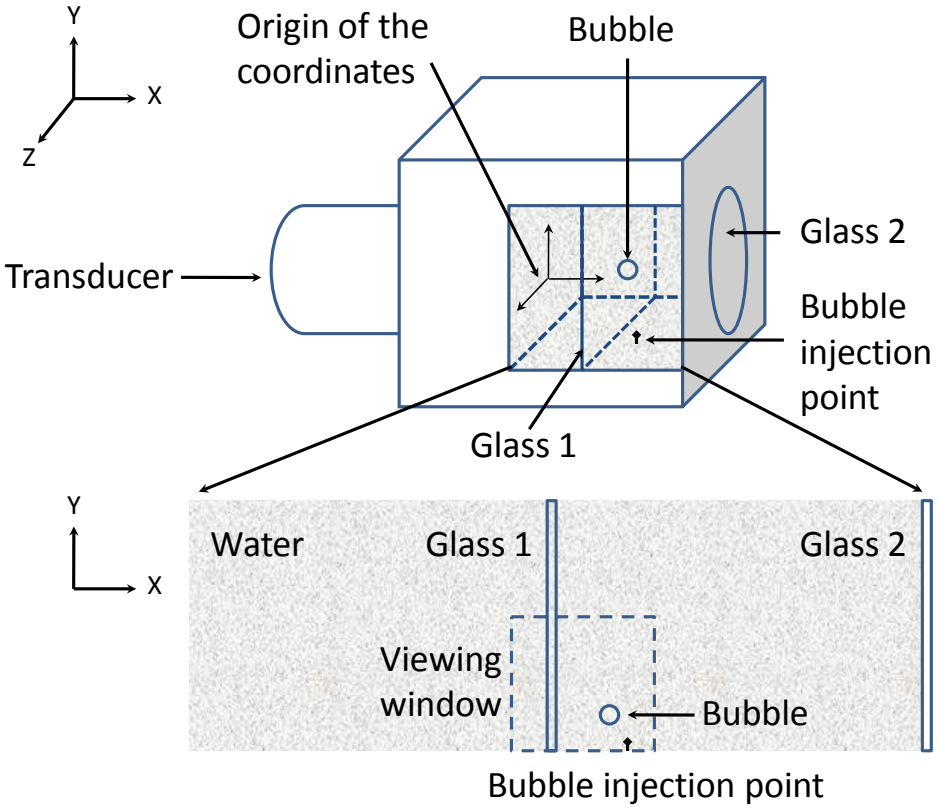

Figure 5.1: A schematic diagram of the multi-layered resonator for multi-bubble transport.

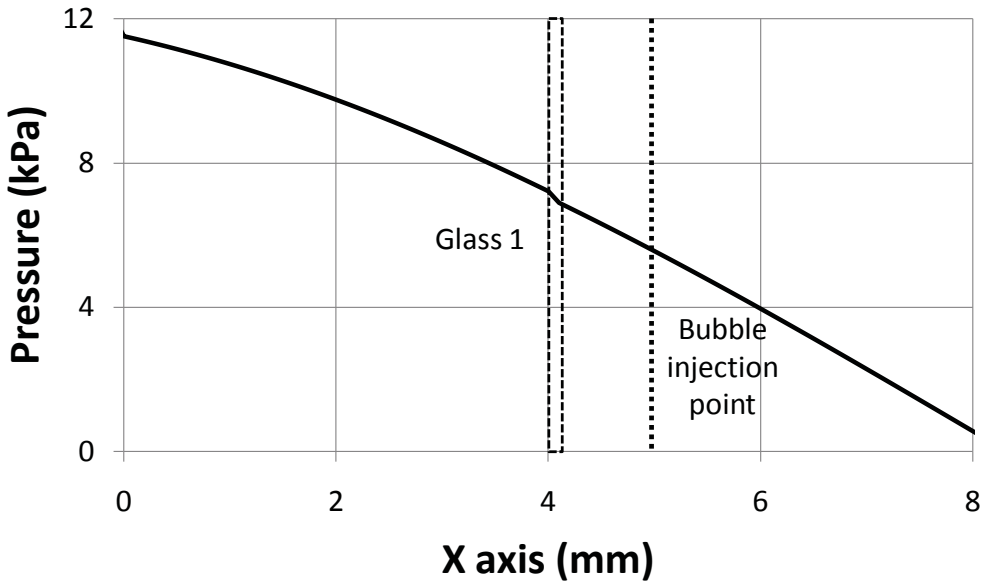

Figure 5.2: A simulated pressure distribution in the water layer with glass 1 at 46.8 kHz for input amplitude of 4 V. The position of glass 1 is indicated by the dashed square and the bubble injection point is shown by the dotted line.

distribution of the present resonator. A simulated pressure distribution of the water layer with glass 1 at 46.8 kHz is displayed in Fig. 5.2 for input signal amplitude of 4 V (peak). It can be seen from Fig. 5.2 that a calculated maximum pressure amplitude of 11.5 kPa is located at the origin of the coordinate system (x = 0 mm in Fig. 5.1) and the pressure amplitude gradually drops to a minimum at the boundary between the water layer and glass 2 (x = 8 mm) as indicated in Fig. 5.2.

Since the thickness of glass 1 in Fig. 5.2 is much smaller than the acoustic wavelength here, little energy is reflected back from the glass surface. The glass plate can then be treated as acoustically transparent. On the other hand, the existence of glass 1 imposes a physical barrier in the liquid. The normal liquid velocity (it is important to note that the mean flow velocity is meant here and not the acoustic particle velocity) on the glass surface is constrained to be zero in this case. To fulfil the zero mean normal flow velocity condition on the glass surface, an imaginary bubble is introduced on the other side of the glass plate to replace it [142]. The previous bubble-wall system is now converted to a bubble-bubble system without the wall. Let us suppose a bubble approaches a wall in the absence of ultrasound. Due to the no-slip boundary condition, the flow field around the bubble is the superposition of the field of a free oscillating bubble and that produced by a mirror bubble [143]. In the presence of a sound field, the flow field near the wall is the combination of the field that is generated by the real bubble's translation and oscillation. To achieve the normal zero flow velocity on the wall surface, the mirror bubble needs to oscillate correspondingly. The mirror bubble here is inserted into the model to account for the low frequency mean flow boundary condition that the thin plate introduces to the system (as is done in the fluid mechanics literature. see [142]). The presence of the thin plate alters the flow field around the bubble, which will influence the forces that are acting on the bubble. The introduction of the mirror bubble allows the correct modelling of the flow field around the bubble and it is hypothesised that the resulting forces due to the flow field (near the interface) on the bubble can be modelled by a bubble-bubble interaction similar to that which is used when calculating Bjerknes forces for bubble-bubble interactions in the bulk. This is what was modelled here and the experimental results show reasonably good agreement with this approach as there is obviously a large force acting on the bubble that attracts the bubble onto the plate surface.

At this point, it is important to point out that this might seem contradictory to the explanation of a Bjerknes force acting between a bubble and itself near a perfectly acoustically reflecting boundary (where it is argued that the pressure field that the bubble emits reflects from the interface and interacts with the bubble itself to produce the Bjerknes force). Since in our case the thin plate does not reflect the acoustic pressure it would be inconsistent to argue that a Bjerknes force acts between the bubble and its image, since the thin plate does not reflect the acoustic energy. However, it is argued here that the force that the bubble sees is an effect due to the distorted fluid flow field around the bubble (that is caused by the thin plate) and the introduction of the mirror bubble and its 'Bjerknes' force is only used as a means to describe this effect. An in depth proof of this is beyond the scope of this thesis, it is most likely that both of these assumptions are too simplistic and the truth lies somewhere in between, especially when considering that in real life the plate is elastic and can deform. However experimental results show that a strong force acts on the bubble near the interface and the Bjerknes force calculation of the bubble with its mirror seems to obtain the right order of magnitude of the force.

It is worth mentioning here that the resonance frequency of a bubble attached to a wall is different from that in a free space as presented by Eq. 6.2. The influence of a wall on the bubble resonance frequency, however, is directly related to the separation distance between the bubble and the wall. For a bubble oscillating near a surface, its angular resonance frequency (ω_{wall}) is related to the free resonance frequency (ω_0) by $\omega_{wall} \sim \omega_0/\sqrt{1+2R_0/d_w}$, where d_w is the separation distance from the wall [147, 148]. The initial separation distances as shown in the present study were at least ten times larger than the bubble diameter which means the ω_{wall} would be approximately equal to its free space resonance. Moreover, the bubbles were driven well below their resonance frequencies and their sizes were considered to be relatively small. Thus, the bubbles were anticipated to translate towards the glass 1 from the bubble injection point at x = 5 mm.

5.2.2 Bubble translation in the acoustic standing wave field

The translations of several bubbles moving from the bubble injection point towards glass 1 (Fig. 5.1) are displayed in Fig. 5.3 at a pressure amplitude of 11.5 kPa. The

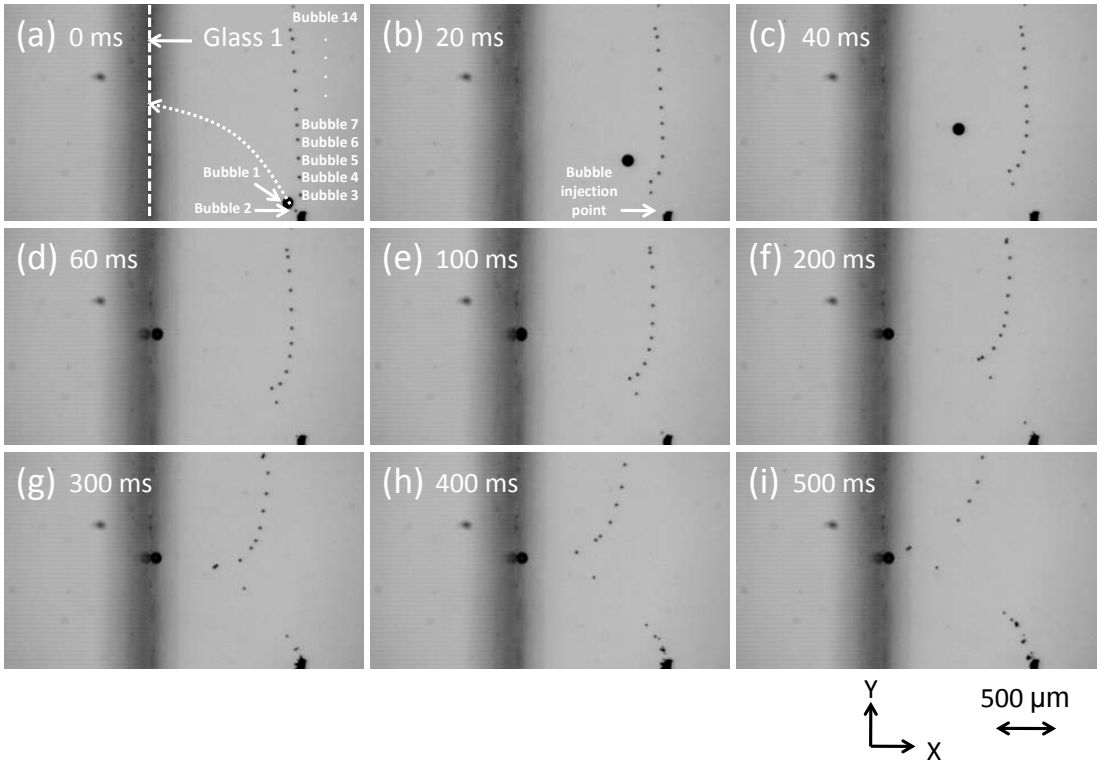

Figure 5.3: Selected frames from a video showing the translations of several bubbles from the injection point to glass 1 at (a) 0 ms; (b) 20 ms; (c) 40 ms; (d) 60 ms; (e) 100 ms; (f) 200 ms; (g) 300 ms; (h) 400 ms; (i) 500 ms. The pressure amplitude is 11.5 kPa.

radius of bubble 1 in Fig. 5.3 is 42 μm, and the radii of the other bubbles are around 13μm.

Initially, bubble 1 (labelled in Fig. 5.3 (a)) moves towards glass 1 at a faster speed than bubbles 2 – 14. After 60 ms, bubble 1 firstly arrives on glass 1, while the following bubbles 2 – 14 are moving on trajectories towards glass 1 and starting to form an arrow shape in the liquid medium. Bubble 3 and 4 are the first two to merge with bubble 1 at 400 ms followed by bubbles 5, 2, 6, and 7 sequentially.

5.3 Discussion of the experimental results

The translation of a bubble in a liquid medium is the outcome of the competition of different external forces. The bubble motion is sensitive to the changes of surrounding environment, such as the presence of neighboring bubbles and boundary

surfaces. In this section, the translations of bubbles are investigated by analyzing the relationship between acoustic and hydrodynamic forces exerted on the bubbles. All the bubble translations shown in Fig. 5.3 were studied and bubbles 1, 3, 5, and 7 are chosen here to illustrate the force relationship. The influence of bubble size and pressure amplitude on the bubble translation is also explored.

5.3.1 The translation of bubble 1

Recalling the force analysis in section 3.4, the translation of bubble 1 can be examined in the x and y axes respectively and the relationship of several main external forces in the x axis is shown in Fig. 5.4 (e).

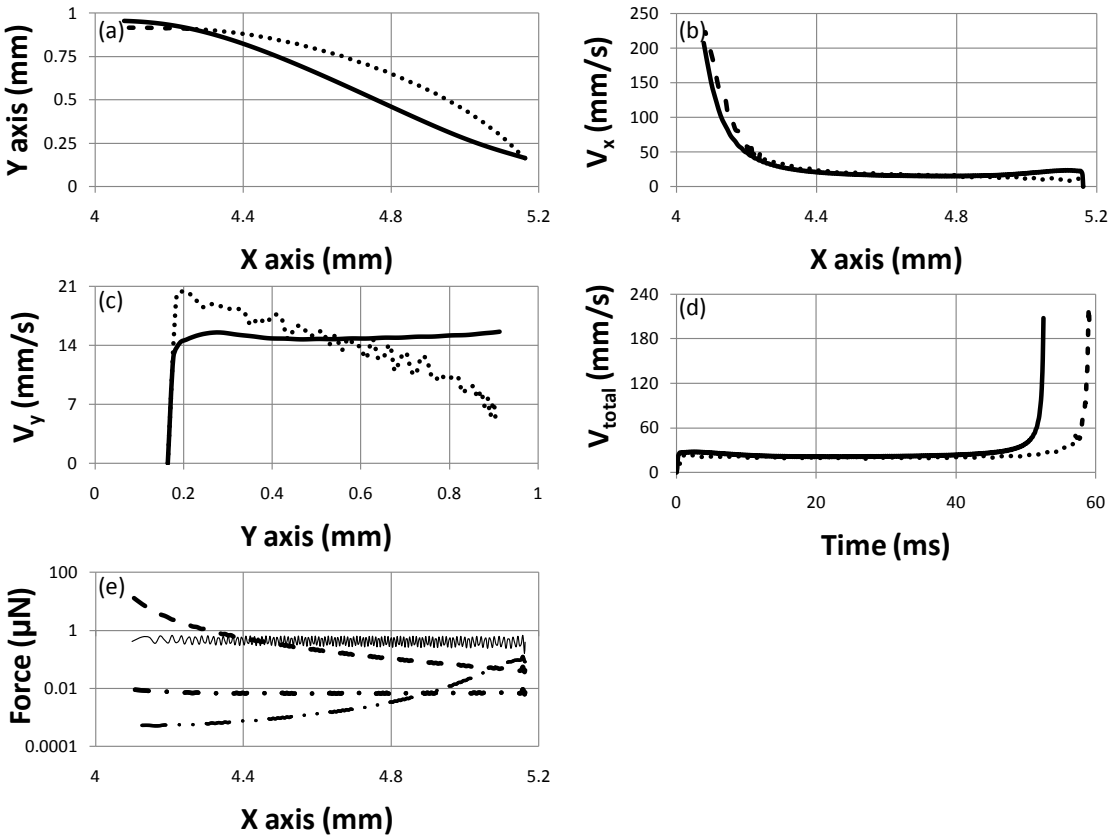

Figure 5.4: The translation of bubble 1 at 46.8 kHz (a) bubble trajectory, experimental result ⋯, theoretical prediction –; (b) velocity in the x axis, experimental result ⋯, theoretical prediction –; (c) velocity in the y axis, experimental result ⋯, theoretical prediction –; (d) total velocity, experimental result ⋯, theoretical prediction –; (e) relationship between different forces, primary Bjerknes force –, secondary Bjerknes force from glass 1 – –, secondary Bjerknes force from glass 2 – ⋯ –, secondary Bjerknes force from bubble 2 – · –. The pressure amplitude was 11.5 kPa.

In the x axis, after the ultrasound is switched on, bubble 1 is mainly controlled by the primary Bjerknes force and starts to move in the direction towards glass 1 from the bubble injection point. It can be seen from Fig. 5.4 (b) that the velocity of bubble 1 in the experiment suddenly rises from 0 to 16 mm/s and then maintains the speed until arriving at x = 4.4 mm. After that, the secondary Bjerknes force from glass 1 grows stronger and starts to outweigh the primary Bjerknes force. The secondary Bjerknes force from glass 2 and a nearby bubble 2 can be neglected at this stage. The velocity of bubble 1 surges up from 20 mm/s at x = 4.4 mm to 207 mm/s at x = 4.07 mm. Good agreement is found between the experiment and theoretical prediction of the x axis velocity of bubble 1.

In the y axis, it is anticipated that the buoyancy force is stronger than the drag force at the beginning, but later on a balance is reached between the two forces. From the theory, bubble 1 is expected to move at a steady speed of 15 mm/s after taking off from the bubble injection point. However, in the experiment, the velocity of bubble 1 witnesses a rise from 0 mm/s at y = 0.16 mm to 20 mm/s at y = 0.18 mm followed by a gradual drop to 6 mm/s at y = 0.89 mm. From the point of view of force, it is possible that the primary Bjerknes force on bubble 1 is weaker than expected since the standing wave field has not been fully established at the moment when the sound field is switched on. In the later phase, especially when bubble 1 is moving close to glass 1, the full strength primary Bjerknes force and the attractive force from glass 1 greatly accelerate the bubble motion in the x axis which in turn shortens the traveling distance in the y axis over the same period. The velocity in the y axis, therefore, is decreasing when bubble 1 is approaching glass 1. This effect can also be seen in the time lag of the traveling time between theory and experiment (Fig. 5.4 (d)). In the experiment, the time for bubble 1 to move from the bubble injection point to glass 1 is 60 ms which is longer than the 52 ms from the theory due to the insufficient primary Bjerknes force experienced by bubble 1 at the beginning.

5.3.2 The translations of bubbles 3, 5, and 7

It can be seen from Fig. 5.3 that bubbles 2 – 14 move at a much slower speed than bubble 1 and their translations behave in a different manner. To explain such behavior, bubbles 3, 5, and 7 are chosen here as the example bubbles because they

represent the typical translational behavior experienced by all other bubbles.

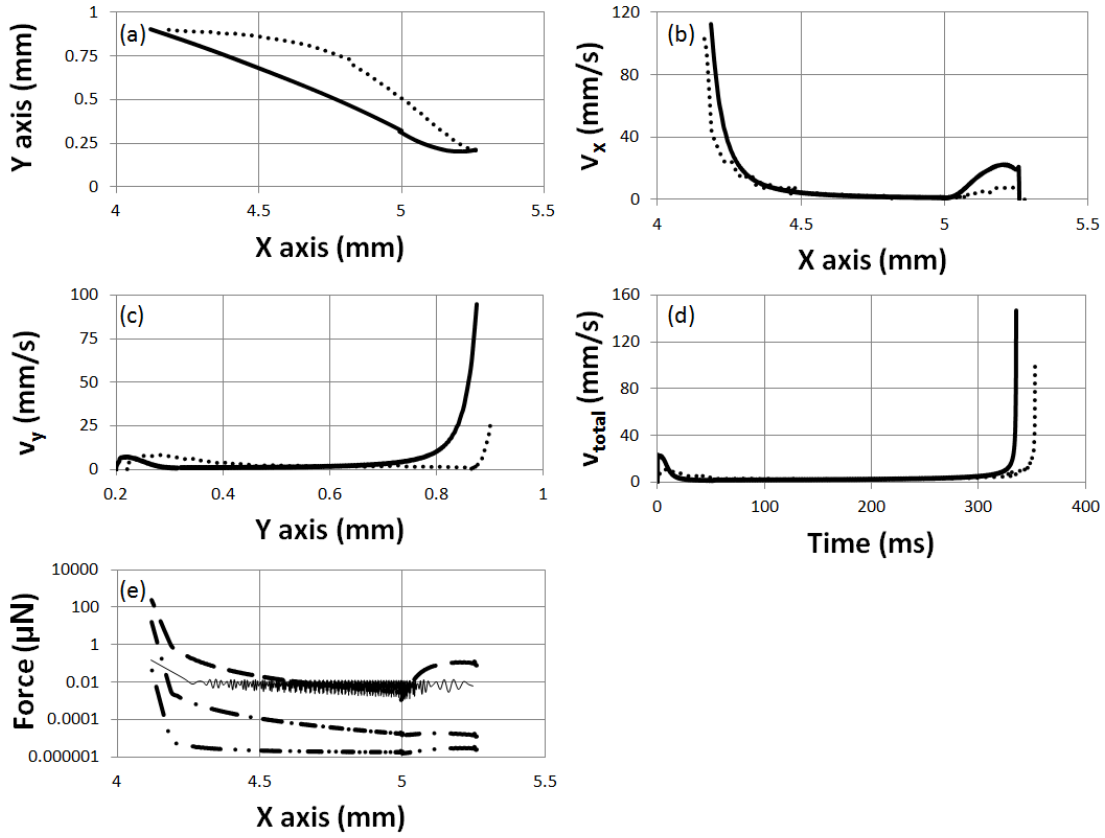

Figure 5.5: The translation of bubble 3 at 46.8 kHz (a) bubble trajectory, experimental result ···, theoretical prediction –; (b) velocity in the x axis, experimental result ···, theoretical prediction –; (c) velocity in the y axis, experimental result ···, theoretical prediction –; (d) total velocity, experimental result ···, theoretical prediction –; (e) relationship between different forces, primary Bjerknes force –, secondary Bjerknes force from glass 1 – –, secondary Bjerknes force from glass 2 – · ·–, secondary Bjerknes force from bubble 2 – · –. The pressure amplitude was 11.5 kPa.

By decomposing the external forces into the x axis force and y axis force, one can study the bubble translation using the same procedure as for bubble 1. Initially, the motion of bubble 3 in the x axis, for example, is mainly controlled by the secondary Bjerknes force from bubble 1. When bubble 1 and 3 are still close to each other, this secondary Bjerknes force is stronger than the primary Bjerknes force and results in a surge in velocity in the x axis (Fig. 5.5 (b)). As bubble 1 is moving at a faster speed towards glass 1, the distance between bubble 3 and 1 grows to the extent that such bubble-bubble interaction is weaker than the primary Bjerknes force. The predicted velocity in the x axis, therefore, decreases from 20 mm/s at x = 5.25 mm

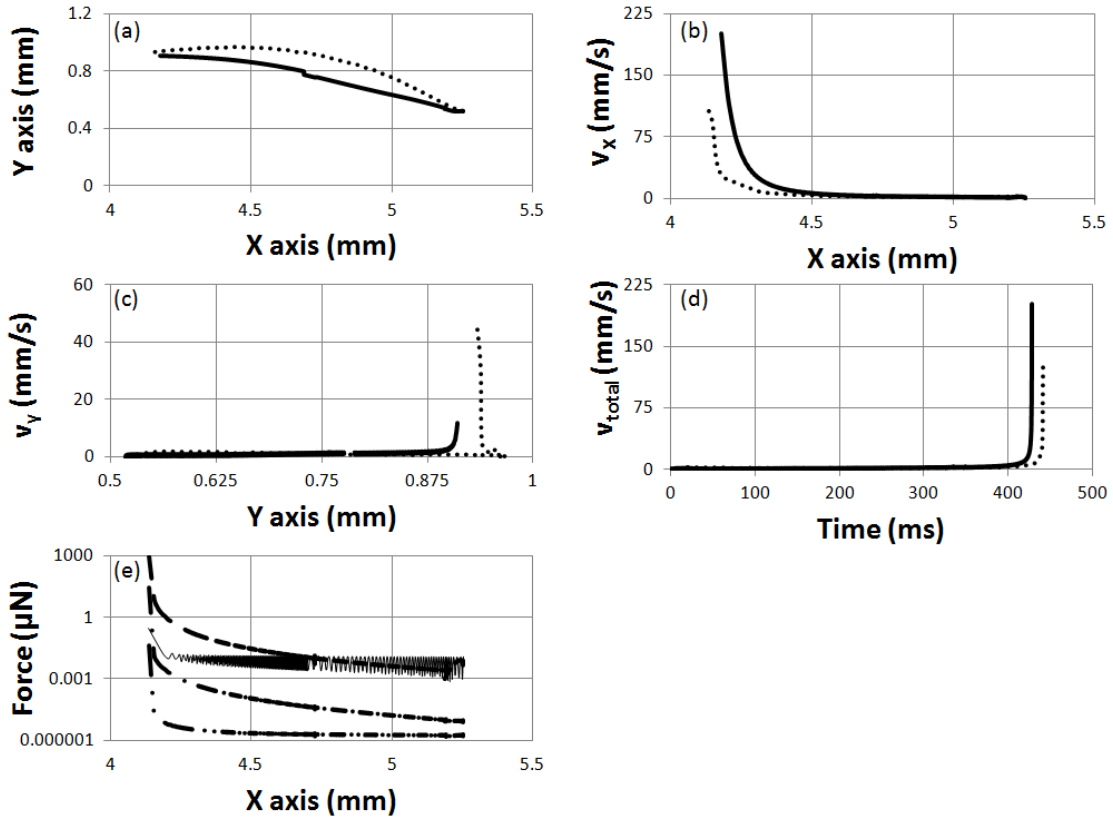

Figure 5.6: The translation of bubble 5 at 46.8 kHz (a) bubble trajectory, experimental result ⋯, theoretical prediction –; (b) velocity in the x axis, experimental result ⋯, theoretical prediction –; (c) velocity in the y axis, experimental result ⋯, theoretical prediction –; (d) total velocity, experimental result ⋯, theoretical prediction –; (e) relationship between different forces, primary Bjerknes force –, secondary Bjerknes force from glass 1 – –, secondary Bjerknes force from glass 2 – ⋯ –, secondary Bjerknes force from bubble 2 – · –. The pressure amplitude was 11.5 kPa.

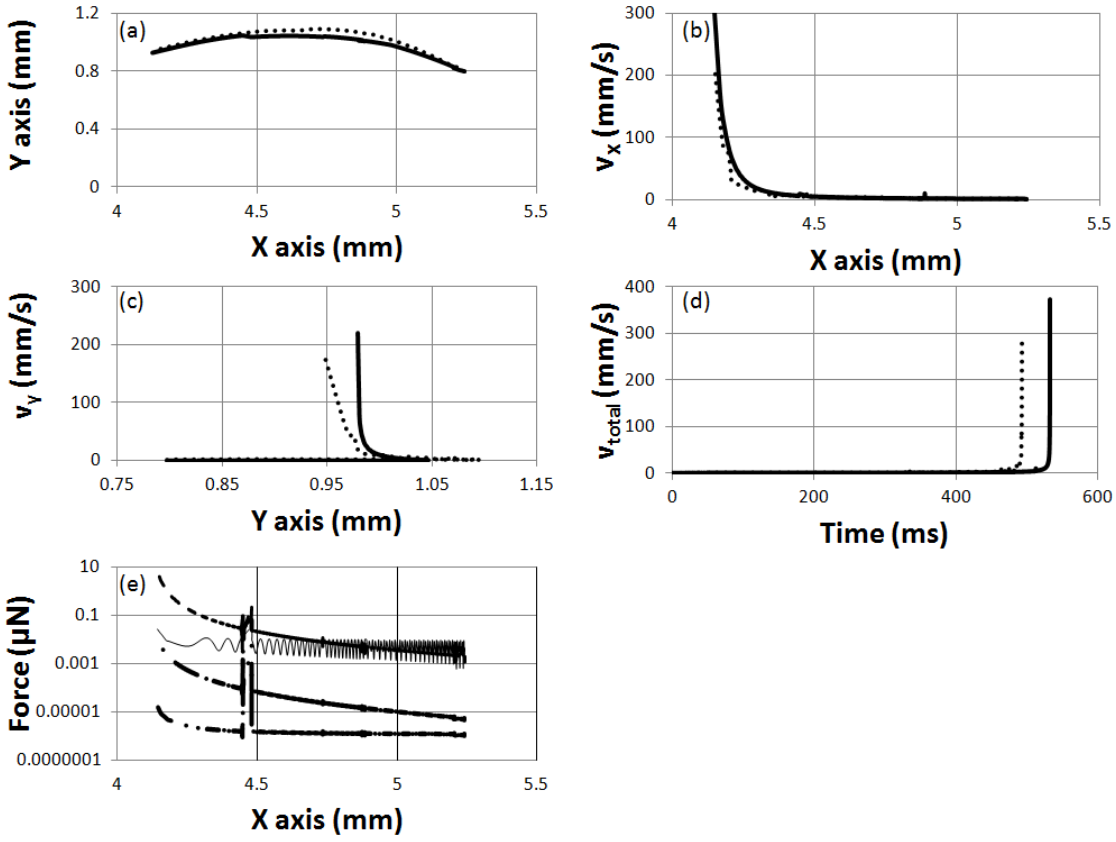

Figure 5.7: The translation of bubble 7 at 46.8 kHz (a) bubble trajectory, experimental result ···, theoretical prediction –; (b) velocity in the x axis, experimental result ···, theoretical prediction –; (c) velocity in the y axis, experimental result ···, theoretical prediction –; (d) total velocity, experimental result ···, theoretical prediction –; (e) relationship between different forces, primary Bjerknes force –, secondary Bjerknes force from glass 1 – –, secondary Bjerknes force from glass 2 – · ·–, secondary Bjerknes force from bubble 2 – · –. The pressure amplitude was 11.5 kPa.

to 4 mm/s at x = 5 mm, while in the experiment the change of velocity over the same period is smaller than the expectation but is still noticeable. From Fig. 5.5 (a), it can be seen that the predicted trajectory of bubble 3 between x = 5.25 to 5 mm also deviates from the experimental result. As discussed in the bubble 1 case, at the beginning of the experiment, the standing wave field in the experiment is weaker than the theoretical prediction which forces bubble 1 to move away from the anticipated trajectory. The trajectory of bubble 3 is consequently changed because the secondary Bjerknes force between bubble 1 and 3 dominates the translation of bubble 3 over that period. However, the shape of the velocity profile between x = 5.25 to 5 mm in the experiment is still consistent with that of the theory.

After the arrival of bubble 1 on to glass 1, the primary Bjerknes force and the secondary Bjerknes force from bubble 1 become the major factors that control the translation of bubble 3. The velocity of bubble 3 in the x axis between x = 5 mm and x = 4.5 mm is around 3 mm/s. When the distance between bubble 3 and bubble 1 decreases, the secondary Bjerknes force from bubble 1 is again dominating the motion of bubble 3 in the x axis. Moreover, within the near field of bubble 1, the secondary Bjerknes force from glass 1 becomes stronger than the primary Bjerknes force and contributes to the boost of velocity along with the interaction force between bubble 1 and 3. The velocity of bubble 3 jumps from 3 mm/s at x = 4.5 mm/s to 90 mm/s at x = 4.18 mm, which is close to the predicted 112 mm/s.

In the y axis, initially, bubble 3 is lifted by the attractive force from bubble 1 and the buoyancy force. As bubble 1 is moving away at a faster speed, the bubble 1 and 3 interaction diminishes as a function of time and the y axis velocity of bubble 3 remains at 3 mm/s between y = 0.17 and 0.7 mm in Fig. 5.5 (c). After that, the attractive force from bubble 1 significantly accelerates the velocity when bubble 3 approaches bubble 1. A 94 mm/s velocity is seen in the theoretical prediction at y = 0.88 mm which is higher than the 27 mm/s one observed in the experiment. Since bubble 3 moves on a trajectory which is not perfectly matching the theoretical prediction, the consequent bubble translation, especially at the moment when bubble 1 and 3 are close enough, could be different from what is expected from the theory. Therefore, the y axis velocity in the experiment is different from that of the simulation. The predicted overall traveling time for bubble 3 to move from the

bubble injection point to glass 1 is in quantitative agreement with the experimental result as shown in Fig. 5.5 (d).

A similar analysis was also applied to bubble 5 and 7 in Fig. 5.6 and Fig. 5.7 respectively. A surge of x axis velocity due to the increase of secondary Bjerknes force from the surface is seen for both bubbles in Fig. 5.6 (b) and Fig. 5.7 (b). The observed maximum x axis velocity of bubbles 5 and 7 are 109 and 214 mm/s respectively, which are lower than the anticipated 200 and 300 mm/s from the model. Ideally, the detection of velocity change, especially at the moment when the bubble is approaching the boundary, requires a high frame rate. However, the limited frame rate used in the experiment was unable to provide the small time interval to construct the accurate velocity information at the final moment when the bubble is contacting the surface and therefore results in a lower than expected x axis velocity in Fig. 5.6 (b) and Fig. 5.7 (b).

It needs to be pointed out here that the influence from bubble 1 on the nearby bubbles decreases with an increase of separation distance between the bubbles. For the bubbles in the far field of bubble 1, a weaker attractive force generated from bubble 1 was anticipated. It can be seen from Fig. 5.7 that since bubble 7 moves at a slow speed, the standing wave field has sufficient time to be established in the x axis. The predicted translation of bubble 7, therefore, is in good agreement with the experimental result. On the other hand, there is a discrepancy of bubble trajectory between the experiment and the prediction for bubble 5 in Fig. 5.6 (a) which is the consequence of the deviation between the observed and calculated trajectory of bubble 1 as shown in Fig. 5.4 (a).

5.3.3 Parametric study

To transport a large amount of bubbles of given size to an appointed position on a surface, one needs to optimize the external forces exerted on the bubbles, such as primary and secondary Bjerknes forces. In section 3.3, it is seen that the Bjerknes forces are directly related to the bubble size and external pressure amplitude. In this section, the influence of different bubble sizes and pressure amplitudes on the bubble translation is discussed.

The translation of the 13 μm bubbles are sensitive to the changes of acoustic and hydrodynamic forces. Let us assume a bubble 1 of radius of 42 μm is fixed on glass 1 at x = 4 mm, y = 0.9 mm, and another bubble 2 can move freely in the water layer. The driving frequency is kept at 46.8 kHz. The calculated forces in Fig. 5.8 (a2, b2, c2) are represented by their absolute values.

Firstly, three radii of bubble 2, 6.5 μm, 13 μm, and 26 μm, are used in Fig. 5.8 (a1, a2) at 11.5 kPa. Fig. 5.8 (a1) shows that changing the radius of bubble 2 can hardly alter its trajectory. The secondary Bjerknes force between bubble 1 and 2 is proportional to their sizes and therefore an increase of the size of bubble 2 results in an increase of secondary Bjerknes force as well, which in turn accelerates the velocity of bubble 2. The traveling time of bubble 2 was found from our calculations to be shortened from 2500 ms for the 6.5 μm bubble to 100 ms for the 26 μm one.

Secondly, the radius of bubble 2 is assumed to be 13 μm, and the radius of bubble 1 is varying from 25 μm to 100 μm. The pressure amplitude is 11.5 kPa. A striking difference of bubble 2 trajectory is noticed in Fig. 5.8 (b1). Bubble 2 experiences much less secondary Bjerknes force from the 25 μm bubble 1 than from the 100 μm one. The 100 μm bubble exerts a repulsive instead of attractive force on bubble 2. It is well-known that the secondary Bjerknes force between two bubbles can shift from an attractive force when the bubbles are oscillating in phase, to a repulsive force when their oscillations are out of phase [53, 137]. Based on Eq.6.2, at 46.8 kHz, the 100 μm bubble is driven above its resonance frequency, while bubble 2 is smaller than the resonance size. Therefore, the secondary Bjerknes force between these two bubbles shifts from an attractive one to a repulsive one in the 100 μm (bubble 1) case.

Thirdly, the radii of bubble 1 and 2 are kept as 42 μm and 13 μm respectively. The pressure amplitude is increased from 5.25 kPa to 23 kPa (Fig. 5.8 (c1, c2)). At a lower pressure amplitude, bubble 2 experiences a smaller secondary Bjerknes force from bubble 1 which only starts to divert the trajectory of bubble 2 within the near field (Fig. 5.8 (c1)). At a higher pressure amplitude, the bubble 2 migrates directly towards bubble 1 at a faster speed due to the increase of interaction between the bubbles (Fig. 5.8 (c2)).

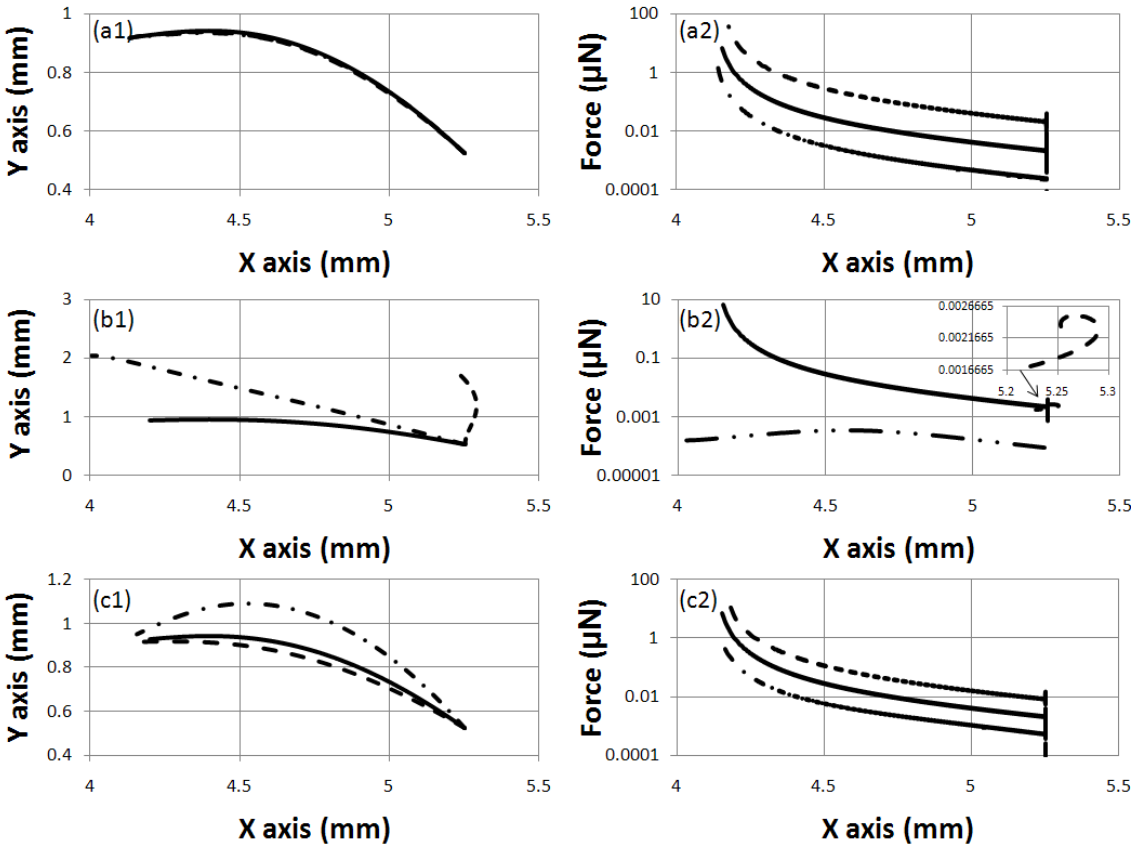

Figure 5.8: A parametric study of the bubble translation under different conditions. The calculated forces are represented by their absolute values. (a1) at 11.5 kPa, the radii of bubble 2 are 6.5 μm (– · –), 13 μm (-), and 26 μm (––); (a2) at 11.5 kPa, the secondary Bjerknes force on bubble 2 with radii of 6.5 μm (– · –), 13 μm (-), and 26 μm (––); (b1) at 11.5 kPa, the radii of bubble 1 are 25 μm (– · –), 50 μm (–), and 100 μm (––); (b2) at 11.5 kPa, the secondary Bjerknes force on bubble 2 with bubble 1 of radii of 25 μm (– · –), 50 μm (–), and 100 μm (––). The secondary force between the 100 μm bubble 1 and 13 μm bubble 2 is shown in the inset; (c1) for a pair of bubbles of radii of 50 μm and 13 μm, the pressure amplitude is 5.25 kPa (– · –), 11.5 kPa (–), and 23 kPa (––); (c2) the secondary Bjerknes force between the bubbles at 5.25 kPa (– · –), 11.5 kPa (–), and 23 kPa (––);

5.4 Conclusion

The collective bubble dynamics near a surface in a weak acoustic standing wave field was shown in this chapter. The bubble translation in a multi-bubble environment was achieved by using a multi-layered resonator which created an uniform one-dimensional acoustic standing wave field in a water layer. The bubble motion was modeled by a pair of modified Keller-Miksis equation and bubble translation equation. The influence of several acoustic and hydrodynamic forces on the bubble

translation was investigated. It was found that the bubble translation near a surface in a multi-bubble environment was mainly controlled by the primary Bjerknes force imposed by the acoustic field, secondary Bjerknes forces introduced by a surface and neighboring bubbles, and buoyancy force from the surrounding liquid. The primary Bjerknes force dominated the bubble translation when the bubble was far away from the surface and was outweighed by the secondary Bjerknes force from the boundary when the bubble was approaching the surface. Moreover, a strong secondary Bjerknes force generated by a neighboring bubble was noticed in the experiment. The bubble-bubble interaction forced nearby bubbles to move on trajectories towards the target bubble instead of the positions that they would have moved to in the absence of the target bubble. It was also seen from a parametric study that increasing the pressure amplitude can enhance the interaction between two bubbles and force bubbles to move at a faster speed. The secondary Bjerknes force between two bubbles can shift from an attractive one when two bubbles oscillate in phase to a repulsive one when their oscillations are out of phase. All of these effects can be decided quantitatively with the presented theory.

Chapter 6

Bubble dynamics near a surface

After their arrivals on a surface, micro-bubbles start to disturb the nearby flow field with their surface oscillations. Previous works mainly focused on the influence of a nearby wall on the oscillation of cavitation bubbles. The interaction between a wall and the oscillation of a moderately oscillating bubble, particularly its non-spherical oscillation modes, is still unclear. Moreover, in a weak acoustic standing wave field, the relationship between a bubble's oscillation mode and the formation of the flow field around it has not yet been fully established. In this chapter, hence, the bubble dynamics near a surface and the characteristics of the flow field are discussed in detail. The change of a bubble's oscillation mode when it approaches a neighboring wall is discussed. The far-field flow motion around an oscillating bubble is explored. The experimental results of bubble oscillation modes and the far-field flow movement are in good agreement with the theoretical predictions.

6.1 Theory

When micro-bubbles arrive on a surface, they can cause flow movement in the vicinity of the boundary. The characteristics of the flow field are directly related to the bubble oscillation modes. Two types of bubble oscillations were reported: spherical and non-spherical modes. Normally, micro-bubbles oscillate symmetrically in the radial direction in the presence of an ultrasound field (Fig. 6.1 a). However,

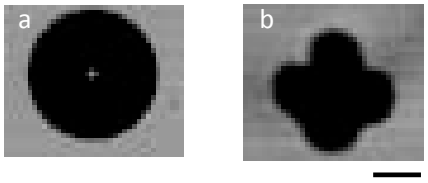

Figure 6.1: A spherical and a non-spherical bubble shapes. (a) a bubble of 70 μm radius oscillated spherically at a driving frequency of 106 kHz. The pressure amplitude was 5 kPa. (b) a bubble of 65 μm radius was driven at 35 kHz with a pressure amplitude of 40 kPa. This bubble shape indicates the bubble was oscillating with a fourth mode. Both bubbles were oscillating in a bulk water medium. The scale bar represents 50 μm.

a bubble can also experience a non-spherical oscillation as seen in Fig. 6.1 b. The conditions to excite the non-spherical oscillation of a bubble are presented in section 6.1.2.

6.1.1 Spherical bubble oscillation near a surface

When a single spherical bubble oscillates at a separation distance d_{wall} from a boundary (Fig. 6.2 a), its radial oscillation can be obtained by considering the real bubble and its imaginary counterpart in Eq.3.24:

$$(1-\frac{\dot{R}}{c})R\ddot{R}+(\frac{3}{2}-\frac{\dot{R}}{2c})\dot{R}^2 = \frac{1}{\rho}(1+\frac{\dot{R}}{c}+\frac{R}{c}\frac{d}{dt})P_{sc}+\frac{\dot{x}^2}{4}-\frac{2}{d_{wall}}(2\dot{R}^2R+R^2\ddot{R}) \tag{6.1}$$

The resonance frequency of a spherical bubble away from a surface is [137]:

$$f_{res} = \frac{1}{2\pi R_0}\sqrt{\frac{3\gamma P_0}{\rho}(1+\frac{2\sigma}{P_0R_0})-\frac{2\sigma}{R_0\rho}} \tag{6.2}$$

It needs to be pointed out that Eq.6.1 is based on the assumption that d_{wall} is larger than the bubble size. For a bubble oscillating on a boundary (Fig. 6.2 b), its spherical oscillation also depends on the properties of the wall. The governing equation for a bubble oscillating on a boundary is given by [149]:

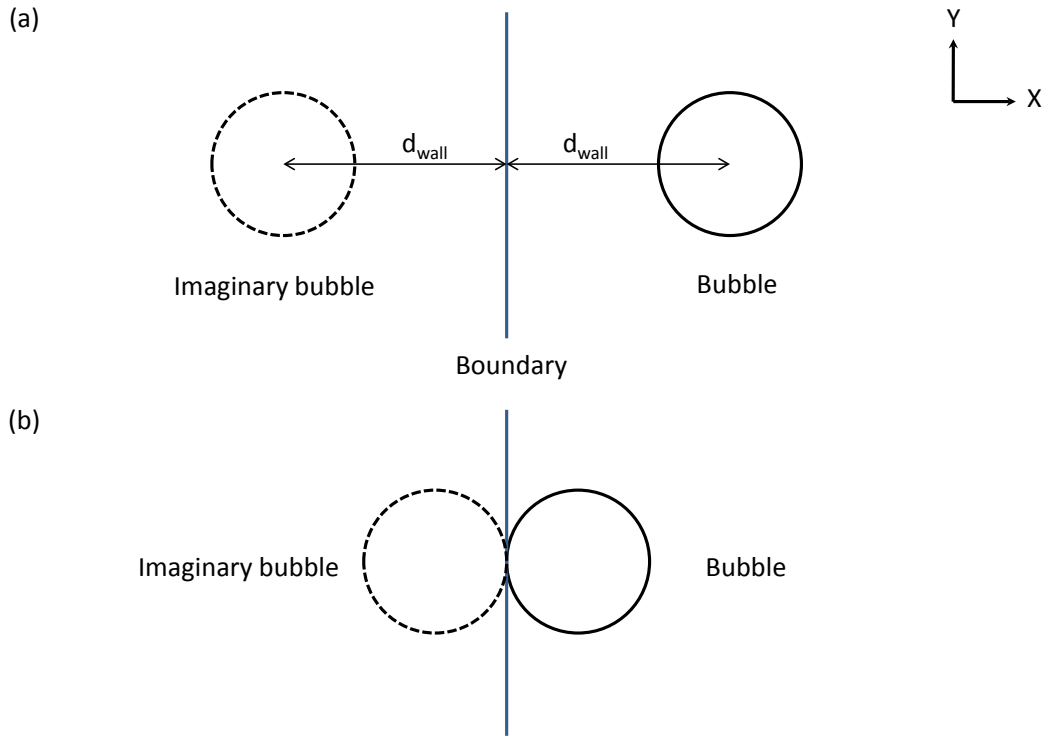

Figure 6.2: The spherical oscillation of a bubble (a) at a separation distance d_{wall} from a boundary, and (b) on a boundary.

$$(1-\frac{\dot{R}}{c})R\ddot{R}+(\frac{3}{2}-\frac{\dot{R}}{2c})\dot{R}^2=\frac{1}{\chi(\rho_{wall},K,G)\rho}(1+\frac{\dot{R}}{c}+\frac{R}{c}\frac{d}{dt})P_{sc} \tag{6.3}$$

where $\chi(\rho_{wall},K,G)$ is a constant that is related to the wall's density (ρ_{wall}), Young's modulus (K), and shear modulus (G). It was reported that $\chi(\rho_{wall},K,G)$ of a rigid wall is larger than unity, while a soft boundary (such as biological tissue or cell membrane) has a $\chi(\rho_{wall},K,G)$ smaller than unity [149]. The influence of the wall on the oscillation of real bubble is included in $\chi(\rho_{wall},K,G)$. The bubble spherical oscillation on a wall is equivalent to its oscillation in a liquid with a changed density $\chi(\rho_{wall},K,G)\rho$ as if the wall does not exist.

Accordingly, the resonance frequency of a spherical bubble oscillating on a wall takes the form of:

$$f_{res}^{wall}=\frac{1}{2\pi R_0}\sqrt{\frac{3\gamma P_0}{\chi(\rho_{wall},K,G)\rho}(1+\frac{2\sigma}{P_0R_0})-\frac{2\sigma}{R_0\rho}} \tag{6.4}$$

To illustrate the influence of $\chi(\rho_{wall},K,G)$ on the spherical bubble oscillation on

a wall, three resonance frequency curves of a bubble oscillating in a bulk medium ($\chi(\rho_{wall}, K, G)$ = 1 [149]), on a glass wall (VWR, UK, $\chi(\rho_{wall}, K, G)$ = 1.1555), and on an OptiCell wall (BioCrystal Ltd, Westerville, USA, $\chi(\rho_{wall}, K, G)$ = 0.62204 [149]) are shown in Fig. 6.3. In the glass wall case, for example, the resonance frequency of a bubble attached to the wall is lower than that of a bubble away from the boundary. Meanwhile, the resonance frequency of a bubble is increased when it is oscillating on an OptiCell wall.

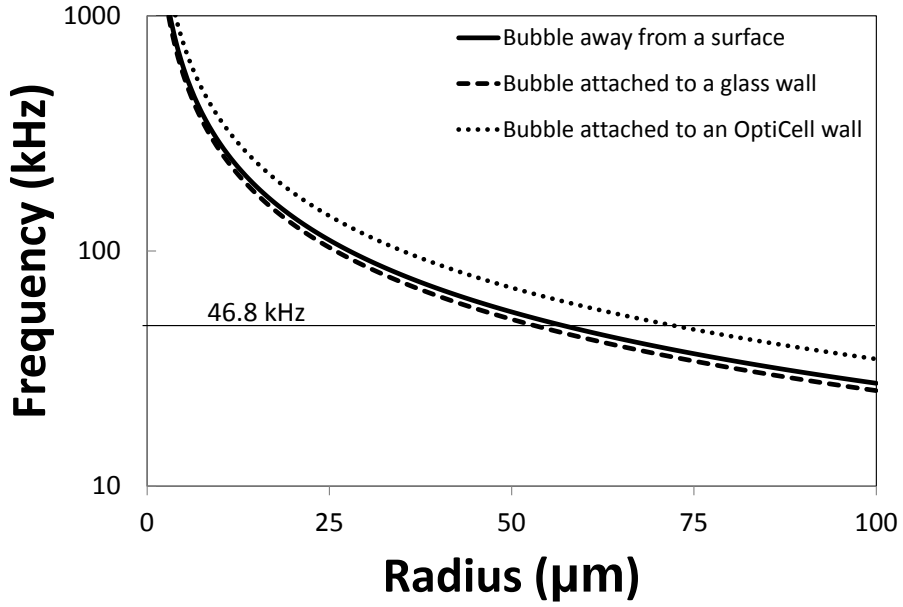

Figure 6.3: Comparison between the resonance frequency of a bubble in a bulk medium ($\chi(\rho_{wall}, K, G)$ = 1), on a glass wall ($\chi(\rho_{wall}, K, G)$ = 1.1555), and on an OptiCell wall ($\chi(\rho_{wall}, K, G)$ = 0.62204). The bubble radii range from 1 to 100 μm.

6.1.2 Non-spherical bubble oscillation near a surface

In addition to the spherical pulsation, a bubble can also oscillate non-spherically in an acoustic field. The shape instability of a bubble was first analyzed by Plesset by introducing non-spherical component in the derivation of bubble oscillation equation [77]. Based on Plessets work, Hilgenfeldt et al proposed a modified equation to calculate the amplitude of non-spherical oscillation [81]. Hilgenfeldts model takes the local viscosity near the bubble surface into account, and has been widely used for explaining sonoluminescing air bubbles [82].

To excite the non-spherical oscillation of a bubble, a small perturbation is introduced on the bubble surface $R(\theta,t) = R(t) + a_n(t)Y_n(\theta)$, where $Y_n(\theta)$ is the spherical harmonic of order n with amplitude of $a_n(t)$. Neglecting the coupling between different modes, the distortion amplitude $a_n(t)$ follows the form of [77, 78, 81]:

$$\ddot{a}_n(t) + B_n(t)\dot{a}_n(t) - A_n(t)a_n(t) = 0 \tag{6.5}$$

Taking the boundary layer approximation and viscous effects into account, $A_n(t)$ and $B_n(t)$ are given by [81]

$$A_n(t) = (n-1)\frac{\ddot{R}}{R} - \frac{\beta_n\sigma}{\rho R^3} - \frac{2\eta\dot{R}}{R^3}[(n-1)(n+2) + 2n(n+2)(n-1)\frac{\delta}{R}] \tag{6.6}$$

$$B_n(t) = \frac{3\dot{R}}{R} + \frac{2\eta}{R^2}[(n+2)(2n+1) - 2n(n+2)^2\frac{\delta}{R}] \tag{6.7}$$

where $\delta = min(\sqrt{\frac{\eta}{\omega}}, \frac{R}{2n})$ and $\beta_n = (n-1)(n+1)(n+2)$.

$a_n(t)$ can be calculated by solving Eq.6.5 - 6.7 with Eq.6.1 for a non-spherical bubble oscillating at a separation distance d_{wall} from a boundary, and with Eq.6.3 for a bubble oscillating on a wall.

Unlike the spherical oscillation which is excited spontaneously in the presence of ultrasound, the non-spherical oscillation can be triggered when the external pressure amplitude exceeds a threshold for a bubble of certain size. The pressure threshold is known as [150]:

$$p_{threshold} = \rho R_0^2 \sqrt{h \frac{(s-1)^2 + 4p}{[-\frac{3}{2}s + 2p + 2(l+\frac{1}{2})]^2 + q^2}} \tag{6.8}$$

$$\begin{aligned} h &= (\omega_0^2 - \omega^2)^2 + (2\beta_{tot}\omega)^2 \\ s &= \frac{4(n-1)(n+1)(n+2)\sigma}{\rho\omega^2 R_0^3} \\ p &= [\frac{2(n+2)(2n+1)\eta}{\rho\omega R_0^2}]^2 \\ q &= \frac{6(n+2)\eta}{\rho\omega R_0^2} \end{aligned}$$

where β_{tot} is the damping factor [151].

The resonance frequency of a non-spherical bubble is [136]:

$$f_n = \frac{1}{2\pi}\sqrt{(n-1)(n+1)(n+2)\frac{\sigma}{\rho R_0^3}},\ n \geq 2 \tag{6.9}$$

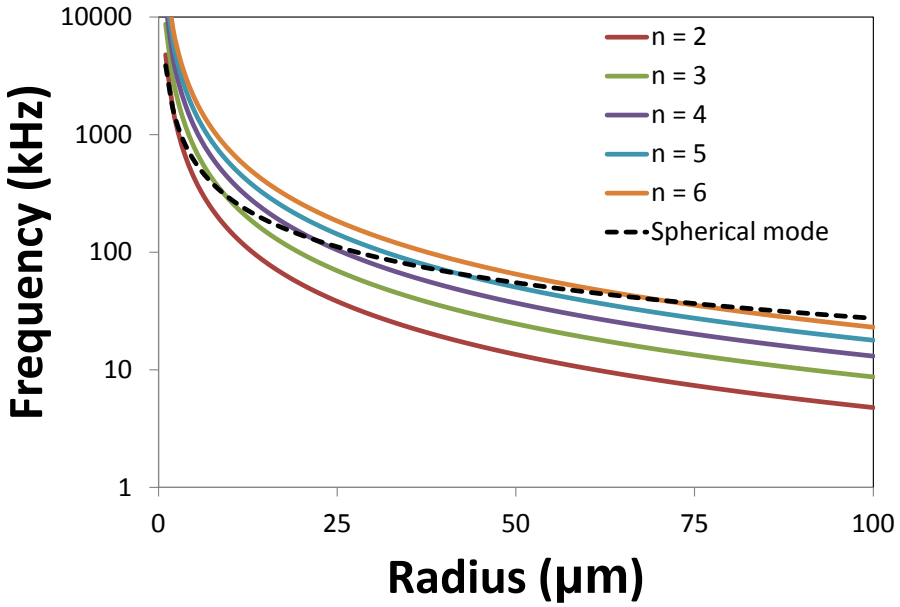

Figure 6.4: The resonance frequencies of non-spherical bubbles with radii ranging from 1 to 100 μm (Eq.6.9). The mode numbers are selected from 2 to 6. The resonance frequency of a spherical bubble (dashed line) is also shown for comparison.

Fig. 6.4 shows the resonance frequency of non-spherical bubbles with radii ranging

from 1 to 100 μm. The mode numbers are selected from $n = 2 - 6$. The resonance frequency of a certain mode decreases with an increase of bubble radius. For a bubble of given size, its non-spherical resonance frequency grows with an increase of mode number. The resonance frequency of a bubble away from a wall is also shown in Fig. 6.4 for comparison.

6.1.3 Microstreaming

It is well-known that either the spherical or non-spherical oscillation of a bubble can accelerate the flow field near the bubble surface [116]. The rectified component of the flow motion is known as microstreaming. Since the microstreaming is directly related to the bubble induced hydrodynamic forces on a particle, a brief review of the microstreaming is given here.

In an incompressible flow, the liquid velocity u is governed by the Navier–Stokes equation [136]:

$$\frac{\partial u}{\partial t} + u\nabla u = \frac{1}{\rho}\left[-\nabla P + \eta\nabla^2 u + F\right] \tag{6.10}$$

where P is the pressure, and F is the sum of external forces.

Taking the curl of the Navier–Stokes equation on both sides eliminates the pressure component. Then, the liquid velocity u can also be replaced by the Stokes streaming function ψ which is related to the radial and tangential components of the liquid velocity [136]:

$$u_r = \frac{1}{r^2 sin\theta}\frac{\partial \psi}{\partial \theta}, u_\theta = -\frac{1}{r sin\theta}\frac{\partial \psi}{\partial r} \tag{6.11}$$

It needs to be noted here that ψ is the Eulerian streaming function. The real flow motion needs to be represented by the Lagrangian streaming function Ψ which is the sum of the Eulerian streaming function and the Stokes drift ψ_s [108]

$$\Psi = \bar{\psi} + \psi_s$$

$$\psi_s = \frac{1}{r^2}\overline{\int \frac{\partial \psi}{\partial r} dt \frac{\partial \psi}{\partial \nu}} \tag{6.12}$$

Usually, the flow motion can be experimentally visualized by adding tracer particles in the liquid, known as Particle Image Velocimetry (PIV) [117]. From a physical point of view, the Lagrangian streaming function Ψ represents the trajectory of these passive tracer particles in the flow field. Thus, Ψ provides a direct way to estimate the flow behavior near a bubble, and can be used to predict the bubble induced hydrodynamic forces. More details of the microstreaming are provided in the Appendix.

Microstreaming due to spherical oscillation

For a spherically oscillating bubble with a lateral translation, the lowest order form of the Lagrangian microstreaming in a bulk medium is [108]:

$$\bar{\Psi}_{11} = \frac{\epsilon^2}{4} R_0^3 \omega sin\phi (-2\frac{r}{R_0} + \frac{R_0}{r} + \frac{R_0^4}{r^4}) sin^2\theta \tag{6.13}$$

where ϵ is the oscillation amplitude. ϕ is the phase shift between the spherical and translational oscillations.

The microstreaming that is caused by the radial and lateral oscillations of a spherical bubble is shown in Fig. 6.5 a. Since the purpose of Fig. 6.5 a is to solely illustrate the microstreaming around a bubble, the parameters except r and θ are all set to unity. For example, $\frac{\epsilon^2}{4} R_0^3 \omega sin\phi = 1$ and $R_0 = 1$ are assumed here. Similar settings are used for Fig. 6.5 (b - d).

In many real life applications, a bubble normally oscillates on a surface. Thus, the bulk medium streaming function needs to be expanded to include the boundary effects. Suppose the surface is rigid, the influence from the boundary on the microstreaming can be treated by adding imaginary singularities on the other side of

the wall . The sum of the original streaming function and the imaginary streaming functions creates a new streaming function $\bar{\Psi}_{11w}$ which fulfills the boundary condition (Fig. 6.5 b) [120].

$$\bar{\Psi}_{11w} = -3\epsilon^2 R_0^4 \omega sin\phi \frac{1}{r} cos^2\theta sin^2\theta \tag{6.14}$$

The flow velocity can then be calculated by substituting Eq.6.14 into Eq.6.11

$$u_{r11w} = \frac{6\epsilon^2 R_0^4 \omega sin\phi}{r^3}[2cos^3\theta - cos\theta]$$

$$u_{\theta 11w} = -\frac{3\epsilon^2 R_0^4 \omega sin\phi}{r^3} cos^2\theta sin\theta \tag{6.15}$$

Microstreaming due to non-spherical oscillation

For a non-spherically oscillating bubble, the lowest order Lagrangian streaming function is found in the literature as (Fig. 6.5 c) [152]:

$$\bar{\Psi}_{11}^n = \frac{\omega\epsilon_{1n}^2 R_0}{2\pi} \frac{2n+1}{4\pi} \frac{(n+2)(n+3)}{2(n+1)(4n+3)} [-(\frac{R_0}{r})^{(2n-1)} + (\frac{R_0}{r})^{(2n+1)}] cos(2n+1)\theta \tag{6.16}$$

where ϵ_{1n} is the amplitude of the nth mode.

For a non-spherical bubble oscillating near a surface, the streaming function also needs to be expanded to include the influence from the wall. By introducing imaginary singularities on the other side of the wall, the new Lagrangian streaming function $\bar{\Psi}_{11w}^n$ takes the form of (Fig. 6.5 d):

$$\bar{\Psi}_{11w}^n = \frac{\omega\epsilon_{1n}^2 R_0^{2n}}{2\pi} \frac{2n+1}{4\pi} \frac{(n+2)(n+3)}{2(n+1)(4n+3)} (4n^2+2n-2) \frac{1}{r^{2n-1}} cos(2n+1)\theta sin^2\theta \tag{6.17}$$

Similar to the spherical case, the flow velocity can be obtained by:

$$u^n_{r11w} = \frac{\omega\epsilon_{1n}^2 R_0^{2n}}{2\pi}\frac{2n+1}{4\pi}\frac{(n+2)(n+3)}{2(n+1)(4n+3)}(4n^2+2n-2) \\ \frac{1}{r^{2n+1}}[2cos(2n+1)\theta cos\theta - (2n+1)sin(2n+1)\theta sin\theta] \tag{6.18}$$

$$u^n_{\theta 11w} = \frac{\omega\epsilon_{1n}^2 R_0^{2n}}{2\pi}\frac{2n+1}{4\pi}\frac{(2n-1)(n+2)(n+3)}{2(n+1)(4n+3)}(4n^2+2n-2)\frac{1}{r^{2n+1}}cos(2n+1)\theta sin\theta \tag{6.19}$$

It can be seen from Fig. 6.5 that the formation of microstreaming depends on the bubble oscillation modes. For example, the microstreaming that is generated by a non-spherical oscillation near a wall is confined within the near field from the bubble surface. This is because $\bar{\Psi}^n_{11w}$ decays at an order of $r^{-(2n-1)}$, while its spherical counterpart decreases at a much slower speed ($\sim r^{-1}$).

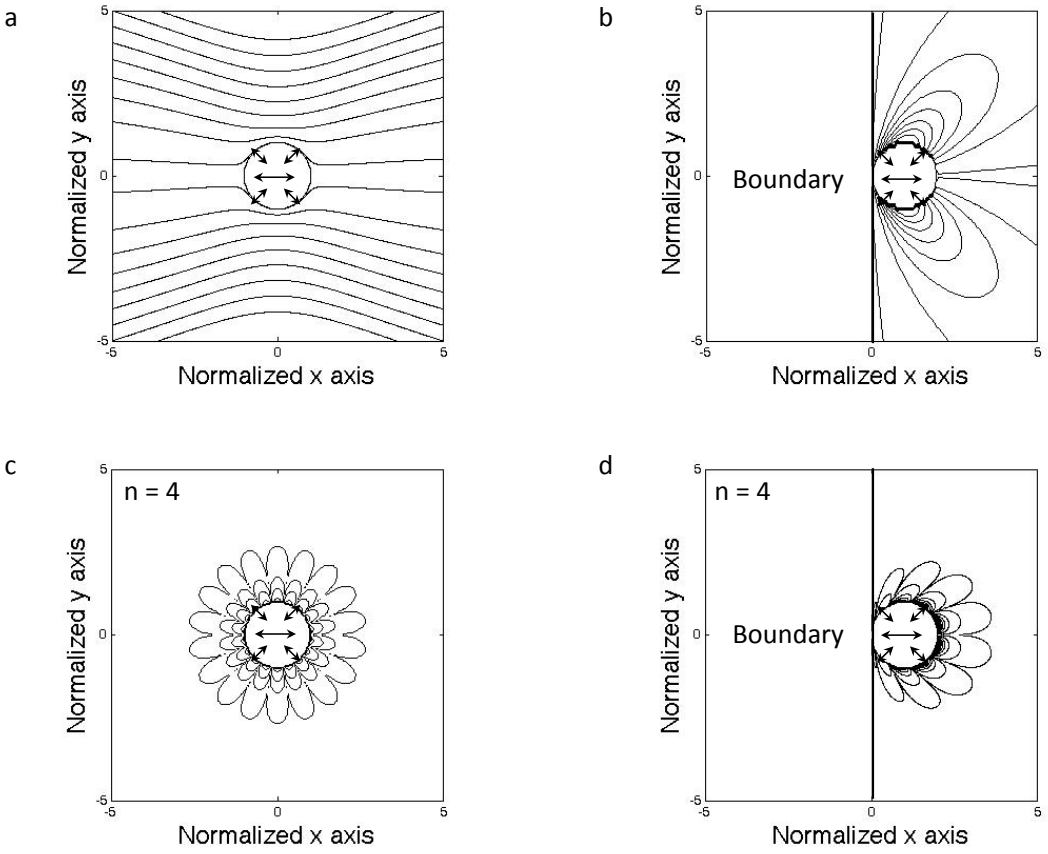

Figure 6.5: The flow motion around an oscillating bubble is represented by the streaming lines. Four types of streaming lines (a) a spherical bubble oscillates in the radial and lateral directions simultaneously. (b) a spherical bubble oscillates on a wall. (c) a non-spherical bubble oscillates in a bulk medium with lateral oscillation. The mode number $n = 4$. (d) a non-spherical bubble oscillates on a wall with the lateral oscillation. The mode number $n = 4$.

6.2 Experimental configuration

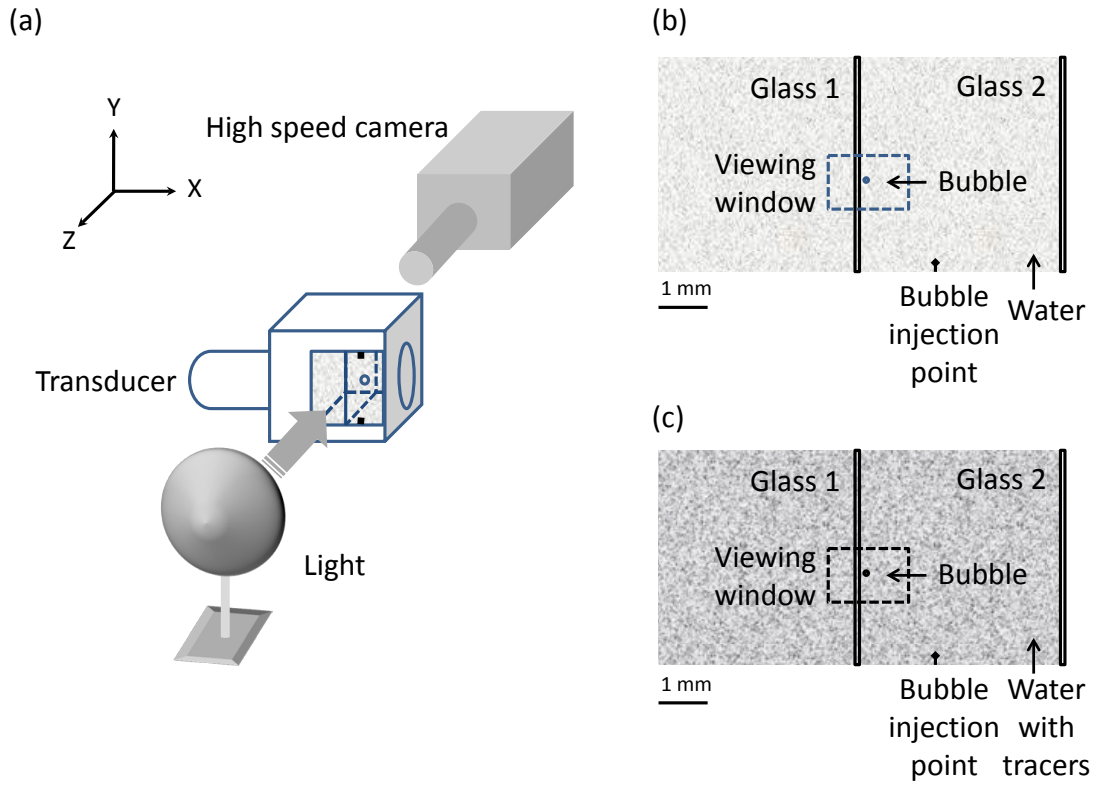

Figure 6.6: A schematic diagram of the test rig for studying the bubble dynamics and microstreaming. (a) the high speed camera system. (b) setup for observing bubble oscillation modes near a surface. (c) setup for observing the microstreaming around a bubble. The dimensions of the setup are the same as presented in chapter 4.

To visualize the bubble behavior near a surface, an experimental setup was designed as shown in Fig. 6.6. The experiments were carried out in two steps: the first step is to zoom in on an area of 1.2 mm by 0.3 mm to observe the oscillations of bubbles when they are approaching glass 1; the second step aims to visualize the microstreaming around an oscillating bubble near the boundary. It needs to be pointed out that the frame rate used in the previous experiments (100k frames/s in chapter 4), is not fast enough to capture the whole process of bubble oscillation because only two frames can be recorded over one oscillation cycle at this frame rate (driving frequency is 46.8 kHz). Thus, a higher frame rate, 525 kframes/s, is used for the following experiments.

The observation of microstreaming was achieved using the Particle Image Velocime-

try (PIV). Tracer particles (Melamine resin micro particle, Sigma-Aldrich, UK) are added into the water chamber in order to reveal the microstreaming. The trajectories of the tracer particles are recorded by the high speed camera system and are analyzed by a particle tracer algorithm written in Matlab (Mathworks, USA).

6.3 Results

6.3.1 Spherical bubble oscillation near a surface

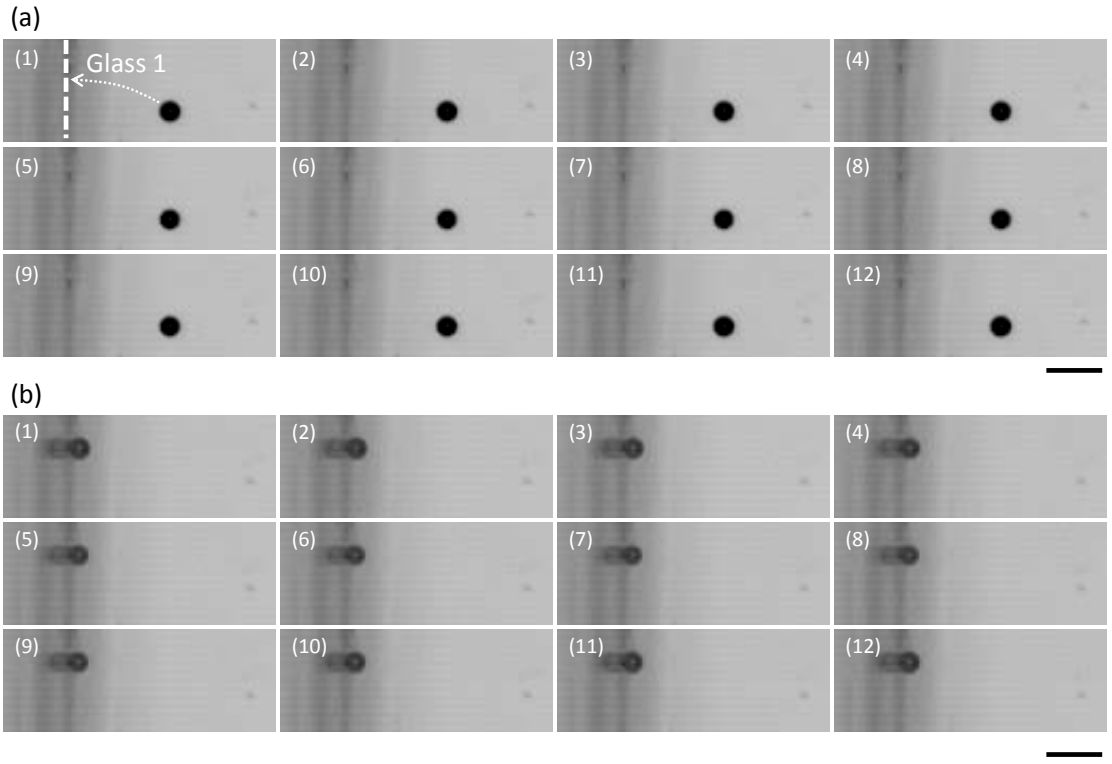

Figure 6.7: Selected frames from a video of bubble oscillation near a surface at 11.5 kPa. The bubble radius is 43 μm. (a) the bubble oscillates with a spherical mode when approaching glass 1. (b) the bubble keeps its spherical shape when sitting on the glass surface. Viewing from top to bottom and left to right. The time interval between each frame is 1.9 μs. The scale bar represents 200 μm.

At 11.5 kPa, a bubble of 43 μm radius translates towards glass 1 as shown in Fig. 6.7 (a). The twelve consecutive frames in Fig. 6.7 (a) present a whole cycle of bubble oscillation. The bubble maintains a spherical shape at this pressure amplitude and its radius periodically varies between 41 μm and 45 μm. The separation distance

between the bubble and the boundary is 0.3 mm. After 11 ms, the bubble arrives onto the surface and still keeps its spherical shape (Fig. 6.7 (b)). The maximum radius, however, increases from 45 μm to 50 μm, while the minimum radius is lowered from 41 μm to 39 μm.

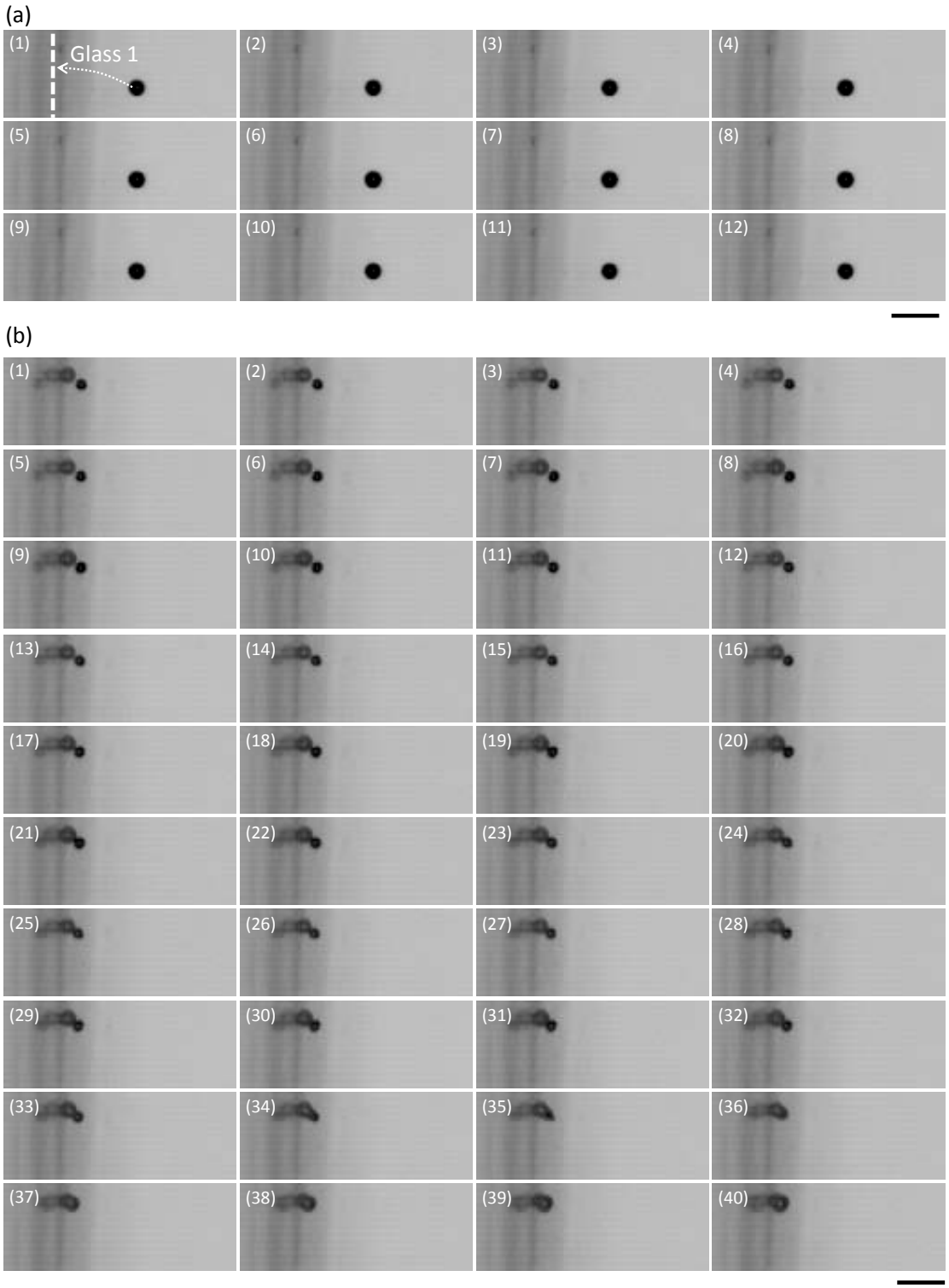

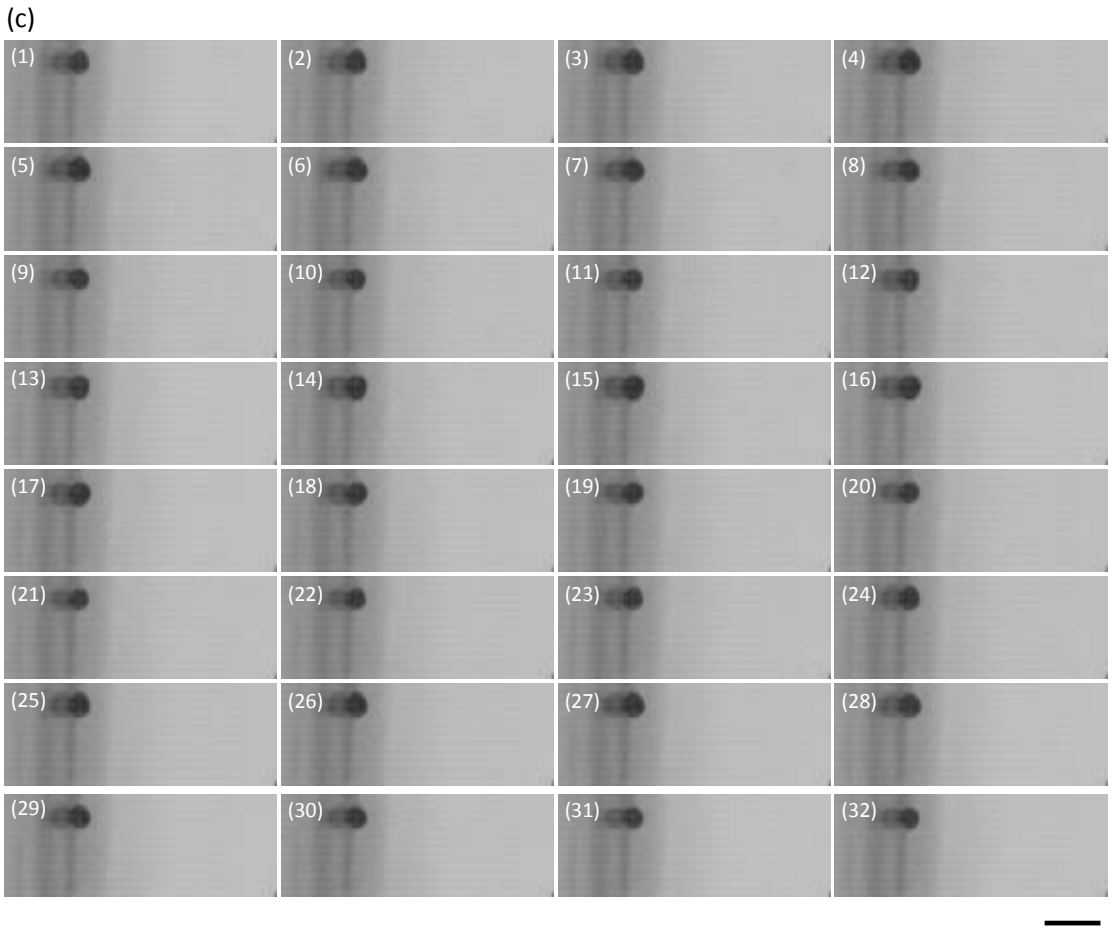

Figure 6.8: Selected frames from a video of bubble oscillation near a surface at 11.5 kPa. The bubble radius is 41 μm. (a) the bubble oscillates with a spherical mode when it is approaching glass 1. (b) a new bubble approaches the target one on the glass surface. (c) a newly formed bubble oscillates with a non-spherical shape. Viewing from top to bottom and left to right. The time interval between each frame is 1.9 μs. The scale bar represents 200 μm.

At the same pressure amplitude, for a similar size bubble, its spherical oscillation can be adjusted to a non-spherical one in the presence of a nearby bubble. In Fig. 6.8 (a), a bubble (radius of 41 μm) oscillates spherically during its translation to glass 1. The spherical oscillation is disturbed by the arrival of another nearby bubble (radius of 28 μm) at 97 ms. The coalescence of these two bubbles is clearly seen in Fig. 6.8 (b). The newly formed bubble then starts to oscillate with a non-spherical mode on the surface as shown in Fig. 6.8 (c).

At a higher pressure amplitude, 20 kPa, a bubble of 43 μm radius oscillates with a spherical shape where the bubble radius varies between 38 μm and 48 μm (Fig. 6.9

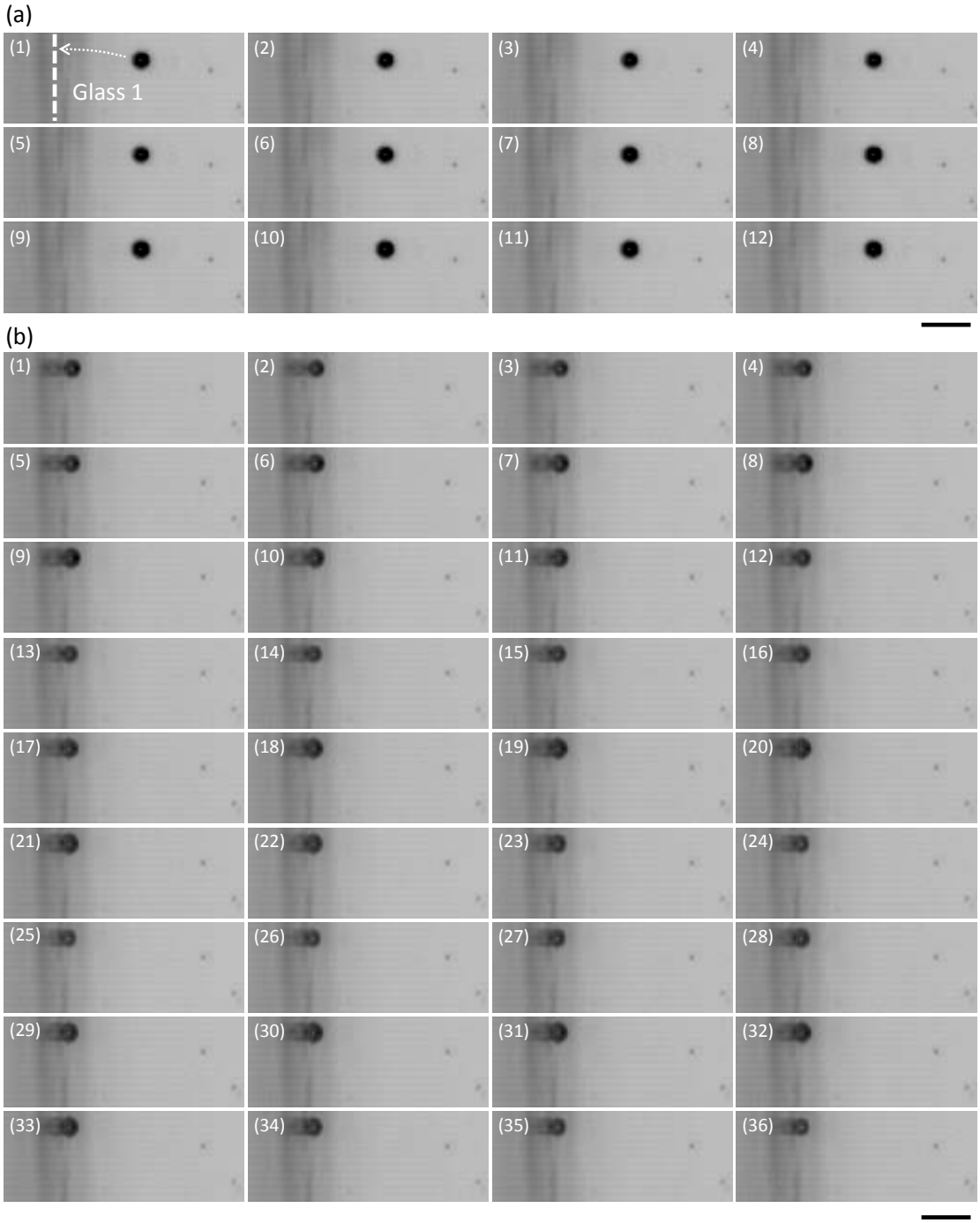
(a)
(1)
Glass 1
(2)
(3)
(4)
(5)
(6)
(7)
(8)
(9)
(10)
(11)
(12)
(b)
(1)
(2)
(3)
(4)
(5)
(6)
(7)
(8)
(9)
(10)
(11)
(12)
(13)
(14)
(15)
(16)
(17)
(18)
(19)
(20)
(21)
(22)
(23)
(24)
(25)
(26)
(27)
(28)
(29)
(30)
(31)
(32)
(33)
(34)
(35)
(36)

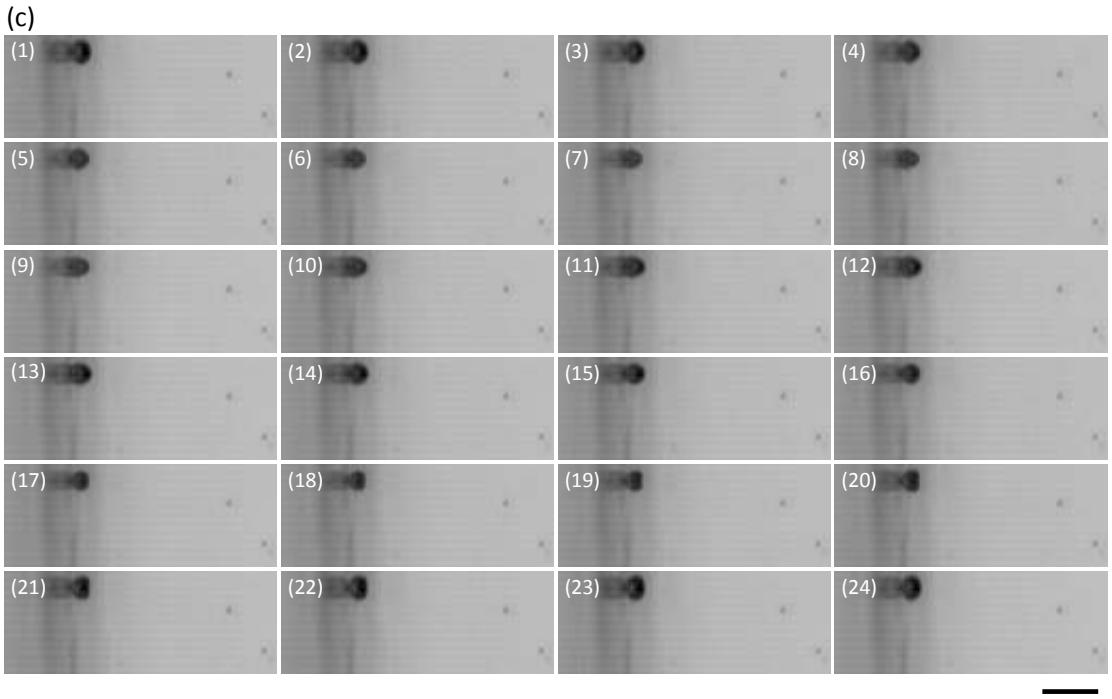

Figure 6.9: Selected frames from a video of bubble oscillation near a surface at 20 kPa. The bubble radius is 43 μm. (a) the bubble oscillates spherically when it is approaching glass 1. (b) the bubble arrives on the surface (c) the bubble oscillates with a non-spherical shape. Viewing from top to bottom and left to right. The time interval between each frame is 1.9 μs. The scale bar represents 200 μm.

(a)). When the bubble arrives onto the surface in Fig. 6.9 (b), it starts to lose its symmetric shape and gradually shifts to a non-spherical oscillation mode. The non-spherical shape is finally formed in Fig. 6.9 (c). The bubble starts to stretch in the horizontal direction where it reaches a maximum extension and then shrinks. The compression of surface shape in the horizontal direction results in a growth of bubble in the vertical direction. When the bubble surface grows to the maximum in the vertical direction, its shape falls back to the original state and then repeats the whole process again.

The influence of the wall on the oscillation of a bubble translating with a spherical shape is more substantial at 28.7 kPa. Initially, a spherical bubble translates in the sound field as seen in Fig. 6.10 (a). After 1.6 ms, the bubble approaches glass 1 at a faster speed. Immediately, the bubble starts to change its shape from spherical to elliptical even without touching the glass surface. The shape change becomes more dramatic after the arrival of the bubble on the glass surface. The elongation of the

bubble shape in the vertical direction eventually leads to a split of the bubble into two parts which then merge back together to form a new bubble. Two subsequent coalescence of the target bubble with two other neighboring bubbles are also shown in Fig. 6.10 (c) and (d) respectively. The newly formed bubble oscillates with a much more complicated mode and completely loses its spherical shape.

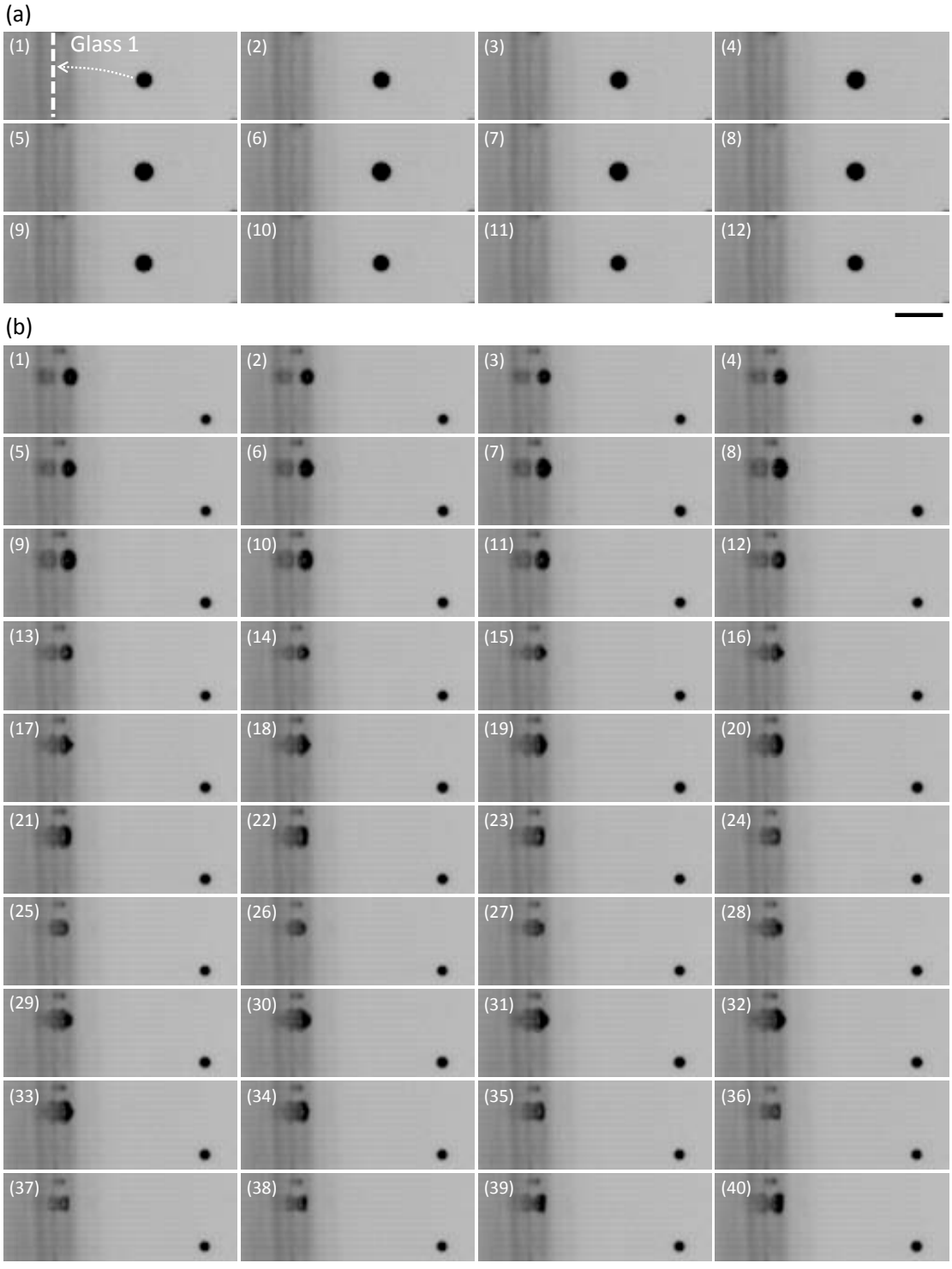

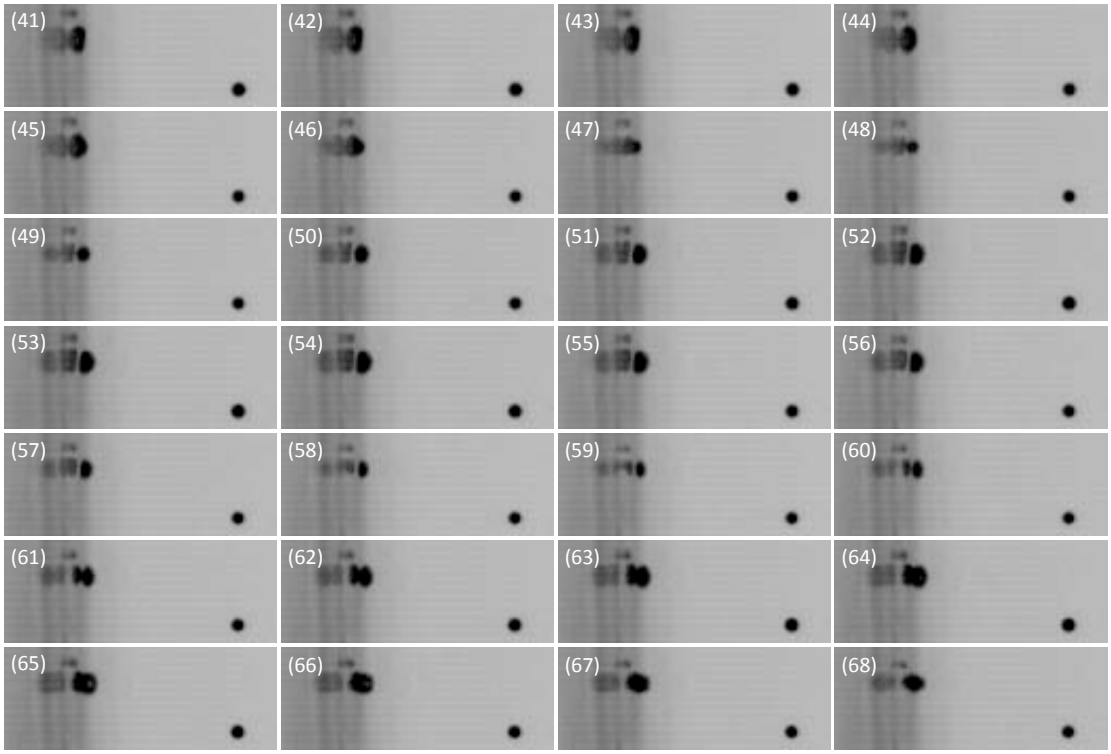
(41)
(42)
(43)
(44)
(45)
(46)
(47)
(48)
(49)
(50)
(51)
(52)
(53)
(54)
(55)
(56)
(57)
(58)
(59)
(60)
(61)
(62)
(63)
(64)
(65)
(66)
(67)
(68)

(c)

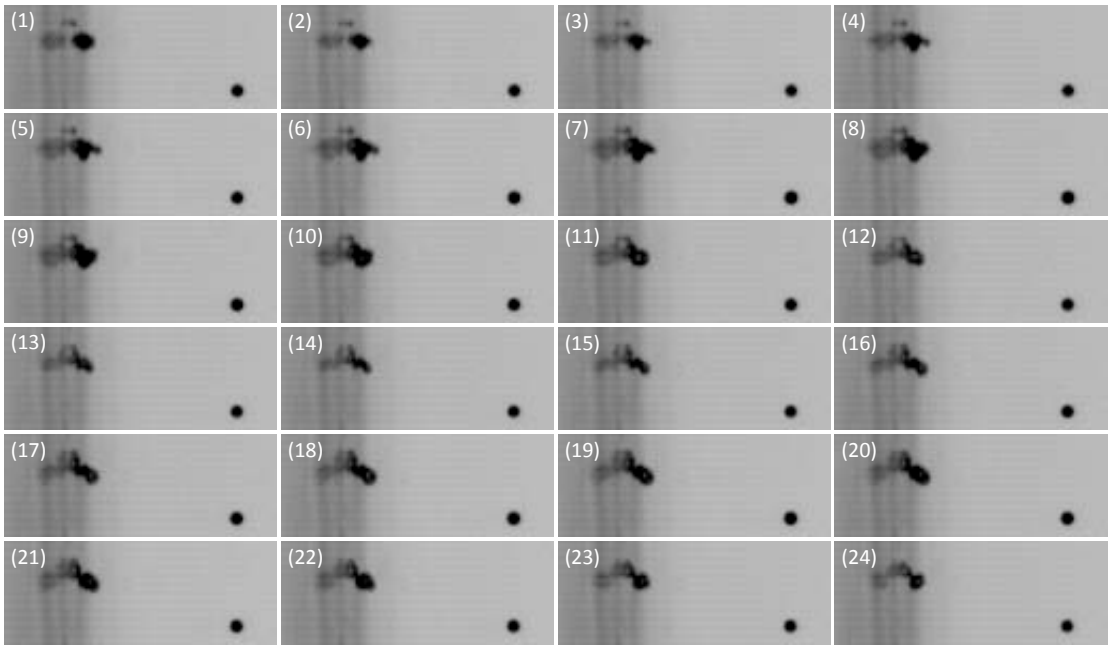
(1)
(2)
(3)
(4)
(5)
(6)
(7)
(8)
(9)
(10)
(11)
(12)
(13)
(14)
(15)
(16)
(17)
(18)
(19)
(20)
(21)
(22)
(23)
(24)

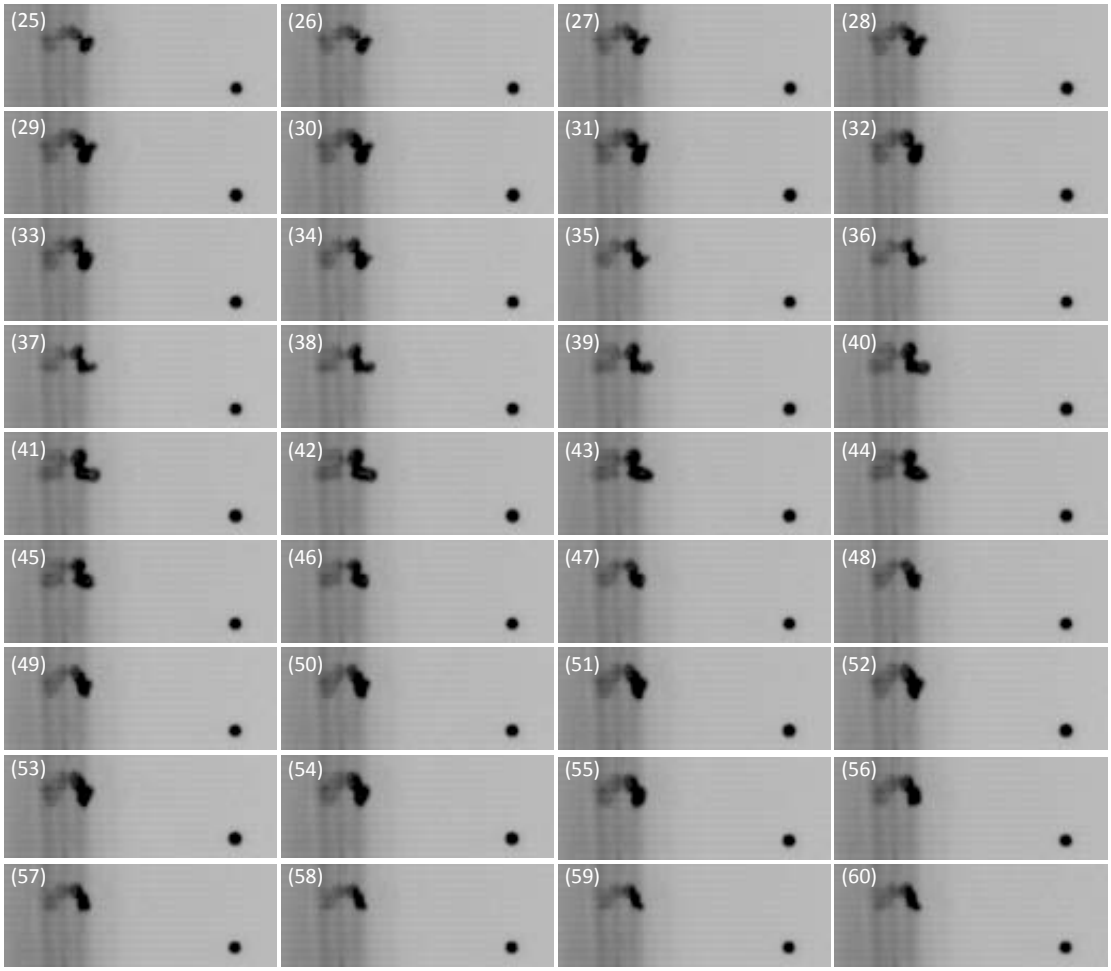
(25)
(26)
(27)
(28)
(29)
(30)
(31)
(32)
(33)
(34)
(35)
(36)
(37)
(38)
(39)
(40)
(41)
(42)
(43)
(44)
(45)
(46)
(47)
(48)
(49)
(50)
(51)
(52)
(53)
(54)
(55)
(56)
(57)
(58)
(59)
(60)

(d)

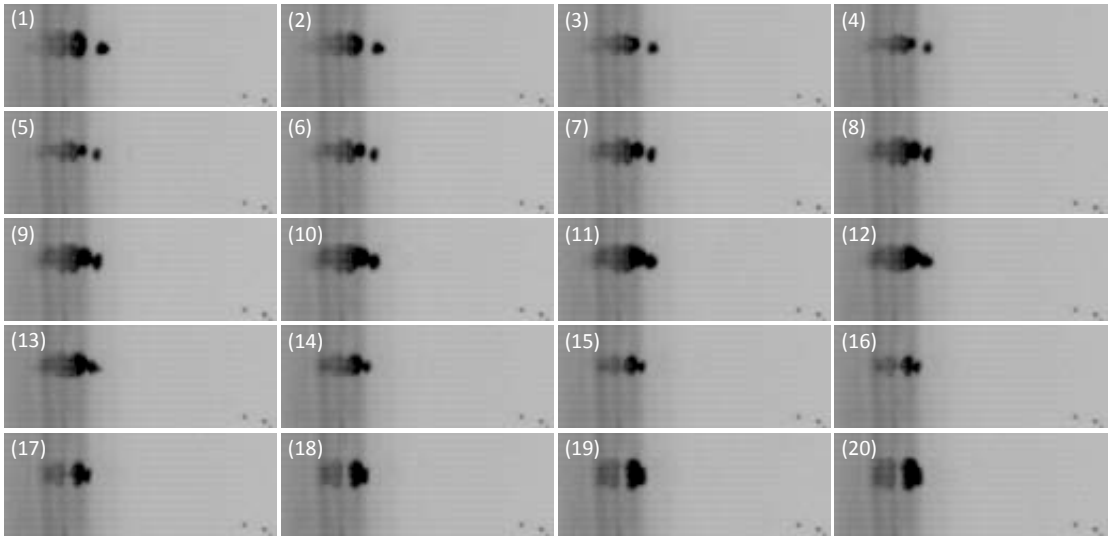
(1)
(2)
(3)
(4)
(5)
(6)
(7)
(8)
(9)
(10)
(11)
(12)
(13)
(14)
(15)
(16)
(17)
(18)
(19)
(20)

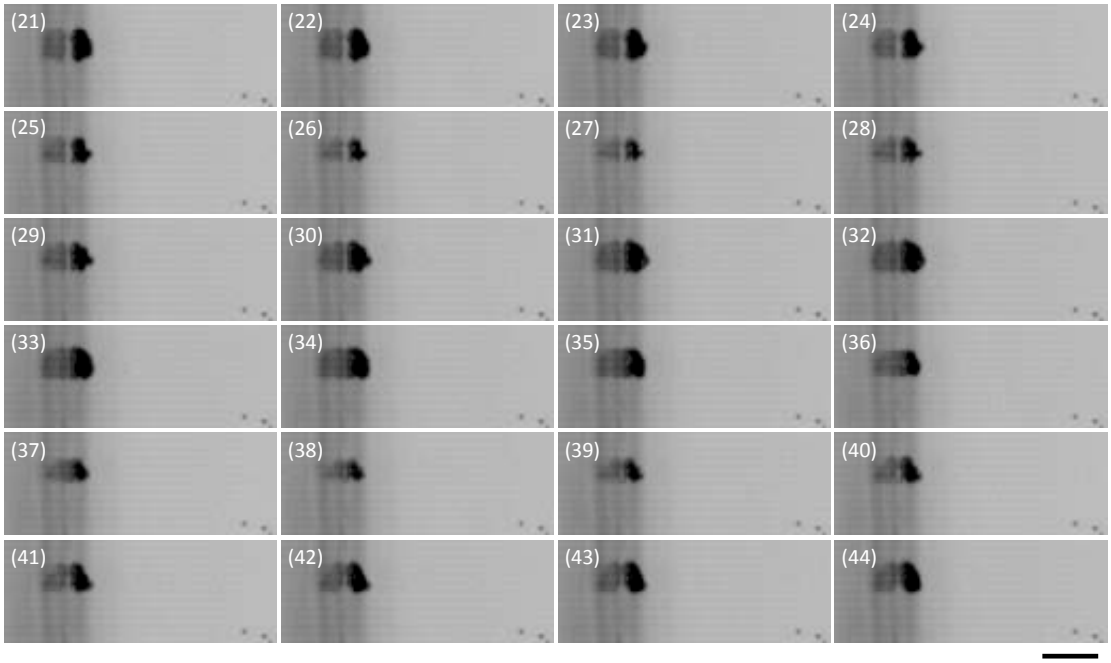

Figure 6.10: Selected frames from a video of bubble oscillation near a surface at 28.7 kPa. The bubble radius is 43 μm. (a) the bubble oscillates with a spherical shape when it is approaching glass 1. (b) the bubble arrives on the surface (c) coalescence of the bubble with a nearby bubble. (d) a second coalescence of two bubbles on the surface. Viewing from top to bottom and left to right. The time interval between each frame is 1.9 μs. The scale bar represents 200 μm.

6.3.2 Non-spherical bubble oscillation near a surface

On the other hand, a bubble can translate with a non-spherical shape when its size exceeds a certain threshold. At 11.5 kPa, for example, a bubble of 54 μm radius oscillates non-spherically when it moves towards glass 1 (Fig. 6.11 (a)). The triangle shape indicates that the bubble pulsates with the third mode during its translation. This triangle shape shifts back to a spherical one after the bubble's arrival on the glass surface in Fig. 6.11 (b). The temporary spherical shape, however, starts to grow back to a non-spherical one after a few acoustic cycles. The asymmetric surface shape is finally formed in Fig. 6.11 (c).

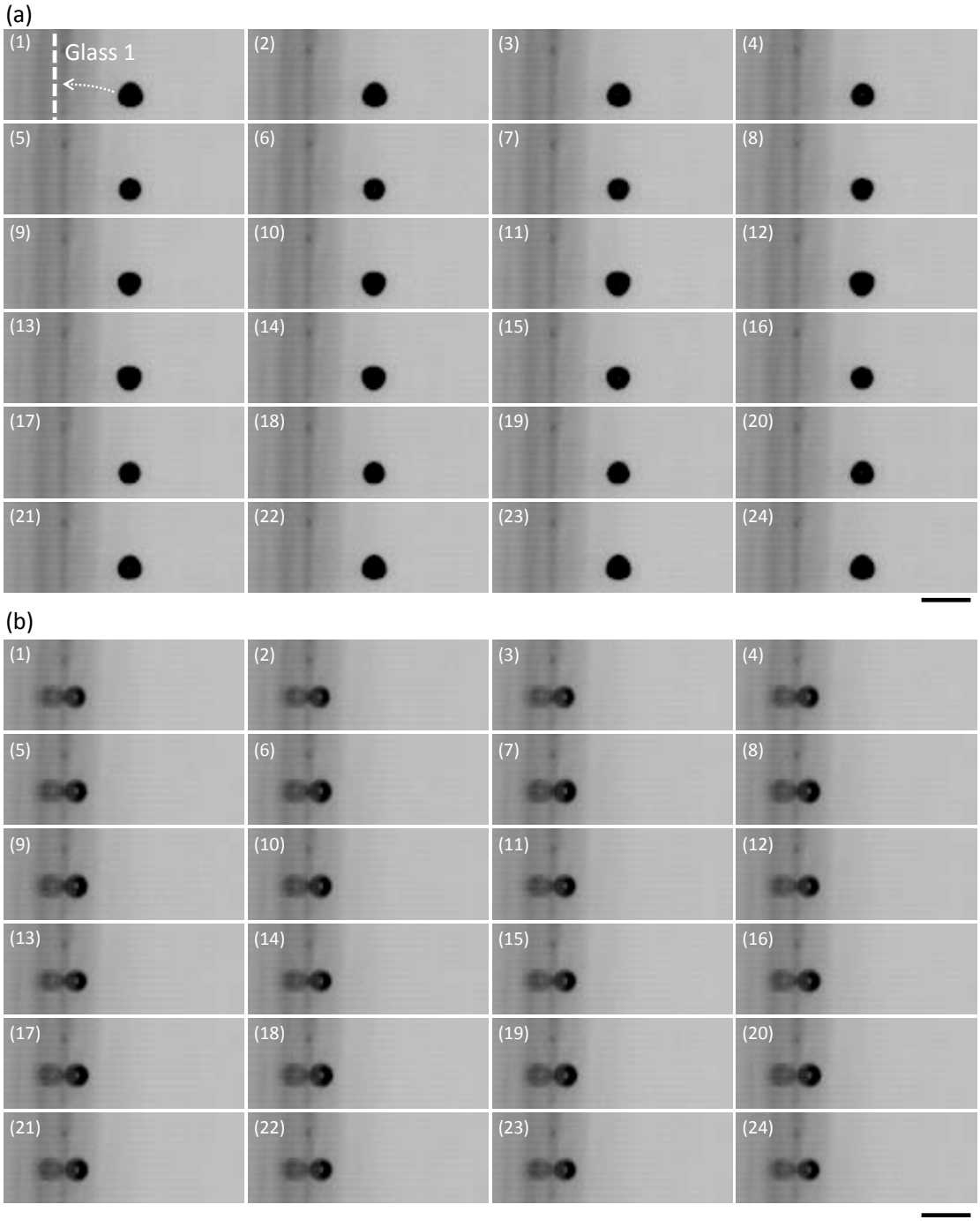
(a)
(1)
Glass 1
(2)
(3)
(4)
(5)
(6)
(7)
(8)
(9)
(10)
(11)
(12)
(13)
(14)
(15)
(16)
(17)
(18)
(19)
(20)
(21)
(22)
(23)
(24)
(b)
(1)
(2)
(3)
(4)
(5)
(6)
(7)
(8)
(9)
(10)
(11)
(12)
(13)
(14)
(15)
(16)
(17)
(18)
(19)
(20)
(21)
(22)
(23)
(24)

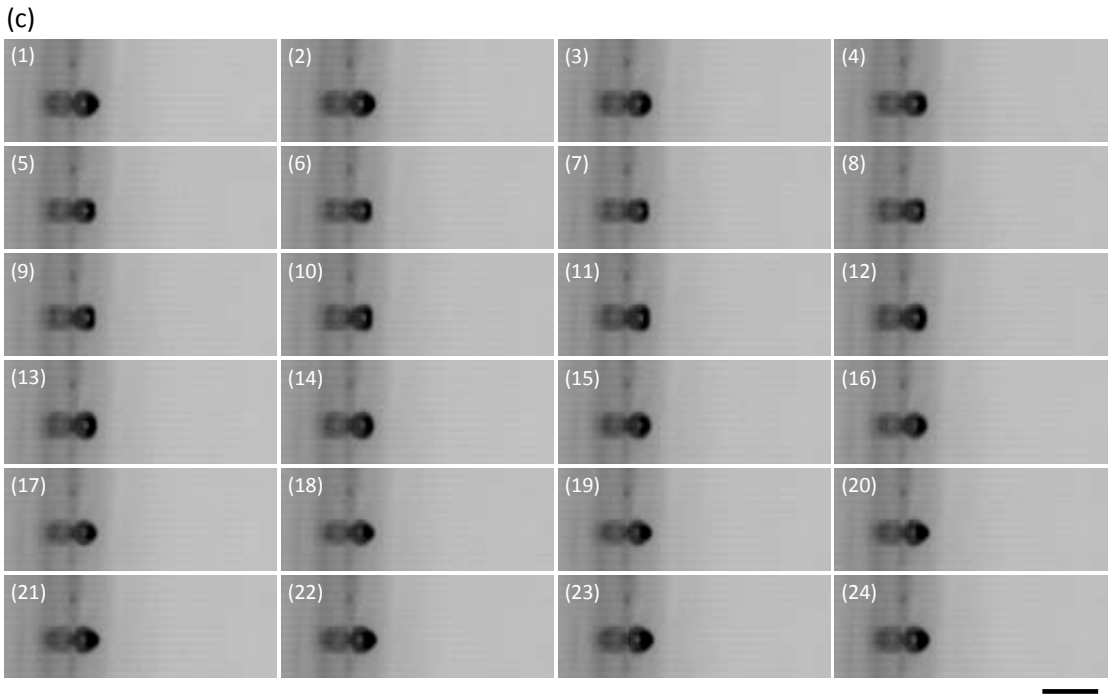

Figure 6.11: Selected frames from a video of bubble oscillation near a surface at 11.5 kPa. The bubble radius is 54 μm. (a) the bubble oscillates with a non-spherical shape when it is approaching glass 1. (b) the bubble shape returns to a spherical one after its arrival on the glass surface. (c) the bubble oscillates with a non-spherical shape. Viewing from top to bottom and left to right. The time interval between each frame is 1.9 μs. The scale bar represents 200 μm.

At 20 kPa, a bubble of 52 μm radius also shows a non-spherical oscillation behavior when it travels towards glass 1. A similar triangle shape is seen in Fig. 6.12 (a). Unlike the low pressure case, the bubble surface immediately changes to a more complicated shape after its arrival on the glass surface. This non-spherical shape keeps evolving as seen in Fig. 6.12 (b - c). The identification of the non-spherical mode, however, is difficult here owing to the limited frame resolution of the frames.

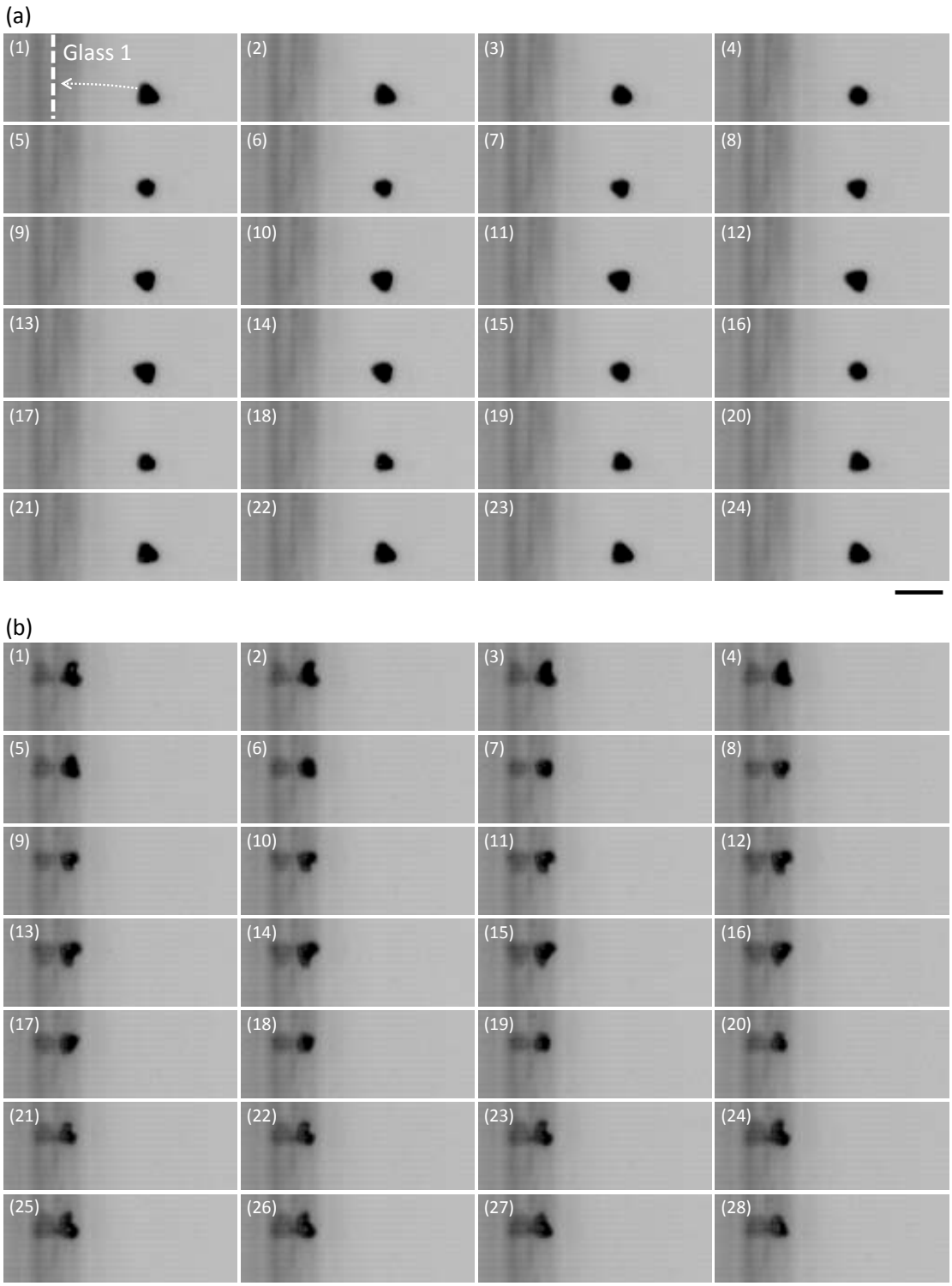
(a)
(1)
Glass 1
(2)
(3)
(4)
(5)
(6)
(7)
(8)
(9)
(10)
(11)
(12)
(13)
(14)
(15)
(16)
(17)
(18)
(19)
(20)
(21)
(22)
(23)
(24)
(b)
(1)
(2)
(3)
(4)
(5)
(6)
(7)
(8)
(9)
(10)
(11)
(12)
(13)
(14)
(15)
(16)
(17)
(18)
(19)
(20)
(21)
(22)
(23)
(24)
(25)
(26)
(27)
(28)

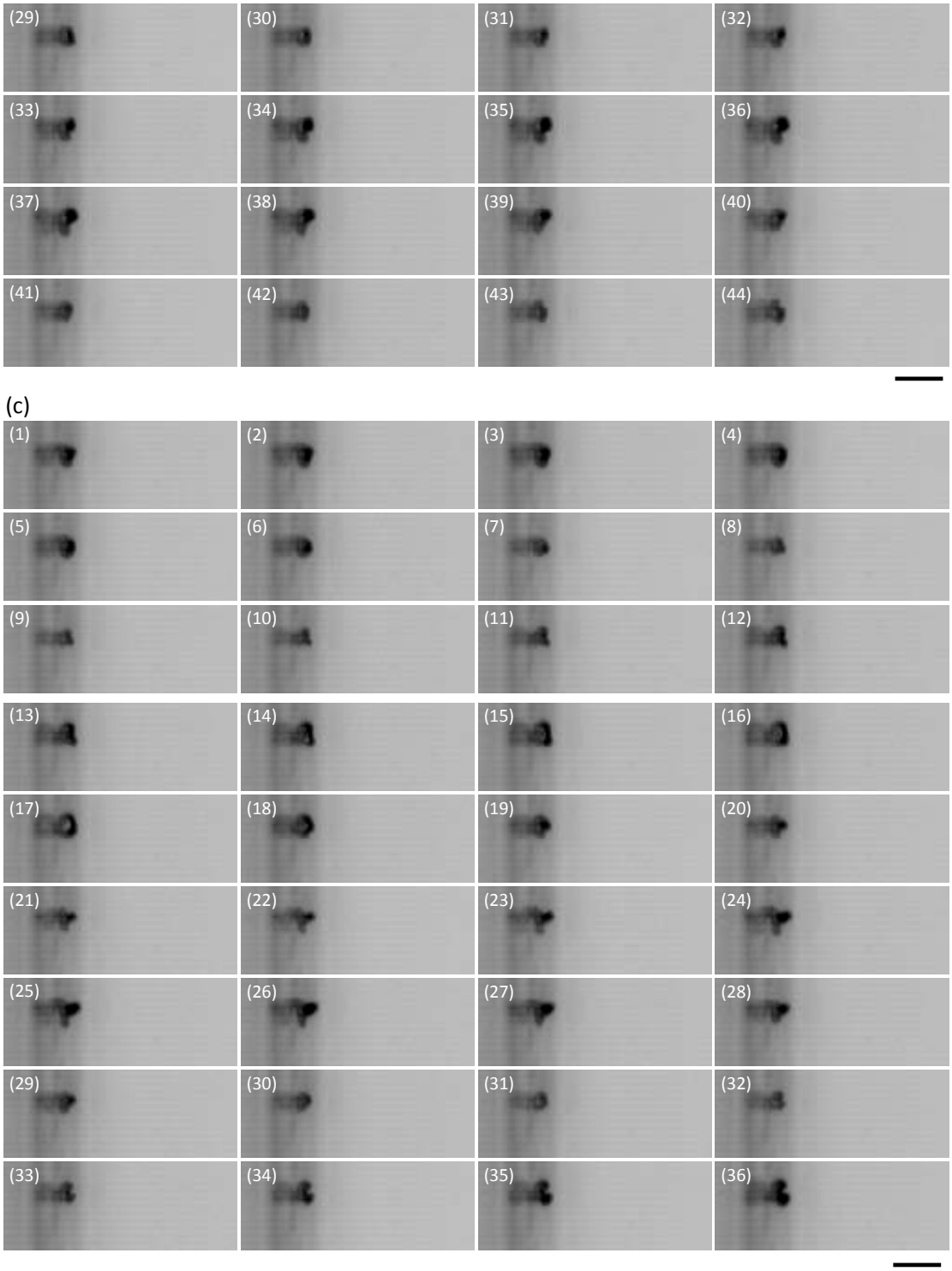

Figure 6.12: Selected frames from a video of bubble oscillation near a surface at 20 kPa. The bubble radius is 52 μm. (a) the bubble oscillates with a non-spherical shape when it is approaching glass 1. (b) the arrival of the bubble on the surface. (c) the bubble oscillates with a non-spherical shape on the surface. Viewing from top to bottom and left to right. The time interval between each frame is 1.9 μs. The scale bar represents 200 μm.

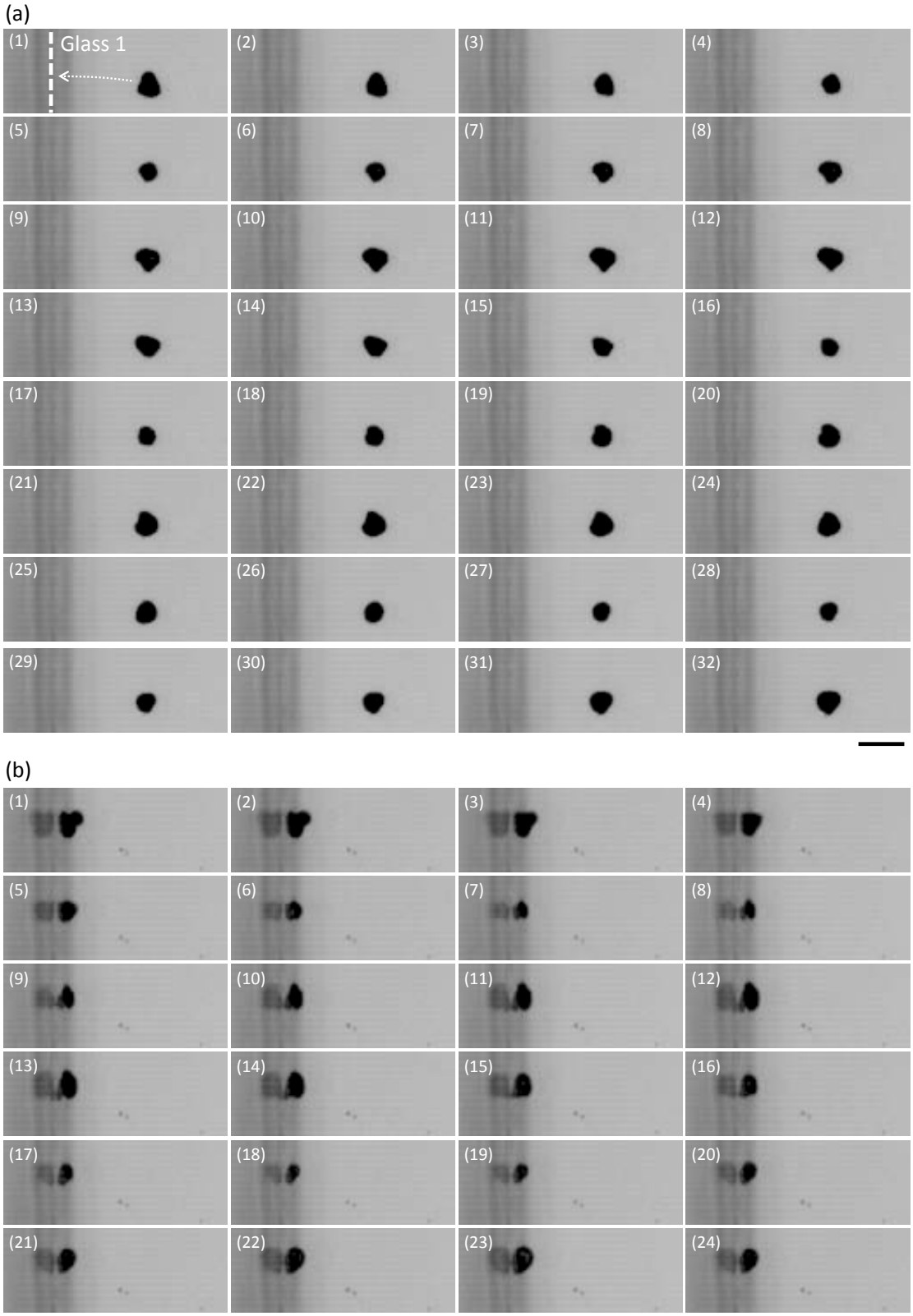
(a)
(1)
Glass 1
(2)
(3)
(4)
(5)
(6)
(7)
(8)
(9)
(10)
(11)
(12)
(13)
(14)
(15)
(16)
(17)
(18)
(19)
(20)
(21)
(22)
(23)
(24)
(25)
(26)
(27)
(28)
(29)
(30)
(31)
(32)
(b)
(1)
(2)
(3)
(4)
(5)
(6)
(7)
(8)
(9)
(10)
(11)
(12)
(13)
(14)
(15)
(16)
(17)
(18)
(19)
(20)
(21)
(22)
(23)
(24)

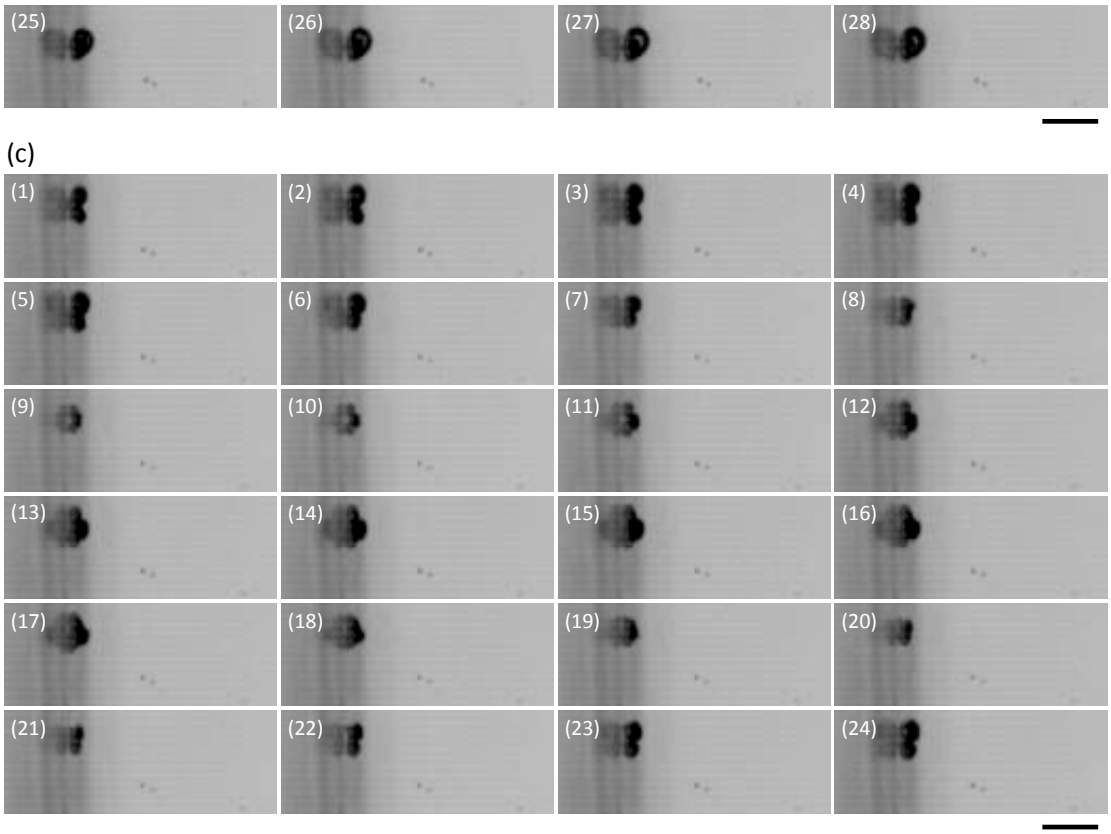

Figure 6.13: Selected frames from a video of bubble oscillation near a surface at 28.7 kPa. The bubble radius is 56 μm. (a) the bubble oscillates with a non-spherical shape when it is approaching glass 1. (b) the arrival of the bubble on the surface. (c) the bubble oscillates with a non-spherical mode on the surface. Viewing from top to bottom and left to right. The time interval between each frame is 1.9 μs. The scale bar represents 200 μm.

Similarly, a bubble of 56 μm radius experiences a strong oscillation at 28.7 kPa in Fig. 6.13. Irregular surface shape is seen for this bubble during its translation. Glass 1 forces the bubble to change its shape even before its hit on the surface. The non-spherical shape becomes more substantial when the bubble starts to oscillate on the surface (Fig. 6.13 (b - c)).

6.4 Discussion of the experimental results

At a given driving frequency, a bubble's oscillation is influenced by external pressure amplitude, bubble size, boundary conditions and neighboring bubbles. The following section discusses the conditions to excite the spherical and non-spherical bubble

oscillations.

6.4.1 Bubble translation with a spherical shape

For bubbles translating with spherical shapes (see Fig. 6.7 - 6.10), their pulsations synchronize with the driving frequency in the far field away from glass 1. The ratio of the maximum radius to the equilibrium radius increases with an increase of the external pressure amplitude. When the bubbles approach glass 1, the influence of the wall on the bubble oscillations becomes more significant. In Fig. 6.7 (b), for example, the maximum bubble radius increases from 45 μm when it translates in the far field, to 50 μm when it oscillates on the surface at 11.5 kPa. This change can be attributed to the shift of bubble resonance frequency as seen in Fig. 6.3. The resonance frequency decreases from 64 kHz (away from glass 1) to 59 kHz (on the wall) which is closer to the driving frequency (46.8 kHz). Thus, the bubble is anticipated to experience a stronger oscillation on the wall.

At a higher pressure amplitude (20 kPa), the boundary can not only shift a bubble's resonance frequency but also trigger non-spherical oscillation. In Fig. 6.9, for instance, a 43 μm radius bubble can switch from a spherical oscillation when it is away from glass 1 to the $n = 3$ mode when it is oscillating on the wall. According to Eq.6.8, a non-spherical oscillation mode can be excited when the pressure exceeds a threshold. Fig. 6.14 shows the pressure thresholds of modes $n = 2 - 6$ before and after the 43 μm bubble's arrival on glass 1 (Fig. 6.9). The pressure threshold of mode $n = 3$ shifts to a lower frequency range when the bubble oscillates on glass 1, and is lower than the given external pressure amplitude. That means the $n = 3$ mode is the easiest one to be excited when the bubble oscillates on the wall.

Moreover, when a bubble experiences a violent oscillation, glass 1 can force the bubble to oscillate non-spherically even without touching the surface. In Fig. 6.10, for example, the bubble changes its shape before its arrival on glass 1 at 28.7 kPa. On the one hand, glass 1 lowers the pressure threshold for exciting non-spherical bubble oscillation as seen in Fig. 6.14. On the other hand, the rapid compression of bubble surface at the bubble-wall contact area promotes the growth of its non-spherical shape, and eventually leads to the split of the bubble (Fig. 6.10 (b)).

Another factor influences the bubble oscillation is the existence of neighboring bubbles. The coalescence of bubbles can also excite a bubble's non-spherical behavior (Fig. 6.10). When the two bubbles are approaching each other, their shapes are deformed significantly owing to the bubble-bubble interactions as discussed in the previous chapters. The combination creates a new large bubble whose pressure threshold of non-spherical oscillation is different from that of its precedents. The relationship between bubble radii and pressure thresholds is shown in Fig. 6.15. Expanded bubble volume from the coalescence leads the newly formed bubble to oscillate at a higher mode, and results in the complicated surface deformation as seen in Fig. 6.10. For example, the minimum pressure amplitude that can only excite n = 3 mode for a bubble of 43 μm radius could cause a bubble of 60 μm radius to oscillate at higher oscillation modes.

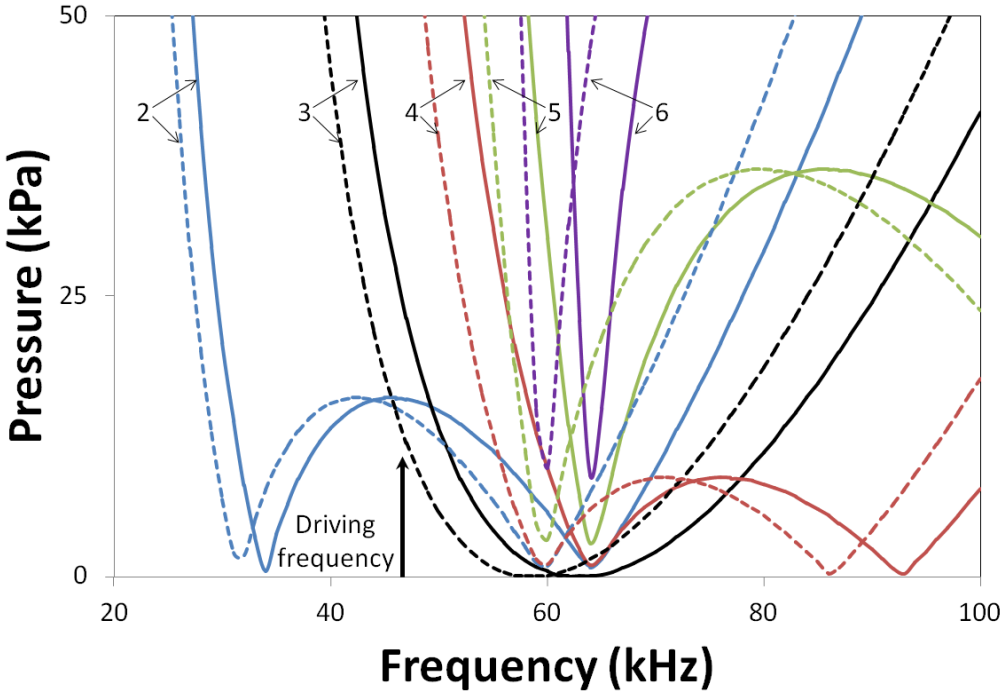

Figure 6.14: Pressure thresholds for exciting the non-spherical oscillation of a bubble of radius of 43 μm (Fig. 6.9). The pressure thresholds are calculated based on Eq. 6.8. Solid lines are the pressure thresholds for a bubble away from glass 1, and the dashed lines are the pressure thresholds for a bubble attached on the wall. The non-spherical oscillation modes are numbered from 2 to 6.

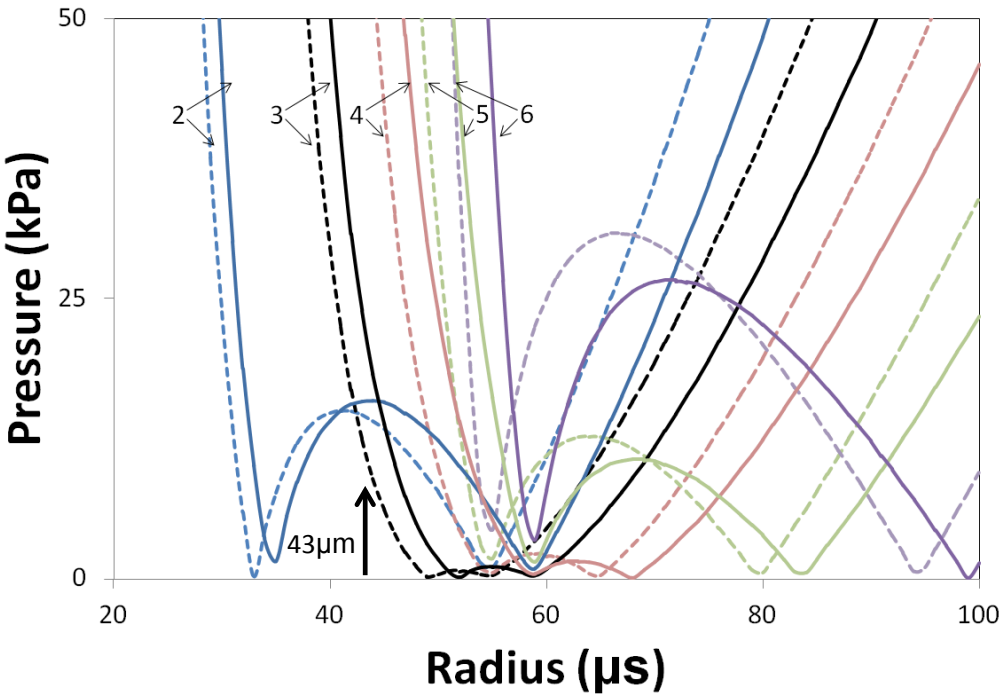

Figure 6.15: The pressure threshold of exciting non-spherical bubble oscillation. The bubble radii ranging from 20 μm to 100 μm. The non-spherical modes are numbered from 2 to 6. The pressure thresholds are calculated based on Eq. 6.8 at 46.8 kHz. Solid lines represent the pressure threshold of a bubble away from glass 1, and the dashed lines are the pressure thresholds for a bubble attached to the wall.

6.4.2 Bubble translation with a non-spherical shape

In the far field away from glass 1, a bubble can oscillate non-spherically when its size exceeds a threshold. For example, it can be seen from Fig. 6.15 that the $n = 3$ mode is easiest one to be excited for a bubble of 54 μm (Fig. 6.11) in the far field. Also, the pressure threshold of the third mode is lower than the driving pressure amplitude (11.5 kPa). Thus, the bubble in Fig. 6.11 can oscillate with the $n = 3$ mode when it is away from glass 1. After arriving on the surface, the bubble switch its shape to the $n = 4$ mode. Similar to the spherical oscillation case, glass 1 lowers the pressure threshold for the excitation of non-spherical modes. Particularly, the fourth mode has a similar threshold level as the third one which may explain the bubble shape change in this case.

At a higher pressure amplitude, a bubble can undergo a more complicated surface deformation. In Fig. 6.12, the glass surface significantly depresses the bubble surface

which in turn leads to an even more deformed shape. The combination of the high pressure amplitude and the nearby wall creates an irregular shape oscillation as seen in Fig. 6.12. The severe shape deformation is also exemplified in Fig. 6.13 where the target bubble completely loses its symmetric shape and oscillates in a more violent manner.

6.5 Microstreaming around an oscillating bubble

After displaying the bubble oscillation modes near a surface, the next step is to investigate the characteristics of microstreaming around a bubble. The revelation of the flow field near a bubble was accomplished using PIV. In Fig. 6.16, a bubble of 70 μm radius oscillates on the glass surface in a liquid filled with the tracer particles (radius = $10\mu m$). The pressure amplitude was 11.5 kPa.

The bubble surface oscillation results in a flow motion around it. This flow motion can push the particles away or attract them to the bubble depending the separation distance between the bubble and particle. On the other hand, it is possible that the motion of the particles could influence the bubble oscillation because they could change the liquid property near the bubble. However, little theory work is found in the literature to discuss the bubble-particle interaction for an oscillating bubble on a surface. Moreover, it is very difficult to quantify the influence of particles on the bubble oscillation with the current test rig. This topic is important in understanding the bubble induced microstreaming, and would be investigated in the future.

As the formation of microstreaming is a time averaged effect, it normally takes a few cycles to move the tracer particles in the liquid medium. Thus, the particles shown in Fig. 6.16 are almost stagnant during this one acoustic cycle. Based on the video result, it was found that the bubble attracts the tracer particles in the far field to move towards the bubble, while it repels the nearby particles back into the liquid and forms a flow circulation. A typical particle trajectory as shown in Fig. 6.16 is extracted in Fig. 6.17. The origin of the coordinate system is set at the bubble center. It needs to be pointed out here that the particle trajectory is only partially shown in Fig. 6.17 due to the limited image quality of the sample video.

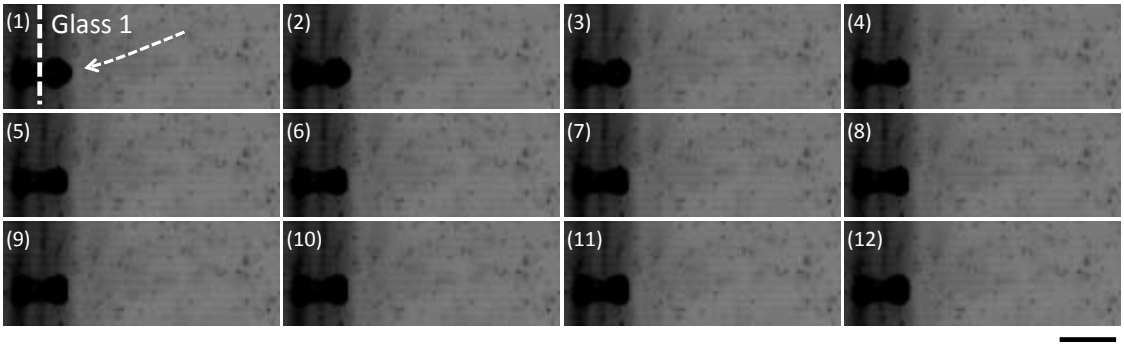

Figure 6.16: Selected frames from a video of bubble oscillation near a surface. Viewing from top to bottom and left to right. The scale bar represents 200 μm. The time interval between each frame is 1.9 μs. The bubble oscillation and microstreaming are better seen in the video on the attached CD.

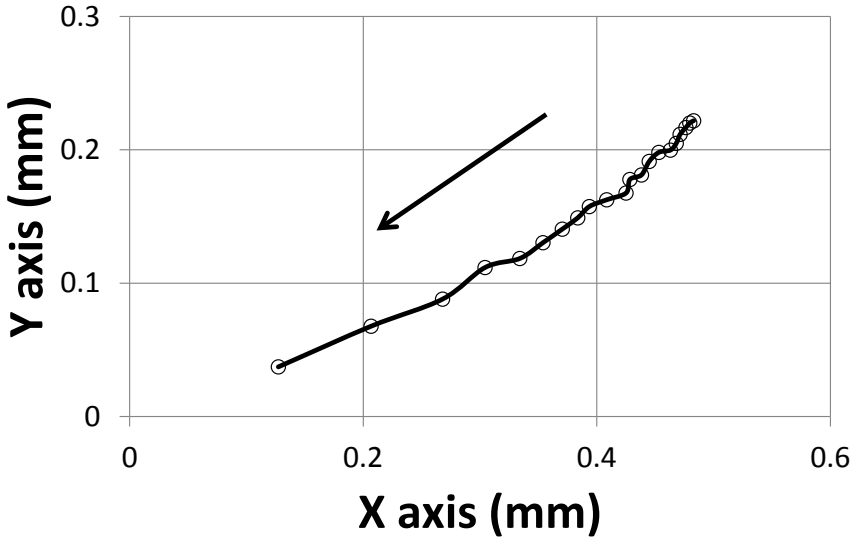

Figure 6.17: A typical particle trajectory of a tracer particle (the white dashed line in Fig. 6.16). The bubble is located at x = 0, y = 0.

It has been recognized that both the spherical and non-spherical oscillations can contribute to the microstreaming around a bubble at a moderate pressure amplitude. To analyze the influence of both modes on the formation of microstreaming, the tracer particle trajectory as shown in Fig. 6.17 is used here as a sample. The target bubble was oscillating with the $n = 4$ mode as seen in Fig. 6.16 (a better video result is provided in the attached CD).

The measured velocities in the x and y axes are extracted from the particle trajectory as shown in Fig. 6.17. The velocities generated from the spherical oscillation are calculated based on Eq.6.15 by extracting the x $(u_r cos\theta + u_\theta sin\theta)$ and y $(u_r cos\theta + u_\theta sin\theta)$ axis velocity components respectively. Similarly, Eq.6.18 is used to predict the x and y axes components of the flow velocity generated from the non-spherical oscillation. The amplitudes of the spherical oscillation and non-spherical oscillations are estimated from the video result. The driving frequency is 46.8 kHz. The bubble is located at $x = 0$, $y = 0$, and the particle moves from the right hand side to the left. In the x axis (Fig. 6.18 (a)), for example, the velocity from the spherical mode gradually grows from 0 mm/s at $x = 0.48$ mm to 3 mm/s at $x = 3$ mm, which are closer to the observed trend from 0.5 mm/s to 4.7 mm/s in the experiment. The velocity from the non-spherical mode ($n = 4$ mode), however, shows little sign of growth over the same period. After that, both the spherical and non-spherical modes experience a rapid growth where the spherical mode velocity arises from 3 mm/s at $x = 0.48$ mm to 16 mm/s at $x = 2$ mm, which is higher than the 10 mm/s as seen in the experiment. Meanwhile, the 4th mode velocity is still far smaller than the test result. It needs to be pointed out here that the velocity profile between $x = 0$ and 2 mm is not able to be determined from the experimental data due to the limited frame rate and the relatively fast particle movement within this area. In the y axis, a similar trend is seen in Fig. 6.18. The observed velocity trend is much more in consistent with the spherical mode velocity than that of the 4th mode one. According to Eq.6.14 and 6.17, the streaming function or flow velocity of spherical mode decays from the bubble center at a speed of the order of r^{-1}, while the non-spherical ones experience a much faster fading at an order of r^{-7} (by setting $n = 4$). In the far field, therefore, the microstreaming is dominated by the spherical oscillation rather than the higher modes. The influence from the spherical pulsation could be matched with its non-spherical counterpart in the vicinity of bubble surface.

That means it is possible for the non-spherical oscillations to contribute to the flow disturbance in the near field. However, the microstreaming in the vicinity of a bubble surface can not be measured with the present test rig.

The calculated streaming patterns from the spherical mode and the $n = 4$ mode are compared with the tracer trajectory in Fig. 6.19. It is seen from the comparisons that the tracer trajectories are more likely to overlap with the anticipated microstreaming from the spherical mode. This comparison clearly shows the observed far field streaming pattern is a result of the bubble spherical oscillation.

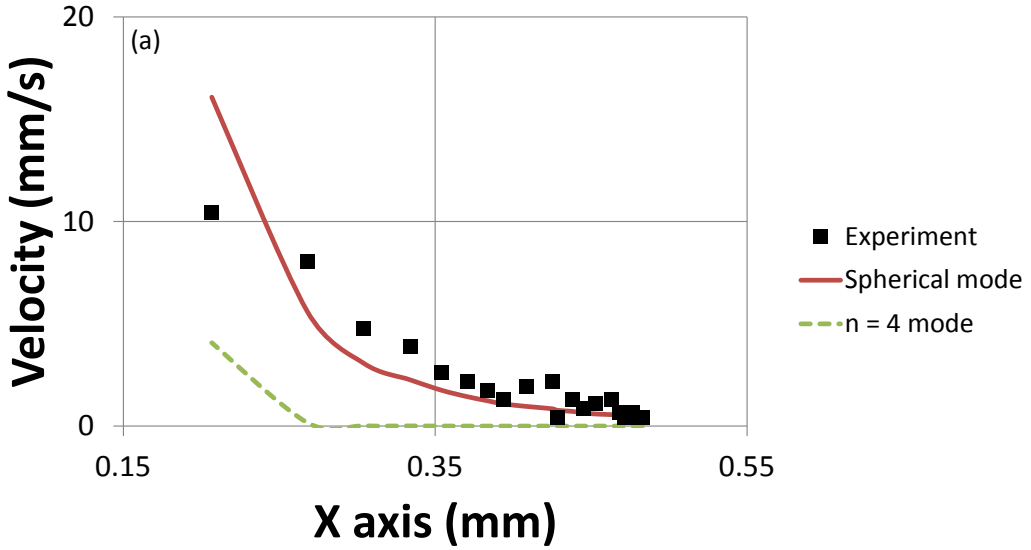

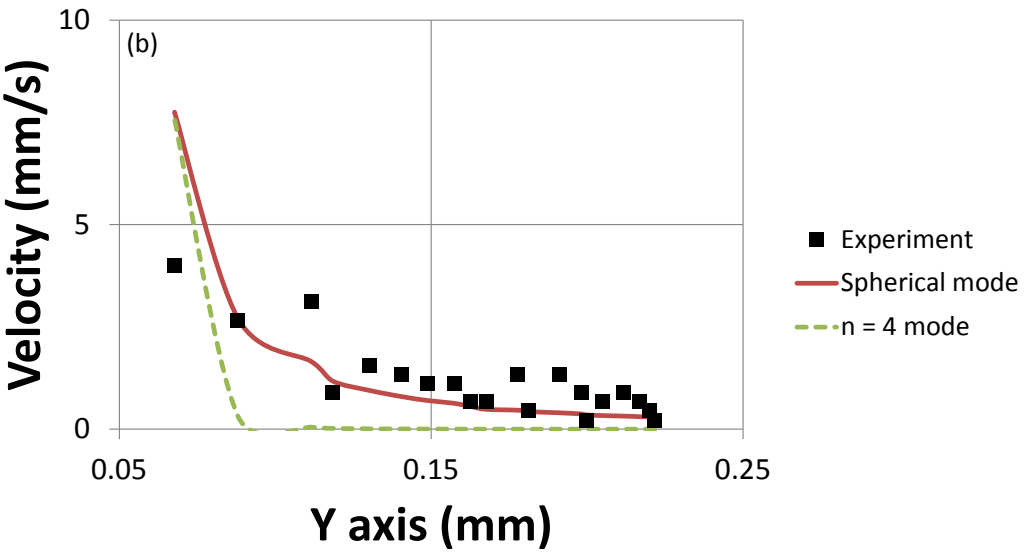

Figure 6.18: Calculated velocity profiles of the observed trajectory. (a) The velocity in the x axis obtained from the experiment, the spherical mode, and the $n = 4$ mode; (b) The velocity in the y axis obtained from the experiment, the spherical modes, and the $n = 4$ mode.

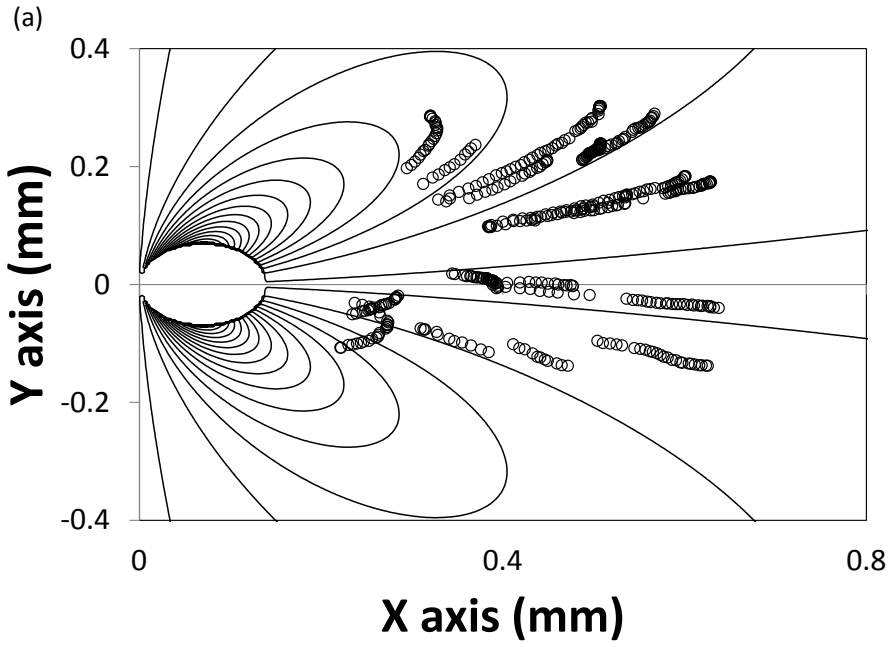

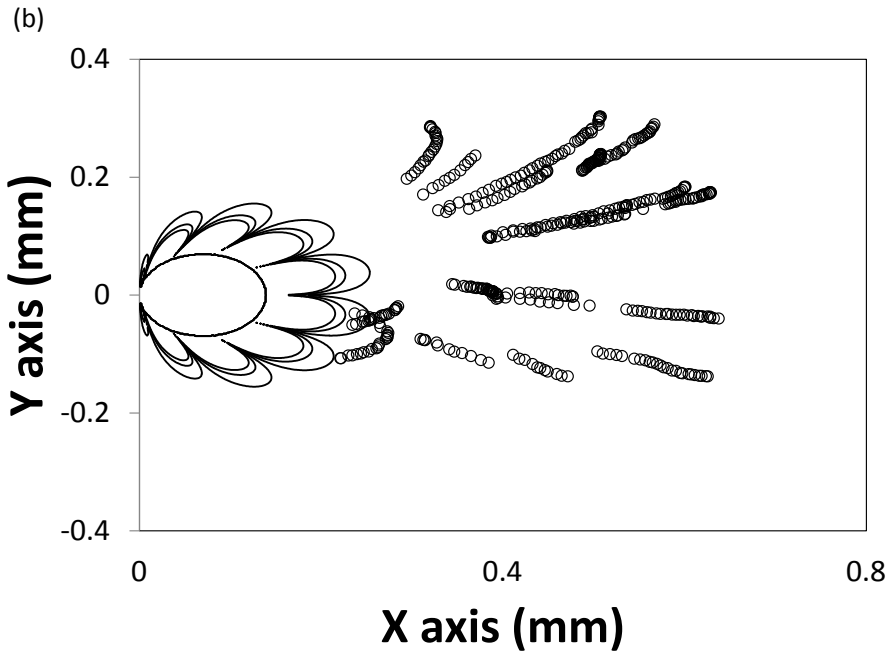

Figure 6.19: The microstreaming from the spherical mode, the 4th mode and the experiment. (a) a comparison between the experiment and the spherical mode induced microstreaming. (b) a comparison between the 4th mode induced microstreaming and the observed tracer trajectory.

6.6 Conclusion

The bubble dynamics near a surface were discussed in this chapter. The bubble oscillation was found to be influenced by the driving frequency, external pressure amplitude, bubble size, boundary conditions and neighboring bubbles. The excitation of non-spherical modes requires the pressure amplitude to exceed a certain threshold for a given size of bubble. On the other hand, at a fixed pressure amplitude, different bubble sizes would result in different oscillation modes. For a bubble translating with a spherical shape, a nearby surface can lower the pressure threshold of non-spherical oscillation modes. Thus, the bubble can shift from the spherical oscillation to a non-spherical one at the same pressure amplitude. An increase of pressure amplitude forces the bubble to undergo a stronger surface shape deformation which was substantially enhanced by a neighboring surface. The nearby surface significantly compressed the bubble-wall contact area and forced the target bubble to lose its symmetric shape within a very short period. Meanwhile,

for a bubble of size above a certain threshold, it can oscillate with a non-spherical shape in the far field. Similarly, when the bubble approached the target surface, a lowered non-spherical oscillation pressure threshold forced the bubble to switch to another oscillation mode. The bubble oscillation mode is further complicated at a higher pressure amplitude, which could excite a higher oscillation mode. All of the observed bubble oscillation mode transitions were in good agreement with the theoretical predictions.

The microstreaming was quantified using the PIV. It was noticed that both the spherical and non-spherical oscillation modes can cause microstreaming at a moderate pressure amplitude. In the far field, the non-spherical mode decayed at a much faster speed than the spherical one. Thus, its contribution to the far-field microstreaming was much less influential than its spherical counterpart, and the observed far field streaming pattern was dominated by the spherical oscillation mode. In the near field, the contribution from the non-spherical mode to the microstreaming could be significantly enhanced. However, this cannot be observed with the current test equipment.

Chapter 7

Ultrasonic cleaning test

Although the macroscopic cleaning effects using micro-bubbles have been widely recognized, the microscopic mechanism of ultrasonic cleaning has not yet been fully explained. In the previous studies, micro-bubbles were assumed to oscillate spherically at all time. However, in real life, a bubble can oscillate spherically and non-spherically during the ultrasonic cleaning process. The influence of non-spherically oscillating bubbles on the particle removal is still unknown. In this chapter, the hydrodynamic forces that are induced by spherical and non-spherical micro-bubbles are shown, and their influences on the particle detachment process are discussed in detail. The investigations are threefold: first, the cleaning effect is exemplified by a series of ultrasonic cleaning tests using the designed test cell; second, theoretical background of particle adhesion force and cleaning forces is given; third, from a mechanic point of view, a possible cleaning mechanism is explained by estimating the relationship between different torques that are exerted on a contamination particle.

7.1 Experimental configuration

To investigate the mechanism underlying the ultrasonic cleaning, the test cell presented in chapter 4 and 5 was used for a cleaning test. A schematic diagram of the experimental procedure is illustrated in Fig. 7.1. Silicon dioxide particles (Micro particles based on silicium dioxide, Sigma-Aldrich, UK) were selected as the con-

tamination particles. In order to deposit these particles on the sample glass plates, the glass surfaces need to be first cleaned by the wet-clean process, or known as SC-1, which is based on the RCA Standard Clean [153]. The glass plates were inserted into a mixture of ammonia solution (Ammonia solution 28 %, VWR, UK), hydrogen peroxide solution (Fluka Analytical, UK) and distilled water at a ratio of $1:1:5$ for 5 minutes. The silicon dioxide solution was then placed on the glass plates and the particles were deposited on the surfaces after the evaporation of liquid. A microscope (Axioskop, Zeiss, Germany) was used to record the contaminated surfaces before and after the ultrasonic treatment. The positions of the glass plates were fixed on the microscope with two scale bars orthogonal to each other.

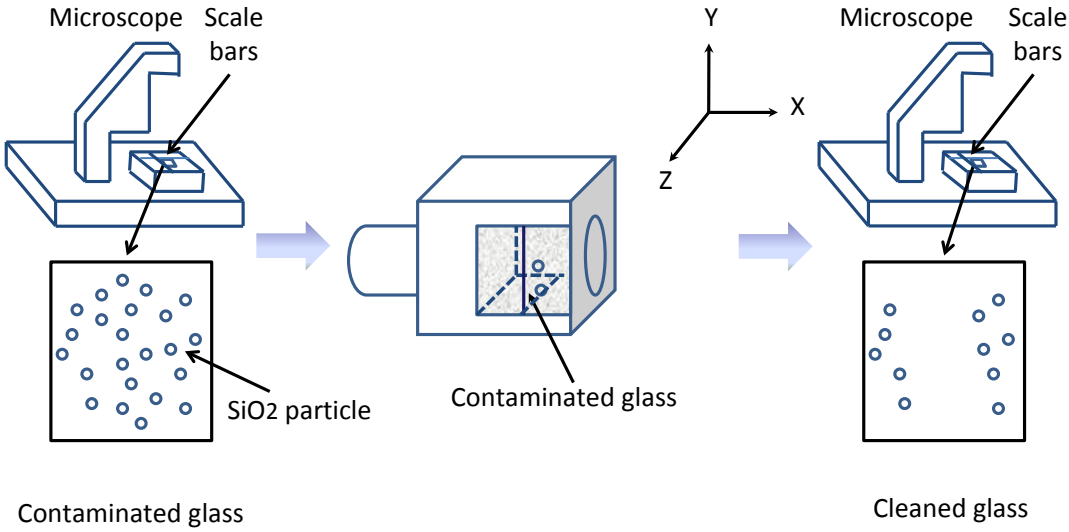

Figure 7.1: A schematic diagram of the ultrasonic cleaning setup. The contaminated glass surfaces are observed by the microscope at the same spot before and after the ultrasonic treatment. The edges of the glass plate are aligned by two scale bars to maintain the glass position as the same in each test.

7.2 Result

Fig. 7.2 shows the contaminated glass plates before and after the ultrasonic treatment (top view in Fig. 7.1). During each test, a liquid drop with a mixture of silicon dioxide particle and liquid was placed on the glass surface. Due to the evaporation of liquid, particles accumulated on the edge of the liquid drop, and formed the layered structure as seen in Fig. 7.2 (a1, b1, c1).

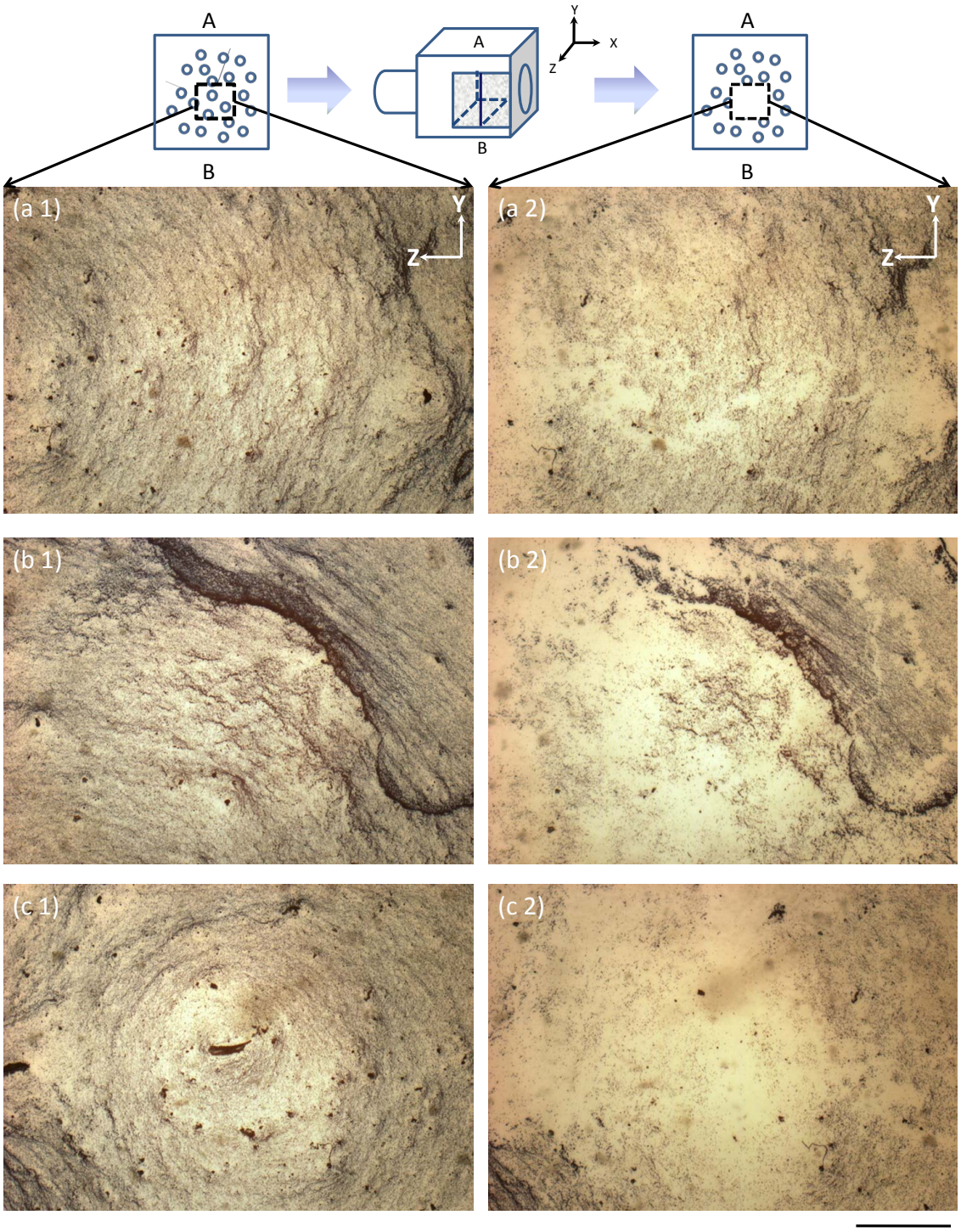

Figure 7.2: The ultrasonic cleaning of micro-sized particles using the proposed test cell. The driving frequency was 46.8 kHz. The pressure amplitude was 11.5 kPa. The sample plates are cleaned for (a) 30 seconds; (b) 1 minute; (c) 2 minutes. Pictures on the left hand side are samples before the ultrasonic treatment, and the cleaning effects are shown in the pictures on the right hand side. The scale bar is 500 μm.

It can be seen that the active micro-bubbles can achieve the particle removals from the sample glass surfaces. The glass plates were inserted into the test cell for 30 seconds, 1 minute, and 2 minutes respectively. The resonator was driven at 46.8 kHz, and the pressure amplitude was 11.5 kPa. The cleaning effect, particularly within the areas where contamination particles were formally densely accumulated, are clearly seen from the comparisons. No obvious damage was noticed from the sample surfaces at this scale. It needs to be pointed out here that these cleaned areas are not uniformly distributed on the surfaces which is due to the interactions between bubbles on the glass plates. As discussed in chapters 3 and 4, bubbles of different sizes would arrive on different locations on the glass surfaces. Also, the secondary Bjerknes force can change the bubble trajectories during their translations. Thus, it is possible that the observed cleaning effect is achieved by several neighboring bubbles rather than an isolated one, and their interactions result in the irregular cleaning path on the surfaces as seen in Fig. 7.2. However, the actual bubble number can not be measured with the present test rig. Moreover, the cleaning efficiency was found as a function of operation time. It can be seen from Fig. 7.2 ($a1$, $b1$, $c1$) that a longer operation time could increase the cleaning efficiency by cleaning more contaminated areas.

7.3 Theory

7.3.1 Particle adhesion force

To understand the cleaning mechanism, one needs to revisit the different external forces exerted on the contamination particles. The primary forces responsible for the particle adhesion are the van der Waals force and electrostatic force. Electrostatic force is dominating for holding large particles (radius $\geq$ 25 μm) on a substrate, while van der Waals force plays an important role for small particles (radius $\leq$ 10 μm) [154]. In this study, the particle radii are 1 μm, and therefore, only the van der Waals force is considered.

Let us first suppose a rigid particle sitting on a substrate without any shape deformation (Fig. 7.3 a, [155]). The van der Waals force between the particle and the

substrate is given by [156]:

$$F_{vdw} = \frac{A_H R_{particle}}{6 Z_{particle}^2} \tag{7.1}$$

where A_H is the Hamaker constant, $R_{particle}$ is the particle radius, $Z_{particle}$ is the interfacial separation of atomic centers at contact.

From the energy point of view, the work of adhesion (W) of a particle is defined as [157]:

$$W = \frac{A_H}{12\pi Z_{particle}^2} \tag{7.2}$$

The van der Waals force for a rigid particle can then be converted to [157]

$$F_{vdw} = 2\pi W R_{particle} \tag{7.3}$$

However, in real life, particles are normally supposed to be elastic rather than completely rigid. That means the particle-substrate contact region is deformable under the adhesion force that pulls the particle on the surface (Fig. 7.3 b). By taking the shape deformation into account, the van der Waals force for a deformable particle is [158]:

$$F_{vdw}^{deform} = F_{vdw}(1 + \frac{a_{particle}^2}{R_{particle} Z_{particle}}) \tag{7.4}$$

where $a_{particle}$ is the particle-substrate contact radius (Fig. 7.3 b). Over the past few decades, several theories have been developed to explain the adhesion induced deformation [159–162]. One of them, the JKR theory (named after Johnson, Kendall, and Roberts) [161] that considers the surface energy and deformation, is widely used to explain the adhesion mechanics of deformable particles. In the JKR theory, the contact radius is a function of the compressive and tensile interactions, and is given by [161]:

$$a^3_{particle} = \frac{6W\pi R^2_{particle}}{K}$$

$$K = \frac{4}{3\pi(k_{particle} + k_{surface})}$$

$$k_{particle} = \frac{1 - \upsilon^2_{particle}}{\pi E_{particle}}, k_{surface} = \frac{1 - \upsilon^2_{surface}}{\pi E_{surface}} \tag{7.5}$$

where υ and E are the Poisson's ratio and Young's modulus of the material respectively.

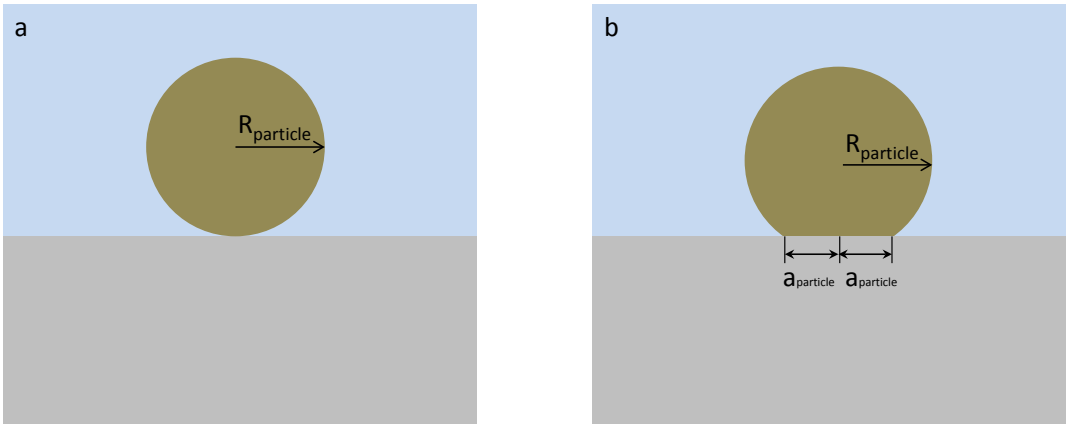

Figure 7.3: Adhesion between a particle and a solid surface. (a) a rigid sphere particle sitting on the substrate without any shape deformation; (b) a deformed particle sitting on the surface with the contact radius $a_{particle}$.

7.3.2 Cleaning forces

During ultrasonic cleaning process, contamination particles experience several hydrodynamic and acoustic forces generated by the acoustic field and oscillating microbubbles. Kim et al [24] identified the main influential cleaning forces for the removal of micrometer-sized particles, and their results are briefly shown here. Initially, a particle sitting on a substrate at rest, the van der Waals force (Eq.7.4) is responsible for the particle adhesion as seen in Fig. 7.4 a.

Acoustic pressure gradient force

Suppose an ultrasound field is established in the direction perpendicular to the wall (Fig. 7.4 b), the acoustic field results in a pressure gradient (∇p) across the particle surface. Accordingly, the particle experiences an acoustic pressure gradient force, which is given by [24]:

$$F_p = \nabla p V_{particle} \tag{7.6}$$

where $V_{particle}$ is the particle volume.

Interface sweeping force

In addition to the sound field, acoustically-driven bubbles are also transported to the vicinity of the particle. For a bubble that is adjacent to the particle (Fig. 7.4 c), the Laplace pressure, which arises from the pressure difference between the gas inside and liquid outside the bubble, generates an interface sweeping force on the particle [24]:

$$F_{if} = \frac{2\pi R_{particle}^2 \sigma}{R_0} \tag{7.7}$$

where σ is the surface tension of a bubble with a radius of R_0.

Dynamic pressure gradient force

Moreover, for a particle located at a distance of d_{bp} from the bubble, the microstreaming that is caused by the bubble oscillation generates a pressure gradient on the particle. Therefore, the particle experiences a dynamic pressure gradient force [24]:

$$F_d = \frac{\partial p_d}{\partial r} V_{particle}$$

$$p_d \sim \frac{1}{2}\rho u^2 \tag{7.8}$$

where r is the distance between a monitoring point and the bubble center. ρ is the liquid density, and u is the liquid velocity.

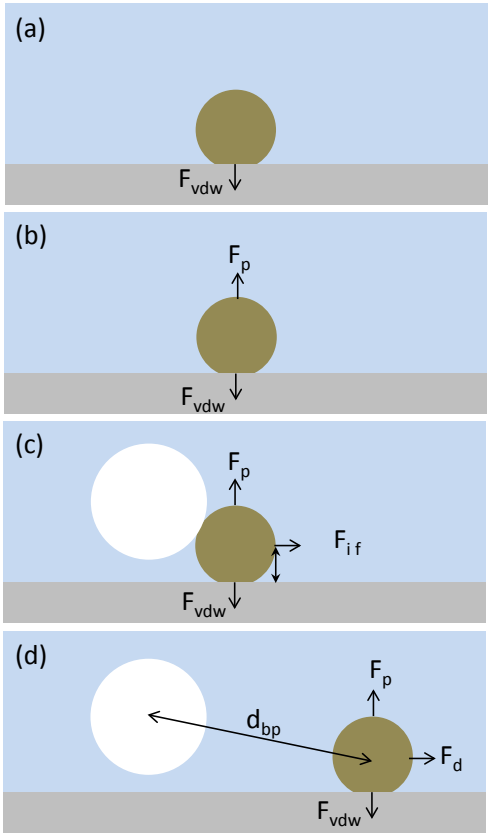

Figure 7.4: The relationship between the particle adhesion force and cleaning forces. (a) a particle is held on a substrate by the van der Waals force in the absence of any external loads. (b) The particle is influenced by the acoustic force and the van der Waals force in the presence of an ultrasound field. (c) An oscillation bubble generates an interface sweeping force on the particle that is located within the bubble oscillation range. The combination of the van der Waals force, the acoustic force, and the interface sweeping force decides the particle movement. (d) For a particle sitting in the far field, it experiences forces from the pressure gradient that is generated by the bubble pulsation, the van der Waals force, and the acoustic force simultaneously.

7.3.3 Linear torque balance model

Three main models of particle removal from a substrate have been reported in the literature [163]. They are rolling, sliding, and lifting models. It has been recognized

that the rolling model is mainly responsible for the removal of spherical particles from a flat surface [163]. Hence, only the rolling model is considered here. Recently, a linear torque balance model was proposed by Kim et al [24] for explaining the particle detachment process in conventional megasonic cleaning. This model has been verified to be able to estimate the different torques exerted on a micrometer-sized particle near an oscillating bubble. Therefore, their work is briefly reviewed here.

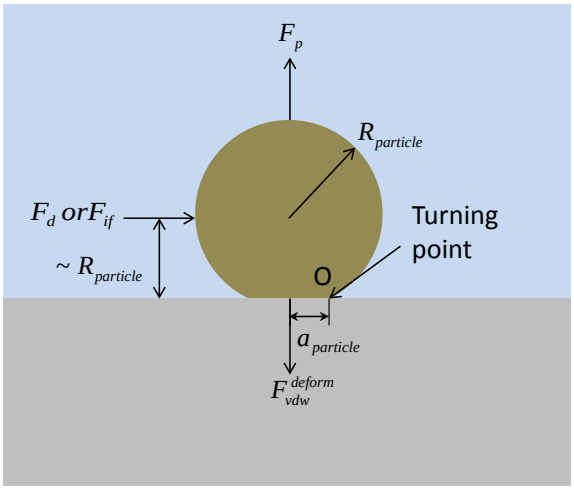

Figure 7.5: Different forces exerted on a particle attached to a surface.

Adhesion torque

The detachment of a particle can be analyzed by exploring the balance between different torques exerted on it. The turning point of the particle is located on the periphery of the contact region (point O in Fig. 7.5). The adhesion torque τ_a that is generated by the van der Waals force with the moment arm ($\sim a_{partitiicle}$) is given by [24].

$$\tau_a \sim F_{vdw}^{deform} a_{particle} \tag{7.9}$$

Acoustic pressure gradient torque

When an acoustic field with an amplitude of P_a is established, for example, in the direction perpendicular to the solid surface (Fig. 7.4 b), the acoustic pressure gradient torque τ_p that is generated by the acoustic pressure gradient force with the moment arm ($\sim a_{particle}$) is [24]:

$$\tau_p \sim \frac{2P_a\omega R_{particle}^3 a_{particle}}{3c} \tag{7.10}$$

where ω is the angular frequency, and c is the sound velocity in the liquid.

Interface sweeping torque

Moreover, during the cleaning process, active bubbles are brought to the vicinity of the particles under the acoustic and hydrodynamic forces. For a particle sitting within the bubble oscillation range (Fig. 7.4 c), it experiences an interface sweeping torque τ_{if} due to the interface sweeping force F_{if} with the moment arm ($\sim R_{particle}$) [24]:

$$\tau_{if} \sim 2\pi R_{particle}^3 \sigma / R_0 \tag{7.11}$$

Dynamic pressure gradient torque

For a particle sitting outside the bubble oscillation range, the bubble also exerts a dynamic pressure gradient torque on the particle [24]:

$$\tau_d \sim F_d R_{particle} = \frac{\partial p_d}{\partial r} V_{particle} R_{particle}$$

$$p_d \sim \frac{1}{2}\rho u^2 \tag{7.12}$$

It is worth mentioning that the flow velocity u that was estimated in [24] is based

on a linear spherical bubble oscillation model at a large pressure amplitude (260 kPa). The contribution from the non-spherical oscillation to the flow velocity was not considered by Kim et al. However, as seen in the previous chapter, both the spherical and non-spherical oscillations can cause microstreaming at a moderate pressure amplitude. Thus, the dynamic pressure torque given in [24] is expanded here by including the influence from both the spherical and non-spherical bubble oscillations. For a spherical oscillation, the dynamic pressure torque is:

$$\tau_{ds} \sim \frac{\partial p_{ds}}{\partial r} V_{particle} R_{particle}$$

$$p_{ds} \sim \frac{1}{2}\rho(\frac{1}{r^2 sin\theta}\frac{\partial \bar{\Psi}_{11w}}{\partial \theta})^2 \tag{7.13}$$

For a non-spherical oscillation, the torque is:

$$\tau_{dn} \sim \frac{\partial p_{dn}}{\partial r} V_{particle} R_{particle}$$

$$p_{dn} \sim \frac{1}{2}\rho(\frac{1}{r^2 sin\theta}\frac{\partial \bar{\Psi}^n_{11w}}{\partial \theta})^2 \tag{7.14}$$

where $\bar{\Psi}_{11w}$ and $\bar{\Psi}^n_{11w}$ are the spherical and non-spherical streaming functions as defined in Eq.6.14 and 6.17.

7.4 Discussion of the experimental result

Based on the linear torque balance model, a particle can be detached from a substrate when the removal torques outweigh the adhesion torque that holds the particle on the surface. In this section, the relationship between the adhesion torque τ_a, the acoustic pressure gradient torque τ_p, the interface sweeping torque τ_{if}, and the dynamic pressure gradient torque τ_d is discussed. The parameters used here are: A_H = 1×10^{-20}J, $R_{particle}$ = 1 μm, $Z_{particle}$ = 0.4 nm. $\upsilon_{particle}$ = 0.17, $\upsilon_{surface}$ = 0.2, $E_{particle}$ = 70 Gpa, $E_{surface}$ = 64 Gpa [164]. The bubble as shown in section 5.2.3 (R_0 = 70

μm, mode number n = 4) is used. This type of bubble was commonly observed under the present experimental condition, and therefore, is selected here for demonstration purpose. The external pressure amplitude is set as P_a = 11.5 kPa. The different torques exerted on particles of radii ranging from 0.1 to 10 μm are shown in Fig.7.6.

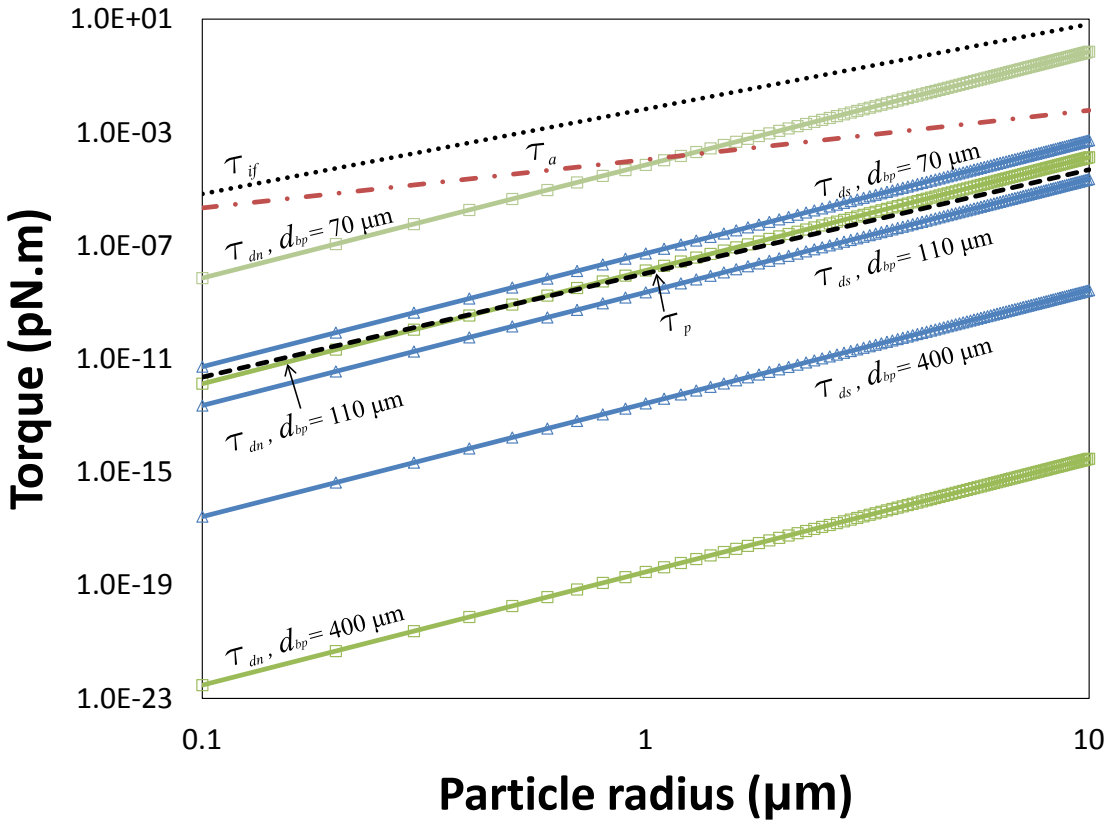

Figure 7.6: Torques generated by the particle adhesion force and other cleaning forces. The particle radius varies from 0.1 to 10 μm. The symbols for different torques are: particle adhesion force τ_a (-··-), acoustic pressure gradient τ_p (- - -), interface sweeping force τ_{if} (···), pressure gradient from spherical oscillation τ_{ds}, (-△-), pressure gradient from non-spherical oscillation τ_{dn} (-□-).

First, an acoustic pressure gradient torque τ_p is generated in the presence of an acoustic field. τ_p, however, is much weaker than the adhesion torque τ_a for most of the micro and sub-micrometer-sized particles. The magnitude difference between τ_p and τ_a increases with a decrease of particle size. Thus, it is hardly possible that the acoustic wave field alone can contribute to the removal of micrometer-sized particles.

Second, besides the acoustic field, acoustically-driven bubbles that are transported onto the solid surface can also influence the particle movement. For particles sitting within the bubble oscillation range, they could experience the interface sweep-

ing torque τ_{if} owing to the Laplace pressure. It can be seen from Fig.7.6 that τ_{if} is sufficiently strong to break the particle-substrate bonding for the micro and sub-micrometer-sized particles. Hence, it is possible to achieve the cleaning effect through the direct contact between micro-bubbles and particles.

Third, in addition to the nearby particles, a bubble can also generate a pressure gradient on a particle sitting out of the oscillation range. This dynamic torque τ_d is directly related to the characteristics of microstreaming around the bubble. As discussed in the previous chapter, both the spherical and non-spherical oscillations can contribute to microstreaming at a moderate pressure amplitude. At a large bubble-particle separation distance (d_{bp} = 400 μm), the dynamic torque τ_{ds} that is generated by spherical bubble oscillation is several orders of magnitude weaker than τ_a, but is stronger than the torque τ_{dn} that is generated from the non-spherical pulsation. With a decrease of d_{bp} to 110 μm, it can be seen from Fig.7.6 that τ_{dn} starts to outweigh its counterpart, but is still negligible compared with τ_a. When d_{bp} is shorten to 70 μm, τ_{dn} is finally able to break the particle-substrate bonding for micrometer-sized particles, while τ_{ds} hardly contributes to the particle removal within this range.

It needs to be pointed out here that this estimated relationship between the different torques exerted on a particle is to solely provide a qualitative understanding of the particle detachment process. To directly demonstrate the particle motion during the cleaning process, a more advanced experimental configuration needs to be developed. This is because the study of the motion of micro and nanometer-sized particles near micro-bubbles requires an optical experimental setup to be able to focus on an area of the scale of nanometer. At such a small scale, the observed microstreaming around the particles could be compared with the theoretical predictions. However, the diffraction limit of the best available conventional microscope is 0.2 μm [165], which is still larger than the nanometer-sized particles. Moreover, more direct observations of the particle-substrate bonding are needed to provide a more accurate prediction of the particle removal process. Ideally, the parameters of contamination particles and the surface, such as contact radius, particle-substrate separation distance, and the flatness of a solid surface etc, are preferable to be obtained using scanning electron microscopy and other optical observation techniques. With these improvements, it

is possible to control the complicated bubble-particle interactions at the nanometer scale.

7.5 Conclusion

The mechanism underlying the ultrasonic cleaning was investigated experimentally and theoretically using the designed test rig. From the experimental results, it was verified that the test cell was able to remove micrometer-size particles from glass surfaces, particularly the area where the particles were heavily aggregated. The cleaned areas were not uniformly distributed on the glass surfaces owing to the fact that the motion of a bubble on a surface is significantly influenced by the existence of nearby bubbles. A longer operation time was found to increase the cleaning efficiency.

The cleaning process was also explained by analyzing the relationship between different torques exerted on a particle. From the simulation result, it was found that the particles were held on a substrate by the particle adhesion force that exerted an adhesion torque on the particles. The acoustic pressure torque that was generated by an acoustic field cannot compete with the adhesion torque, and thus contributed little to the removal of micro and sub-micrometer-sized particles. With the introduction of micro-bubbles to the near field of the particles, it was possible to break the particle-substrate bonding through the bubble oscillation process. On the one hand, particles sitting within the bubble oscillation range can be forced to move off the substrate by the interface sweeping torque. On the other hand, particles located outside the bubble oscillation range were possible to be removed by the dynamic pressure torque. Previous studies, however, only considered the dynamic pressure torque that was generated by spherical oscillation at a large pressure amplitude. In this chapter, it was shown that it was the non-spherical oscillation rather than the spherical one that contributed to the cleaning of particles at a moderate pressure amplitude. The dynamic pressure torque that resulted from non-spherical oscillation was sufficiently strong to outweigh the adhesion torque within short distances. However, the spherical oscillation contributed little to the cleaning process. These estimations are linear approximations of the particle detachment, and provide a

qualitative insight into the ultrasonic cleaning process at a moderate pressure amplitude. An improved experimental rig, which is able to measure the microstreaming around the particles and the particle-substrate bonding force at the nanometer scale, is needed to be developed in the future to gain quantitative results.

Chapter 8

Conclusions

8.1 Thesis review

This thesis investigated the mechanism underlying ultrasonic cleaning using microbubbles. It was hypothesised that oscillating bubbles can cause cleaning by disturbing the flow field in the vicinity of contamination particles. Although the macroscopic cleaning effect has been reported, the bubble-particle interaction at the microscopic has not yet been fully understood. Moreover, in real life applications, bubbles are required to be transported onto the target surface. However, the detailed mechanism of bubble translation in a complicated multi-bubble environment is still unknown. Therefore, in this thesis, the investigation of ultrasonic cleaning was carried out in two steps: first the bubble transportation under various conditions was studied, and then the bubble behavior near a surface was explored in order to establish the relationship between the bubble induced cleaning forces and particle adhesion forces.

The dynamics of a bubble within an acoustic standing wave field were explored numerically and experimentally. The translation and oscillation of a bubble were derived based on the Lagrangian formulism. The external forces exerted on the bubble were analyzed for a bubble translating in a bulk medium and a multi-bubble environment respectively. The predicted bubble trajectories in the sound field were verified by the optical observations with a high speed camera system. Furthermore,

the bubble oscillation near a surface and the corresponding microstreaming were studied. The dominating factors which can influence the bubble oscillation mode were found. The shift of bubble oscillation modes were explained by the change of pressure threshold of non-spherical oscillation modes when a bubble is attached to a wall. The microstreaming around an oscillating bubble on a wall was explored with the PIV, and its formation was modelled based on the vorticity equation. Meanwhile, the feasibility of using the proposed system in real life ultrasonic cleaning applications was verified based on the experimental results of removing micrometer-sized particles from sample glass surfaces. The influence of both the spherical and non-spherical oscillation modes on the cleaning effect was explained based on a linear torque balance model.

Chapter 2 presented the design and construction of a multi-layered resonator for bubble motion control. The test cell consists of a transducer, a liquid medium and a glass backing plate. The acoustic field within the liquid was successfully modelled using the 1D model so that the transducer impedance as well as the pressure distribution within the whole assembly could be predicted. While this type of device is commonly employed in particle and cell manipulation studies but rarely for bubble manipulation investigations.

Chapter 3 revisited the theory background of single bubble and multi-bubble translation in an acoustic standing wave field. The translation and oscillation equations were derived from the Lagrangian formulism. The influence of a wall on the bubble translation was discussed.

In chapter 4, the mechanism of single bubble transportation was shown. Bubble radial oscillation was simulated by a modified Keller-Miksis equation and bubble translational motion was derived from an equation obtained by applying Newton's second law to a bubble in a liquid medium. The bubble trajectories were recorded by a high speed camera system. The influence of pressure amplitude and bubble size on the single bubble translation was explored.

Chapter 5 discussed the mechanism of bubble translation in a multi-bubble environment. An improved test rig was designed to study the multi-bubble transportation in a sound field. A theoretical model was established to explain the multi-bubble

translation by expressing the balance between Bjerknes forces and hydrodynamic forces on a bubble in a liquid medium. The bubble translations were observed with the high speed camera system and were compared with the theoretical predictions. The translational behaviors of bubbles of different sizes were examined. The influence of bubble-bubble interactions on the multi-bubble translation was studied.

Chapter 6 focused on the bubble behavior near a surface. The spherical and non-spherical bubble oscillation modes were observed with the high speed camera system. Several factors, including pressure amplitude, driving frequency, bubble size, boundary conditions, and neighboring bubbles, can all influence the bubble oscillation modes near a surface. Moreover, the microstreaming around an oscillating bubble was revealed with the PIV. Analytical solutions based on the modified Navier-Stokes equation were used to compare with the experimental results.

Chapter 7 demonstrated the feasibility of using the test rig for ultrasonic cleaning, and explored the possible mechanism of particle removal based on a linear torque balance model. The removal of silicon dioxide particles from sample glass surfaces was studied experimentally using a microscope. The relationship between the bubble-bubble interactions on the surfaces and its impact on the cleaning process was demonstrated. The cleaning mechanism was investigated by analyzing the relationship between different torques exerted on the micro and sub-micrometer-sized particles. The possible cleaning forces that were generated by the acoustic field and micro-bubbles were identified, and their relationship with the particle adhesion force was illustrated.

8.2 Main findings of this thesis

8.2.1 Single bubble translation

The single bubble translation was studied with a multi-layered resonator. The sound field was successfully predicted by a 1D model. The outputs of the 1D model included impedance of the stack and pressure distribution in the layered structure.

It was found that the motion of a single bubble was controlled by the primary

Bjerknes force from the sound field, the buoyancy force from the surrounding liquid, and the drag forces due to the liquid viscosity. For a single bubble, its translation can be influenced by the external pressure amplitude and its initial size. Bubbles larger than their resonance sizes were pushed towards the pressure node. Increasing the input pressure amplitude and decreasing the bubble size can force the bubbles to move towards the target at faster speeds, seen in the experiment by their arrivals at the reflector at lower heights. Bubbles smaller than their resonance size, on the other hand, were forced to move towards the pressure anti-node instead. The small bubbles were less sensitive to the changes of pressure amplitude and bubble size. All of these observed single bubble translations were in good agreement with the theoretical predictions.

8.2.2 Multi-bubble translation

The collective bubble dynamics near a surface in a weak acoustic standing wave field was investigated. The multi-bubble translation was achieved by using an improved multi-layered resonator which created an uniform one-dimensional acoustic standing wave field in a water layer. The bubble motion was calculated by a model that takes the boundary conditions and neighboring bubbles into account. The influence of several acoustic and hydrodynamic forces on the bubble translation was explored.

It was found that the bubble translation near a surface in a multi-bubble environment was mainly controlled by the primary Bjerknes force imposed by the acoustic field, secondary Bjerknes forces introduced by a surface and neighboring bubbles, and buoyancy force from the surrounding liquid. The primary Bjerknes force dominated the bubble translation when the bubble was far away from the surface and was outweighed by the secondary Bjerknes force from the boundary when the bubble was approaching the surface. Moreover, a strong secondary Bjerknes force generated by a neighboring bubble was noticed in the experiment. The bubble-bubble interaction forced nearby bubbles to move on trajectories towards the target bubble instead of the positions that they would have moved to in the absence of the target bubble. It was also seen from a parametric study that increasing the pressure amplitude can enhance the interaction between two bubbles and force bubbles to move at a faster speed. The secondary Bjerknes force between two bubbles can shift from an

attractive one when two bubbles oscillate in phase to a repulsive one when their oscillations are out of phase. All of these experimental results were in good agreement with the presented theory.

8.2.3 Bubble oscillation modes and microstreaming

The bubble behavior near a surface and the microstreaming was investigated theoretically and experimentally. It was noticed that several factors, including the driving frequency, external pressure amplitude, bubble size, boundary conditions and neighboring bubbles, worked together to decide the bubble oscillation modes. At a certain pressure amplitude, a bubble can maintain its spherical shape when its size was below a threshold, while the non-spherical modes can be excited for a bubble of larger size. Increasing the external pressure amplitude for a given size of bubble can also trigger the occurrence of non-spherical surface shape. Moreover, a nearby wall lowered the pressure threshold of non-spherical modes and enhanced the excitation of asymmetric surface pulsation. The neighboring wall can severely deform the bubble shape at the bubble-wall contact area at a large pressure amplitude which in turn promoted the bubble's non-spherical surface oscillation. The observed transitions between different bubble oscillation modes showed good agreement with the theoretical predictions.

Different oscillation modes could trigger different microstreaming around a bubble at a moderate pressure amplitude. Microstreaming due to the non-spherical modes decayed at a much faster rate with distance from the bubble than the spherical one, and thus contributed much less to the observed far-field microstreaming. The non-spherical mode would take more effect in the near field of the bubble. However, this effect is so localised that microstreaming due to non-spherical bubble oscillations could not be measured with the constructed test rig.

8.2.4 Ultrasonic cleaning mechanism

The mechanism underlying the ultrasonic cleaning using micro-bubbles was explored theoretically by analyzing the relationship between the different torques exerted on

micro and sub-micrometer-sized particles. From the simulation result, it was found that the acoustic pressure gradient torque that was generated by an acoustic standing wave field could not move micro and sub-micrometer-sized particles on a flat substrate. With the introduction of acoustically-driven bubbles, particles sitting within the bubble oscillation range could be cleaned by the interface sweeping torque. For particles located outside the oscillation range (bubble wall displacement), the dynamic pressure gradient torque that arose from the microstreaming could be responsible for the particle detachment. Previous theory, however, only considered the linear spherical bubble oscillation induced dynamic torque at a large pressure amplitude, which is not sufficient to explain particle removal. It was shown in this thesis that at a moderate pressure amplitude, the non-spherical bubble oscillation could potentially be responsible for the particle removal process in the vicinity of a micro-bubble. This provides a qualitatively insight into the mechanism of ultrasonic cleaning at moderate pressure amplitudes. The measurement of the microstreaming around the particles and the particle-substrate bonding force at the nanometer scale requires improved test equipment to be developed in the future.

8.3 Suggestions for future work

In the future, it would be possible to extend the study of bubble dynamics control in two directions: one is to investigate the particle removal mechanism at the nanometer scale, and the second one is to improve the performance of the acoustic standing wave field.

As suggested by the outcomes of this thesis, it is the non-spherical oscillation rather than the spherical oscillation that could be responsible for the cleaning of micro and sub-micrometer-sized particles. However, due to the limitation of the present optical observation technique, detailed analysis of the particle movement around oscillating bubbles at the nanometer scale has not yet been accomplished. Recently, Total Internal Reflection Fluorescence (TIRF) microscopy was reported to be able to visualize the nanobubble behavior on a surface [166]. The sharp contrast images obtained by TIRF is preferable in the study of particle removal. By adjusting the focus zone on the area in the vicinity of a surface, it might be possible to

observe the interaction between contamination particles and nearby flow motion at the nanometer scale. Moreover, it could also be possible to explore the cleaning of particles bonded with various adhesion forces on a substrate with the current test rig. This is important in quantifying the cleaning efficiency of different particles in future industrial applications.

The sound field presented in this thesis was designed as a one-dimensional one, which was uniformly distributed in the other directions in space. However, in real life ultrasonic cleaning processes, a multi-dimensional sound field is more preferable because the bubble translation is a three dimensional effect rather than a pure one dimensional one. The bubble-bubble interaction is important in controlling the bubble motion on a surface which in turn would influence the cleaning efficiency. Random bubble motion on a surface is a potential issue for the cleaning process, particularly for large scale operation. Ideally, bubbles are supposed to oscillate locally and disturb the flow motion in the near field of the surface. The accumulation of bubbles within an area would decrease the cleaning efficiency. Therefore, it would be necessary to create a sound field distributed with a certain pattern on a surface in order to effectively excite bubble oscillations, and meanwhile decrease the possibility of bubble coalescence. The design of transducers that enable excitation of these complicated sound fields for specific applications would be an interesting field for future work.

Appendix

Microstreaming

In an incompressible flow, the governing equation of the liquid velocity is governed by the Navier–Stokes equation [136]:

$$\frac{\partial u}{\partial t} + u\nabla u = \frac{1}{\rho}\left[-\nabla P + \eta\nabla^2 u + F\right] \tag{A-1}$$

where P is the pressure, and F is the sum of external forces.

Taking the curl of the Navier–Stokes equation on both sides eliminates the pressure component. The liquid velocity can be replaced by the Stokes streaming function ψ which is related to the radial and tangential components of the liquid velocity [136]:

$$\begin{aligned} u_r &= \frac{1}{r^2 sin\theta}\frac{\partial \psi}{\partial \theta} = -\frac{1}{r^2}\frac{\partial \psi}{\partial \nu} \\ u_\theta &= -\frac{1}{r sin\theta}\frac{\partial \psi}{\partial r} = -\frac{1}{r\sqrt{(1-\nu^2)}}\frac{\partial \psi}{\partial r} \end{aligned} \tag{A-2}$$

where $\nu = cos\theta$.

The Navier–Stokes equation is now converted to the vorticity equation in the form of streaming function ψ [167]:

$$\frac{\partial \Omega}{\partial t} + \frac{1}{r^2}\left[\frac{\partial(\psi,\Omega)}{\partial(r,\nu)} + 2\Omega\zeta\psi\right] = \eta D^2\Omega \tag{A-3}$$

$$\zeta \equiv \frac{\nu}{1-\nu^2}\frac{\partial}{\partial r} + \frac{1}{r}\frac{\partial}{\partial \nu} \tag{A-4}$$

where Ω is the vorticity of the flow defined by a linear operator D^2:

$$\Omega = -D^2\psi \tag{A-5}$$

$$D^2 \equiv \frac{\partial^2}{\partial^2 r^2} + \frac{1-\nu^2}{r^2}\frac{\partial^2}{\partial \nu} \tag{A-6}$$

The vorticity Eq.A-3 only contains the variable ψ and is the basis of the following flow dynamic analysis. Ideally, a numerical simulation of Eq.A-3 will characterize the complete details of the microstreaming. Such an analysis, however, consumes a considerable amount of computing time. Alternatively, analytical solutions up to the second order term have been verified to be suitable to quantify the microstreaming behavior at a low pressure amplitude in a bulk medium [108] and near a boundary [120]. Thus, the derivations of analytical solutions under different conditions are given as follows.

To obtain the analytical solution of Eq.A-3, the streaming function is expanded in a form of powers series as [108]:

$$\psi = \epsilon\psi_{01} + \epsilon'\psi_{10} + \epsilon^2\psi_{20} + \epsilon\epsilon'\psi_{11} + \epsilon'\psi_{02} + \cdots \tag{A-7}$$

where ϵ' and ϵ are the amplitudes of the translational streaming ψ_{n0} and radial streaming ψ_{0n} respectively. ψ_{11} is the streaming generated by the coupled bubble translation and oscillation.

The ψ given by Eq.A-3 is the Eulerian streaming function. The real flow motion needs to be represented by the Lagrangian streaming function Ψ which is the sum of the Eulerian streaming function and the Stokes drift ψ_s [108]

$$\Psi = \bar{\psi} + \psi_s$$

$$\psi_s = \frac{1}{r^2}\overline{\int \frac{\partial\psi}{\partial r}dt\frac{\partial\psi}{\partial\nu}} \tag{A-8}$$

where the over bar denotes the time average.

Besides Eq.A-7-A-8, the boundary conditions for Eq.A-3 are still unknown. The next step, thus, is to apply various boundary conditions on the vorticity equation to obtain the analytical solutions.

Microstreaming from a spherical oscillation

The analysis of the streaming function is accomplished by applying different boundary conditions to Eq.A-3 - A-8. For a spherical pulsation in a bulk medium, the bubble surface can be represented by [108]:

$$R(t) = R_0 - iR_0\epsilon exp(i(\omega t + \phi)) \tag{A-9}$$

where ϕ is the pulsation phase.

When a bubble travels in a liquid medium, the liquid velocity must be equal to the bubble wall displacement in the radial direction and the tangential liquid velocity vanishes. The boundary conditions in the radial and tangential directions are [108]:

$$\frac{R^2}{r^2} = -\frac{1}{r^2}\frac{\partial\psi_{01}}{\partial\nu}$$

$$-\frac{\partial^2\psi}{\partial r^2} + \frac{2}{r}\frac{\partial\psi}{\partial r} = 0 \tag{A-10}$$

By equating the bubble wall velocity and the liquid velocity, ψ_{01} is found by:

$$\psi_{01} = -\nu exp(i(\omega t + \phi)) \tag{A-11}$$

It is clearly shown that both $D^2\bar{\psi_{01}}$ and $\partial\psi_{01}/\partial r$ vanish.

ψ_{10} is given by applying the boundary condition Eq.A-10:

$$\psi_{10} = [\frac{1}{2}(r^2 - \frac{1}{r}) + \frac{B}{\alpha^2 r} + \frac{C}{\alpha^2}(1 + \frac{1}{\alpha r})exp(-\alpha(r-1))](1-\nu^2)exp(i\omega t) \tag{A-12}$$

where B and C are constants:

$$B = -\frac{3(1+1/\alpha)}{1+3/\alpha}, C = \frac{3}{1+3/\alpha} \tag{A-13}$$

Taking the mean values of Eq.A-3 and substituting ψ_{01} and ψ_{10}, the coupled streaming function ψ_{11} is shown by:

$$r^2 \eta D^4 \bar{\psi}_{11} = \overline{\frac{\partial(\psi_{01}, D^2\psi_{10})}{\partial(r,\nu)}} + \overline{2\zeta\psi_{01}D^2\psi_{10}} \tag{A-14}$$

With the boundary condition Eq.A-10, the lowest order form of the Lagrangrian microstreaming is [108]:

$$\bar{\psi}_{11} = -\frac{1}{2}iexp(-i\phi)[(r + \frac{1}{2r}) + 3(1-i)\delta(r - \frac{1}{r})](1-\nu^2) \tag{A-15}$$

where $\delta = \sqrt{2\eta/\omega}$.

The Stokes drift of the spherical pulsation is [108]:

$$\psi_{s11} = \frac{3}{4}exp(-i\phi)(i + \delta^2 - 2i\delta\eta + 4i\delta^2\eta^2) - [(1+i)\delta - 2\delta^2 - 2(1+i)\delta^2\eta]e(-(1+i)\eta)(1-\nu^2) \tag{A-16}$$

The Lagrangrian streaming function is the sum of the mean Eulerian streaming and the Stokes drift. The lowest order form of the Lagrangrian is [108]:

$$\bar{\Psi}_{11} = sin\phi(-\frac{r}{2} + \frac{1}{4r} + \frac{1}{4r^4})(1-\nu^2) \tag{A-17}$$

In dimensional terms, the microstreaming takes the form of [120]

$$\bar{\Psi}_{11} = \frac{\epsilon^2}{4} R_0^3 \omega sin\phi (-2\frac{r}{R_0} + \frac{R_0}{r} + \frac{R_0^4}{r^4})(1-\nu^2) \tag{A-18}$$

It needs to be pointed out that in many applications, a bubble normally oscillates near a surface. Thus, the bulk medium streaming function needs to be expanded to include the boundary effects. Suppose the surface is rigid, the influence from the boundary on the microstreaming can be treated by adding imaginary singularities on the other side of the wall . The sum of the original streaming function and the imaginary streaming functions creates a new streaming function $\bar{\Psi}_{11w}$ which fulfills the new rigid boundary condition [120].

$$\bar{\Psi}_{11w} = -3\epsilon^2 R_0^4 \omega sin\phi \frac{1}{r} \nu^2 (1-\nu^2) \tag{A-19}$$

The flow velocity can then be calculated by substituting Eq.A-19 into Eq.A-2

$$u_{r11w} = \frac{6\epsilon^2 R_0^4 \omega sin\phi}{r^3} [\nu^3 - \nu(1-\nu^2)]$$

$$u_{\theta 11w} = -\frac{3\epsilon^2 R_0^4 \omega sin\phi}{r^3} \nu^2 \sqrt{1-\nu^2} \tag{A-20}$$

Microstreaming from a non-spherical oscillation

The microstreaming around a bubble with a non-spherical shape is derived following the same procedure as for the spherical case.

The time varying bubble surface is defined by:

$$R(t) = R_0 + \epsilon \tag{A-21}$$

The kinematic boundary condition on the bubble surface is [152]:

$$u_r - \frac{u_\theta}{r}\frac{\partial \epsilon}{\partial \theta} = -\frac{1}{r^2}\left(\frac{\partial \psi}{\partial \nu} + \frac{\partial \epsilon}{\partial \nu}\frac{\partial \psi}{\partial r}\right) \tag{A-22}$$

The dynamic boundary conditions are [152]:

$$\begin{aligned} p_0\left(\frac{R_0}{r}\right)^{3\gamma} - \sigma(\nabla, \mathbf{n}) =& P - 2\eta_d\left[r^2 + (1-\nu^2)\left(\frac{\partial \epsilon}{\partial \nu}\right)^2\right]^{-1}\{-\frac{\partial^2 \psi}{\partial r \partial \nu} + \\ & \frac{2}{r}\frac{\partial \psi}{\partial \nu} + \left(\frac{\partial \epsilon}{\partial \nu}\right)\left[-\frac{\partial^2 \psi}{\partial r^2} + \frac{1-\nu^2}{r^2}\frac{\partial^2 \psi}{\partial \nu^2} + \frac{2}{r}\frac{\partial \psi}{\partial r}\right] + \\ & \frac{1}{r^2}\left(\frac{\partial \epsilon}{\partial \nu}\right)^2\left[(1-\nu^2)\frac{\partial^2 \psi}{\partial r \partial \nu} + \nu\frac{\partial \psi}{\partial r} - \frac{\sqrt{1-\nu^2}}{r}\frac{\partial \psi}{\partial \nu}\right]\} \end{aligned} \tag{A-23}$$

$$\begin{aligned} & \left[1 - \frac{1-\nu^2}{r^2}\left(\frac{\partial \epsilon}{\partial \nu}\right)^2\right]\left[\frac{\partial^2 \psi}{\partial r^2} - \frac{1-\nu^2}{r^2}\frac{\partial^2 \psi}{\partial \nu^2} - \frac{2}{r}\frac{\partial \psi}{\partial r}\right] + \\ & \frac{2}{r^2}\frac{\partial \epsilon}{\partial \nu}\left[-2(1-\nu^2)\frac{\partial^2 \psi}{\partial r \partial \nu} - \nu\frac{\partial \psi}{\partial r} + \frac{3(1-\nu^2)}{r}\frac{\partial \psi}{\partial \nu}\right] = 0 \end{aligned} \tag{A-24}$$

where η_d is the dynamic viscosity, $\mathbf{n}$ is the unit vector normal to the bubble surface

$$\mathbf{n} = \left[e_r - \frac{1}{r}\frac{\partial \epsilon}{\partial \theta}e_\theta\right]\sqrt{1 + \frac{1}{r^2}\left(\frac{\partial \epsilon}{\partial \theta}\right)^2} \tag{A-25}$$

where e_r and e_θ are the unit vector in the radial and tangential directions respectively.

Substituting the streaming power series into Eq.A-23 and A-24, the lowest order Lagrangian streaming function for non-spherical surface oscillation is [152]:

$$\begin{aligned} \psi_{01} =& \left(-\frac{i\omega}{2}\right)\epsilon_{1n}\sqrt{\frac{2n+1}{4\pi}}\frac{a^2}{n(n+1)}\{\left(\frac{a}{r}\right)^n + 2n(n+2)\left[1 - i\frac{n(n+1)}{2\alpha r a}(r-a) - \right. \\ & \left.\frac{2}{\alpha a}\right]\frac{exp(i\alpha\epsilon)}{\alpha^2 a^2}\}\sqrt{1-\nu^2}P_n^1\nu \end{aligned} \tag{A-26}$$

where ϵ_{1n} is the amplitude of the nth mode.

Using Eq.A-8, the Stokes drift is found by:

$$\begin{aligned}\psi_s =&\frac{\omega}{2}\epsilon_{1n}^2 R_0 \frac{2n+1}{4\pi}\frac{n+2}{n+1}exp(-\frac{\eta}{\sqrt{2}})\{\beta cos(\frac{\eta}{\sqrt{2}}+\frac{\pi}{4})(1-\beta\eta(n+2))+\\ &\beta^2(n+3)sin(\frac{\eta}{\sqrt{2}})\}(1-\nu^2)P_n\end{aligned} \tag{A-27}$$

The lowest order Lagrangian streaming function for non-spherical surface oscillation is [152]:

$$\begin{aligned}\psi_{01}^n &= -\frac{i\omega}{2}\epsilon_{1n}\sqrt{\frac{2n+1}{4\pi}}\frac{R_0^2}{n(n+1)}M\sqrt{1-\nu^2}P_n^1(\nu)\\ M &= (\frac{R_0}{r})^n + \frac{2n(n+2)}{(\alpha R_0)^2}[1-i\frac{n(n+1)}{2\alpha r R_0}(r-R_0)-\frac{2}{\alpha R_0}]e^{i\alpha(r-R_0)}\end{aligned} \tag{A-28}$$

Therefore, the Lagrangian steaming is given by:

$$\bar{\Psi}_{11}^n = \frac{\omega\epsilon_{1n}^2 R_0}{2\pi}\frac{2n+1}{4\pi}\frac{(n+2)(n+3)}{2(n+1)(4n+3)}[-(\frac{R_0}{r})^{(2n-1)}+(\frac{R_0}{r})^{(2n+1)}]cos(2n+1)\theta \tag{A-29}$$

where ϵ_{1n} is the amplitude of the nth mode.

For a bubble oscillating near a surface, the streaming function also needs to be expanded to include the influence from the wall. By introducing imaginary singularities on the other side of the wall, the new Lagrangian streaming function $\bar{\Psi}_{11w}^n$ takes the form of:

$$\bar{\Psi}_{11w}^n = \frac{\omega\epsilon_{1n}^2 R_0^{2n}}{2\pi}\frac{2n+1}{4\pi}\frac{(n+2)(n+3)}{2(n+1)(4n+3)}(4n^2+2n-2)\frac{1}{r^{2n-1}}cos(2n+1)\theta sin^2\theta \tag{A-30}$$

Similar to the spherical case, the flow velocity can be obtained by:

$$u^n_{r11w} = \frac{\omega\epsilon_{1n}^2 R_0^{2n}}{2\pi}\frac{2n+1}{4\pi}\frac{(n+2)(n+3)}{2(n+1)(4n+3)}(4n^2+2n-2) \\ \frac{1}{r^{2n+1}}[2cos(2n+1)\theta cos\theta - (2n+1)sin(2n+1)\theta sin\theta] \tag{A-31}$$

$$u^n_{\theta 11w} = \frac{\omega\epsilon_{1n}^2 R_0^{2n}}{2\pi}\frac{2n+1}{4\pi}\frac{(2n-1)(n+2)(n+3)}{2(n+1)(4n+3)}(4n^2+2n-2)\frac{1}{r^{2n+1}}cos(2n+1)\theta sin\theta \tag{A-32}$$

References

[1] S. Wolf and R.N. Tauber. *Silicon processing for the VLSI era process technology.* Lattice Press, Sunset Beach, CA, 1986.

[2] E. Maisonhaute, C. Prado, P.C. White, and R.G. Compton. Surface acoustic cavitation understood via nanosecond electrochemistry. Part III: Shear stress in ultrasonic cleaning. *Ultrasonics Sonochemistry*, 9(6):297–303, 2002.

[3] G.K. Batchelor. *An introduction to fluid dynamics.* Cambridge University Press, 1970.

[4] D. Zhuang and J.H. Edgar. Wet etching of gan, aln, and sic: a review. *Materials Science and Engineering: R: Reports*, 48(1):1–46, 2005.

[5] W. Kim, K. Park, J. Oh, J. Choi, and H.Y. Kim. Visualization and minimization of disruptive bubble behavior in ultrasonic field. *Ultrasonics*, 8:798–802, 2010.

[6] A.C. Tam, H.K. Park, and C.P. Grigoropoulos. Laser cleaning of surface contaminants. *Applied surface science*, 127:721–725, 1998.

[7] H.K. Park, C.P. Grigoropoulos, W.P. Leung, and A.C. Tam. A practical excimer laser-based cleaning tool for removal of surface contaminants. *IEEE Transactions on Components, Packaging, and Manufacturing Technology, Part A*, 17(4):631–643, 1994.

[8] F. Lang, M. Mosbacher, and P. Leiderer. Near field induced defects and influence of the liquid layer thickness in steam laser cleaning of silicon wafers. *Applied Physics A: Materials Science and Processing*, 77(1):117–123, 2003.

[9] A.C. Tam, W.P. Leung, W. Zapka, and W. Ziemlich. Laser-cleaning techniques for removal of surface particulates. *Journal of Applied Physics*, 71(7):3515–3523, 1992.

[10] W. Zapka, W. Ziemlich, and A.C. Tam. Efficient pulsed laser removal of 0.2 μm sized particles from a solid surface. *Applied physics letters*, 58(20):2217–2219, 1991.

[11] J.M. Lee and K.G. Watkins. Removal of small particles on silicon wafer by laser-induced airborne plasma shock waves. *Journal of Applied Physics*, 89:6496–6500, 2001.

[12] M. Mosbacher, H.J. Münzer, J. Zimmermann, J. Solis, J. Boneberg, and P. Leiderer. Optical field enhancement effects in laser-assisted particle removal. *Applied Physics A: Materials Science and Processing*, 72(1):41–44, 2001.

[13] G. Vereecke, R. Vos, M.M. Heyns, M. Schmidt, F. Holsteyns, M. Baeyens, S. Gomme, J. Snow, P.W. Mertens, and V. Coenen. Influence of hardware and chemistry on the removal of nano-particles in a megasonic cleaning tank. *Solid State Phenomena*, 92:143–146, 2003.

[14] G. Vereecke, F. Holsteyns, S. Arnauts, S. Beckx, P. Jaenen, K. Kenis, M. Lismont, M. Lux, R. Vos, and J. Snow. Evaluation of megasonic cleaning for sub-90nm technologies. *Solid State Phenomena*, 103:141–146, 2005.

[15] C.D. Ohl, M. Arora, R. Dijkink, V. Janve, and D. Lohse. Surface cleaning from laser-induced cavitation bubbles. *Applied Physics Letters*, 89(7):074102, 2006.

[16] W.D. Song, M.H. Hong, B. Lukyanchuk, and T.C. Chong. Laser-induced cavitation bubbles for cleaning of solid surfaces. *Journal of applied physics*, 95:2952–2956, 2004.

[17] G.W. Gale and A.A. Busnaina. Removal of particulate contaminants using ultrasonics and megasonics: a review. *Particulate science and Technology*, 13(3-4):197–211, 1995.

[18] A. Busnaina and I. Kashkoush. The effect of time, temperature and particle size on submicron particle removal using ultrasonic cleaning. *Chemical Engineering Communications*, 125(1):47–61, 1993.

[19] W. Glenn and A.B. Ahmed. Roles of cavitation and acoustic streaming in megasonic cleaning. *Particulate science and technology*, 17(3):229–238, 1999.

[20] A.A. Busnaina and F. Dai. The removal of submicron particles in liquid-based cleaning. *The Journal of Adhesion*, 67(1-4):181–193, 1998.

[21] M. Hauptmann, S. Brems, E. Camerotto, A. Zijlstra, G. Doumen, T. Bearda, P.W. Mertens, and W. Lauriks. Influence of gasification on the performance of a 1 MHz nozzle system in megasonic cleaning. *Microelectronic Engineering*, 87(5-8):1512–1515, 2010.

[22] F. Holsteyns, T. Janssens, S. Arnauts, W. Van der Putte, V. Minsier, J. Brunner, J. Straka, and P.W. Mertens. Ex situ bubble generation, enhancing the particle removal rate for single wafer megasonic cleaning processes. *Solid State Phenomena*, 134:201–204, 2008.

[23] A. Mayer and S. Shwartzman. Megasonic cleaning: A new cleaning and drying system for use in semiconductor processing. *Journal of Electronic Materials*, 8(6):855–864, 1979.

[24] W. Kim, T.H. Kim, J. Choi, and H.Y. Kim. Mechanism of particle removal by megasonic waves. *Applied Physics Letters*, 94(8):081908, 2009.

[25] S.R. Gonzalez-Avila, X. Huang, P.A. Quinto-Su, T. Wu, and C.D. Ohl. Motion of micrometer sized spherical particles exposed to a transient radial flow: Attraction, repulsion, and rotation. *Physical Review Letters*, 107(7):74503, 2011.

[26] X. Xi, F. Yang, D. Chen, Y. Luo, D. Zhang, N. Gu, and J. Wu. A targeting drug-delivery model via interactions among cells and liposomes under ultrasonic excitation. *Physics in Medicine and Biology*, 53:3251–3265, 2008.

[27] M. Ward, J. Wu, and J.F. Chiu. Ultrasound-induced cell lysis and sonoporation enhanced by contrast agents. *The Journal of the Acoustical Society of America*, 105:2951–2957, 1999.

[28] S. Bao, B.D. Thrall, and D.L. Miller. Transfection of a reporter plasmid into cultured cells by sonoporation in vitro. *Ultrasound in medicine and biology*, 23(6):953–959, 1997.

[29] S. Bao, B.D. Thrall, R.A. Gies, and D.L. Miller. In vivo transfection of melanoma cells by lithotripter shock waves. *Cancer research*, 58(2):219–221, 1998.

[30] D.L. Miller, S. Bao, R.A. Gies, and B.D. Thrall. Ultrasonic enhancement of gene transfection in murine melanoma tumors. *Ultrasound in medicine and biology*, 25(9):1425–1430, 1999.

[31] D.L. Miller, S.V. Pislaru, and J.F. Greenleaf. Sonoporation: mechanical DNA delivery by ultrasonic cavitation. *Somatic cell and molecular genetics*, 27(1):115–134, 2002.

[32] M. Ward, J. Wu, and J.F. Chiu. Experimental study of the effects of Optison concentration on sonoporation in vitro. *Ultrasound in medicine and biology*, 26(7):1169–1175, 2000.

[33] P. Prentice, A. Cuschieri, K. Dholakia, M. Prausnitz, and P. Campbell. Membrane disruption by optically controlled microbubble cavitation. *Nature Physics*, 1(2):107–110, 2005.

[34] R.H. Liu, J. Yang, M.Z. Pindera, M. Athavale, and P. Grodzinski. Bubble-induced acoustic micromixing. *Lab Chip*, 2(3):151–157, 2002.

[35] D. Krefting, R. Mettin, and W. Lauterborn. High-speed observation of acoustic cavitation erosion in multibubble systems. *Ultrasonics Sonochemistry*, 11(3-4):119–123, 2004.

[36] A. Philipp and W. Lauterborn. Cavitation erosion by single laser-produced bubbles. *Journal of Fluid Mechanics*, 361(1):75–116, 1998.

[37] C.D. Ohl, T. Kurz, R. Geisler, O. Lindau, and W. Lauterborn. Bubble dynamics, shock waves and sonoluminescence. *Philosophical Transactions of the Royal Society of London. Series A: Mathematical, Physical and Engineering Sciences*, 357(1751):269–294, 1999.

[38] W. Lauterborn and W. Hentschel. Cavitation bubble dynamics studied by high speed photography and holography: part one. *Ultrasonics*, 23(6):260–268, 1985.

[39] O. Lindau and W. Lauterborn. Cinematographic observation of the collapse and rebound of a laser-produced cavitation bubble near a wall. *Journal of Fluid Mechanics*, 479(1):327–348, 2003.

[40] W. Lauterborn and C.D. Ohl. Cavitation bubble dynamics. *Ultrasonics Sonochemistry*, 4(2):65–75, 1997.

[41] L.V. King. On the acoustic radiation pressure on spheres. *Proceedings of the Royal Society of London. Series A: Mathematical and Physical Sciences*, 147(861):212–240, 1934.

[42] K. Yosioka, Y. Kawasima, and H. Hirano. Acoustic radiation pressure on bubbles and their logarithmic decrement. *Acustica*, 5(3):173–178, 1955.

[43] A. Eller. Force on a bubble in a standing acoustic wave. *The Journal of the Acoustical Society of America*, 43:170–171, 1968.

[44] L.A. Crum. Bjerknes forces on bubbles in a stationary sound field. *The Journal of the Acoustical Society of America*, 57:1363–1370, 1975.

[45] C.P. Lee and T.G. Wang. Acoustic radiation force on a bubble. *The Journal of the Acoustical Society of America*, 93:1637–1640, 1993.

[46] A.A. Doinikov. Acoustic radiation force on a bubble: Viscous and thermal effects. *The Journal of the Acoustical Society of America*, 103:143–147, 1998.

[47] N. Gaines. A magnetostriction oscillator producing intense audible sound and some effects obtained. *Journal of Applied Physics*, 3:209–229, 1932.

[48] M. Strasberg and T.B. Benjamin. Excitation of oscillations in the shape of pulsating gas bubbles; experimental work. *The Journal of the Acoustical Society of America*, 30:697–697, 1958.

[49] A. Eller and L.A. Crum. Instability of the motion of a pulsating bubble in a sound field. *The Journal of the Acoustical Society of America*, 47:762–767, 1970.

[50] C.C. Mei and X. Zhou. Parametric resonance of a spherical bubble. *Journal of Fluid Mechanics*, 229:29–50, 1991.

[51] Z.C. Feng and L.G. Leal. Translational instability of a bubble undergoing shape oscillations. *Physics of Fluids*, 7:1325–1336, 1995.

[52] A.A. Doinikov. Translational motion of a bubble undergoing shape oscillations. *Journal of Fluid Mechanics*, 501:1–24, 2004.

[53] I. Akhatov, R. Mettin, C.D. Ohl, U. Parlitz, and W. Lauterborn. Bjerknes force threshold for stable single bubble sonoluminescence. *Physical review E*, 55(3):3747–3750, 1997.

[54] T.J. Matula, S.M. Cordry, R.A. Roy, and L.A. Crum. Bjerknes force and bubble levitation under single-bubble sonoluminescence conditions. *The Journal of the Acoustical Society of America*, 102:1522–1527, 1997.

[55] D.L. Miller. Stable arrays of resonant bubbles in a 1-MHz standing-wave acoustic field. *The Journal of the Acoustical Society of America*, 62:12–19, 1977.

[56] S. Khanna, N.N. Amso, S.J. Paynter, and W.T. Coakley. Contrast agent bubble and erythrocyte behavior in a 1.5-MHz standing ultrasound wave. *Ultrasound in medicine and biology*, 29(10):1463–1470, 2003.

[57] L.A. Kuznetsova, S. Khanna, N.N. Amso, W.T. Coakley, and A.A. Doinikov. Cavitation bubble-driven cell and particle behavior in an ultrasound standing wave. *The Journal of the Acoustical Society of America*, 117:104–112, 2005.

[58] Y. Abe, M. Kawaji, and T. Watanabe. Study on the bubble motion control by ultrasonic wave. *Experimental Thermal and Fluid Science*, 26(6-7):817–826, 2002.

[59] T. Watanabe and Y. Kukita. Translational and radial motions of a bubble in an acoustic standing wave field. *Physics of Fluids A: Fluid Dynamics*, 5:2682–2688, 1993.

[60] A.A. Doinikov. Translational motion of a spherical bubble in an acoustic standing wave of high intensity. *Physics of Fluids*, 14:1420–1425, 2002.

[61] R. Mettin and A.A. Doinikov. Translational instability of a spherical bubble in a standing ultrasound wave. *Applied Acoustics*, 70(10):1330–1339, 2009.

[62] T. Barbat, N. Ashgriz, and C.S. Liu. Dynamics of two interacting bubbles in an acoustic field. *Journal of Fluid Mechanics*, 389(1):137–168, 1999.

[63] A.A. Doinikov and S.T. Zavtrak. On the mutual interaction of two gas bubbles in a sound field. *Physics of Fluids*, 7:1923–1930, 1995.

[64] R. Mettin, I. Akhatov, U. Parlitz, C.D. Ohl, and W. Lauterborn. Bjerknes forces between small cavitation bubbles in a strong acoustic field. *Physical review E*, 56(3):2924–2931, 1997.

[65] J.W.S. Rayleigh. *The theory of sound*. Dover, New York, 1945.

[66] M.S. Plesset. The dynamics of cavitation bubbles. *J. appl. Mech*, 16(3):227–282, 1949.

[67] F.R. Gilmore. The growth or collapse of a spherical bubble in a viscous compressible liquid. *California Institute of Technology , Pasadena, CA. (Unpublished)*, 1952.

[68] J.B. Keller and M. Miksis. Bubble oscillations of large amplitude. *The Journal of the Acoustical Society of America*, 68:628–633, 1980.

[69] R.G. Holt and L.A. Crum. Acoustically forced oscillations of air bubbles in water: Experimental results. *The Journal of the Acoustical Society of America*, 91:1924–1932, 1992.

[70] Y. Tian, J.A. Ketterling, and R.E. Apfel. Direct observation of microbubble oscillations. *The Journal of the Acoustical Society of America*, 100:3976–3978, 1996.

[71] R. Geisler. *Untersuchungen zur laserinduzierten Kavitation mit Nanosekunden-und Femtosekundenlasern*. Universität Göttingen, 2004.

[72] B. Gompf and R. Pecha. Mie scattering from a sonoluminescing bubble with high spatial and temporal resolution. *Physical Review E*, 61(5):5253–5256, 2000.

[73] T.J. Matula. Inertial cavitation and single–bubble sonoluminescence. *Philosophical Transactions of the Royal Society of London. Series A: Mathematical, Physical and Engineering Sciences*, 357(1751):225–249, 1999.

[74] M.S. Plesset and A. Prosperetti. Bubble dynamics and cavitation. *Annual Review of Fluid Mechanics*, 9(1):145–185, 1977.

[75] Z.C. Feng and L.G. Leal. Nonlinear bubble dynamics. *Annual review of fluid mechanics*, 29(1):201–243, 1997.

[76] W. Lauterborn and T. Kurz. Physics of bubble oscillations. *Reports on Progress in Physics*, 73:106501, 2010.

[77] M.S. Plesset. On the stability of fluid flows with spherical symmetry. *Journal of Applied Physics*, 25(1):96–98, 1954.

[78] A. Prosperetti. Viscous effects on perturbed spherical flows. *Quarterly of Applied Mathematics*, 34:339–352, 1977.

[79] A. Prosperetti and Y. Hao. Modelling of spherical gas bubble oscillations and sonoluminescence. *Philosophical Transactions of the Royal Society of London. Series A: Mathematical, Physical and Engineering Sciences*, 357(1751):203–223, 1999.

[80] Y. Hao and A. Prosperetti. The effect of viscosity on the spherical stability of oscillating gas bubbles. *Physics of Fluids*, 11:1309–1317, 1999.

[81] S. Hilgenfeldt, D. Lohse, and M. Brenner. Phase diagrams for sonoluminescing bubbles. *Physics of fluids*, 8:2808–2826, 1996.

[82] D. Lohse, M.P. Brenner, T.F. Dupont, S. Hilgenfeldt, and B. Johnston. Sonoluminescing air bubbles rectify argon. *Physical review letters*, 78(7):1359–1362, 1997.

[83] M.P. Brenner, D. Lohse, and TF Dupont. Bubble shape oscillations and the onset of sonoluminescence. *Physical review letters*, 75(5):954–957, 1995.

[84] M.P. Brenner, S. Hilgenfeldt, and D. Lohse. Single bubble sonoluminescence. *Reviews of modern physics*, 74(2):425–484, 2002.

[85] M.S. Longuet-Higgins. Monopole emission of sound by asymmetric bubble oscillations. part 1. normal modes. *Journal of Fluid Mechanics*, 201:525–541, 1989.

[86] M.S. Longuet-Higgins. Monopole emission of sound by asymmetric bubble oscillations. part 2. an initial-value problem. *Journal of Fluid Mechanics*, 201(1):543–565, 1989.

[87] S.J. Shaw. Translation and oscillation of a bubble under axisymmetric deformation. *Physics of fluids*, 18:072104, 2006.

[88] S. Zhao, K.W. Ferrara, and P.A. Dayton. Asymmetric oscillation of adherent targeted ultrasound contrast agents. *Applied physics letters*, 87:134103, 2005.

[89] H.J. Vos, B. Dollet, JG Bosch, M. Versluis, and N. de Jong. Nonspherical vibrations of microbubbles in contact with a wall–a pilot study at low mechanical index. *Ultrasound in medicine and biology*, 34(4):685–688, 2008.

[90] H.J. Vos, B. Dollet, M. Versluis, and N. de Jong. Nonspherical shape oscillations of coated microbubbles in contact with a wall. *Ultrasound in Medicine and Biology*, 37(6):935–948, 2011.

[91] M. Versluis, D.E. Goertz, P. Palanchon, I.L. Heitman, S.M. van der Meer, B. Dollet, N. de Jong, and D. Lohse. Microbubble shape oscillations excited through ultrasonic parametric driving. *Physical Review E*, 82(2):026321, 2010.

[92] M. Overvelde, V. Garbin, J. Sijl, B. Dollet, N. de Jong, D. Lohse, and M. Versluis. Nonlinear shell behavior of phospholipid-coated microbubbles. *Ultrasound in medicine and biology*, 36(12):2080–2092, 2010.

[93] M. Overvelde, V. Garbin, B. Dollet, N. de Jong, D. Lohse, and M. Versluis. Dynamics of coated microbubbles adherent to a wall. *Ultrasound in medicine and biology*, 37(9):1500–1508, 2011.

[94] V.G Levich. *Physicochemical hydrodynamics*. Prentice-Hall Englewood Cliffs, NJ, 1962.

[95] D.W. Moore. The velocity of rise of distorted gas bubbles in a liquid of small viscosity. *Journal of Fluid Mechanics*, 23(4):749–766, 1965.

[96] D.W. Moore. The boundary layer on a spherical gas bubble. *Journal of Fluid Mechanics*, 16(pt 2):161–176, 1963.

[97] J. Happel and H. Brenner. *Low Reynolds number hydrodynamics: with special applications to particulate media*. Springer, 1983.

[98] J.W. Cleaver and B. Yates. Mechanism of detachment of colloidal particles from a flat substrate in a turbulent flow. *Journal of Colloid and Interface Science*, 44(3):464–474, 1973.

[99] M.E. O'Neill. A sphere in contact with a plane wall in a slow linear shear flow. *Chemical Engineering Science*, 23(11):1293–1298, 1968.

[100] L.M. Milne-Thompson. *Theorical hydrodynamics*. MacMillan, London, 1968.

[101] M.S. Longuet-Higgins. Mass transport in water waves. *Philosophical Transactions of the Royal Society of London. Series A: Mathematical and Physical Sciences*, 245(903):535–581, 1953.

[102] E. Yeager and F. Hovorka. Ultrasonic waves and electrochemistry. i. a survey of the electrochemical applications of ultrasonic waves. *The Journal of the Acoustical Society of America*, 25:443–455, 1953.

[103] S.A. Elder, J. Kolb, and W.L. Nyborg. Small-scale acoustic streaming effects in liquids. *The Journal of the Acoustical Society of America*, 26:933–933, 1954.

[104] N. Riley. On a sphere oscillating in a viscous fluid. *The Quarterly Journal of Mechanics and Applied Mathematics*, 19(4):461–472, 1966.

[105] N. Amin and N. Riley. Streaming from a sphere due to a pulsating source. *Journal of Fluid Mechanics*, 210(1):459–473, 1990.

[106] B.J. Davidson and N. Riley. Cavitation microstreaming. *Journal of Sound and Vibration*, 15(2):217–233, 1971.

[107] H. Zhao, S.S. Sadhal, and E.H. Trinh. Singular perturbation analysis of an acoustically levitated sphere: Flow about the velocity node. *The Journal of the Acoustical Society of America*, 106:589–595, 1999.

[108] M.S. Longuet-Higgins. Viscous streaming from an oscillating spherical bubble. *Proceedings of the Royal Society of London. Series A: Mathematical, Physical and Engineering Sciences*, 454(1970):725, 1998.

[109] J. Wu and G. Du. Streaming generated by a bubble in an ultrasound field. *Journal of the Acoustical Society of America*, 101:1899–1907, 1997.

[110] X. Liu and J. Wu. Acoustic microstreaming around an isolated encapsulated microbubble. *The Journal of the Acoustical Society of America*, 125:1319–1330, 2009.

[111] A.A. Doinikov and A. Bouakaz. Acoustic microstreaming around a gas bubble. *The Journal of the Acoustical Society of America*, 127:703, 2010.

[112] N. Riley. Steady streaming. *Annual review of fluid mechanics*, 33(1):43–65, 2001.

[113] M.J. Lighthill. Acoustic streaming. *Journal of Sound and Vibration*, 61(3):391–418, 1978.

[114] N. Riley. Oscillatory viscous flows. review and extension. *IMA Journal of Applied Mathematics*, 3(4):419–434, 1967.

[115] J. Kolb and W.L. Nyborg. Small-scale acoustic streaming in liquids. *The Journal of the Acoustical Society of America*, 28:1237, 1956.

[116] S.A. Elder. Cavitation microstreaming. *The Journal of the Acoustical Society of America*, 31:54, 1959.

[117] P. Tho, R. Manasseh, and A. Ooi. Cavitation microstreaming patterns in single and multiple bubble systems. *Journal of Fluid Mechanics*, 576:191–233, 2007.

[118] J. Collis, R. Manasseh, P. Liovic, P. Tho, A. Ooi, K. Petkovic-Duran, and Y. Zhu. Cavitation microstreaming and stress fields created by microbubbles. *Ultrasonics*, 50(2):273–279, 2010.

[119] D. Kröninger, K. Köhler, T. Kurz, and W. Lauterborn. Particle tracking velocimetry of the flow field around a collapsing cavitation bubble. *Experiments in fluids*, 48(3):395–408, 2010.

[120] P. Marmottant and S. Hilgenfeldt. Controlled vesicle deformation and lysis by single oscillating bubbles. *Nature*, 423(6936):153–156, 2003.

[121] P. Marmottant, S. van der Meer, M. Emmer, M. Versluis, N. de Jong, S. Hilgenfeldt, and D. Lohse. A model for large amplitude oscillations of coated bubbles accounting for buckling and rupture. *The Journal of the Acoustical Society of America*, 118:3499–3505, 2005.

[122] G. Gormley and J. Wu. Observation of acoustic streaming near albunex spheres. *The Journal of the Acoustical Society of America*, 104:3115–3118, 1998.

[123] N.R. Harris, M. Hill, S. Beeby, Y. Shen, N.M. White, J.J. Hawkes, and W.T. Coakley. A silicon microfluidic ultrasonic separator. *Sensors and Actuators B: Chemical*, 95(1-3):425–434, 2003.

[124] N. Harris, M. Hill, Y. Shen, R.J. Townsend, S. Beeby, and N. White. A dual frequency ultrasonic microengineered particle manipulator. *Ultrasonics*, 42(1-9):139–144, 2004.

[125] N.R. Harris, M. Hill, R. Townsend, N.M. White, and S.P. Beeby. Performance of a micro-engineered ultrasonic particle manipulator. *Sensors and Actuators B: Chemical*, 111:481–486, 2005.

[126] T. Lilliehorn, U. Simu, M. Nilsson, M. Almqvist, T. Stepinski, T. Laurell, J. Nilsson, and S. Johansson. Trapping of microparticles in the near field of an ultrasonic transducer. *Ultrasonics*, 43(5):293–303, 2005.

[127] S. Oberti, A. Neild, and J. Dual. Manipulation of micrometer sized particles within a micromachined fluidic device to form two-dimensional patterns using ultrasound. *The Journal of the Acoustical Society of America*, 121:778–785, 2007.

[128] T. Laurell, F. Petersson, and A. Nilsson. Chip integrated strategies for acoustic separation and manipulation of cells and particles. *Chemical Society Reviews*, 36(3):492–506, 2007.

[129] J.J. Hawkes, M.J. Long, W.T. Coakley, and M.B. McDonnell. Ultrasonic deposition of cells on a surface. *Biosensors and Bioelectronics*, 19(9):1021–1028, 2004.

[130] A. Haake, A. Neild, G. Radziwill, and J. Dual. Positioning, displacement, and localization of cells using ultrasonic forces. *Biotechnology and bioengineering*, 92(1):8–14, 2005.

[131] K.A.J. Borthwick, W.T. Coakley, M.B. McDonnell, H. Nowotny, E. Benes, and M. Groeschl. Development of a novel compact sonicator for cell disruption. *Journal of microbiological methods*, 60(2):207–216, 2005.

[132] P.D. Wilcox, R.S.C. Monkhouse, P. Cawley, M.J.S. Lowe, and B.A. Auld. Development of a computer model for an ultrasonic polymer film transducer system. *NDT and E International*, 31(1):51–64, 1998.

[133] M. Hill, Y. Shen, and J.J. Hawkes. Modelling of layered resonators for ultrasonic separation. *Ultrasonics*, 40(1-8):385–392, 2002.

[134] M. Hill, R.J. Townsend, and N.R. Harris. Modelling for the robust design of layered resonators for ultrasonic particle manipulation. *Ultrasonics*, 48(6):521–528, 2008.

[135] B.A. Auld. *Acoustic fields and waves in solids*, volume 1. Robert E.Kreiger Publishing Company, Malabar, FL, 1990.

[136] H. Lamb and S.H. Lamb. *Hydrodynamics*. Cambridge Univiversity Press, 1997.

[137] T.G. Leighton. *The acoustic bubble*. Academic Press, London, 1997.

[138] W. Lauterborn. Numerical investigation of nonlinear oscillations of gas bubbles in liquids. *The Journal of the Acoustical Society of America*, 59(2):283–293, 1976.

[139] A.A. Doinikov. Equations of coupled radial and translational motions of a bubble in a weakly compressible liquid. *Physics of Fluids*, 17:128101, 2005.

[140] R. Mei, J.F. Klausner, and C.J. Lawrence. A note on the history force on a spherical bubble at finite reynolds number. *Physics of fluids*, 6:418–420, 1994.

[141] J. Magnaudet and D. Legendre. The viscous drag force on a spherical bubble with a time-dependent radius. *Physics of fluids*, 10(3):550–554, 1998.

[142] C. Pozrikidis. *Boundary integral and singularity methods for linearized viscous flow*. Cambridge University Press, 1992.

[143] F. Takemura, S. Takagi, J. Magnaudet, and Y. Matsumoto. Drag and lift forces on a bubble rising near a vertical wall in a viscous liquid. *Journal of Fluid Mechanics*, 461:277–300, 2002.

[144] J. Magnaudet, S. Takagi, and D. Legendre. Drag, deformation and lateral migration of a buoyant drop moving near a wall. *Journal of Fluid Mechanics*, 476(1):115–157, 2003.

[145] F. Takemura and J. Magnaudet. The transverse force on clean and contaminated bubbles rising near a vertical wall at moderate reynolds number. *Journal of Fluid Mechanics*, 495:235–253, 2003.

[146] F. Takemura, J. Magnaudet, and P. Dimitrakopoulos. Migration and deformation of bubbles rising in a wall-bounded shear flow at finite reynolds number. *Journal of Fluid Mechanics*, 634:463, 2009.

[147] M. Strasberg. The pulsation frequency of nonspherical gas bubbles in liquids. *The Journal of the Acoustical Society of America*, 25:536–537, 1953.

[148] E.M.B. Payne, S.J. Illesinghe, A. Ooi, and R. Manasseh. Symmetric mode resonance of bubbles attached to a rigid boundary. *The Journal of the Acoustical Society of America*, 118:2841–2849, 2005.

[149] A. Doinikov, L. Aired, and A. Bouakaz. Dynamics of a contrast agent microbubble attached to an elastic wall. *IEEE Transactions on Medical Imaging*, 31(3):654–662, 2011.

[150] A. Francescutto and R. Nabergoj. Pulsation amplitude threshold for surface waves on oscillating bubbles. *Acustica*, 41:215–220, 1978.

[151] X. Yang and C.C. Church. A model for the dynamics of gas bubbles in soft tissue. *The Journal of the Acoustical Society of America*, 118:3595–3606, 2005.

[152] A.O. Maksimov. Viscous streaming from surface waves on the wall of acoustically-driven gas bubbles. *European Journal of Mechanics-B/Fluids*, 26(1):28–42, 2007.

[153] W. Kern and D.A. Puotinen. Cleaning solutions based on hydrogen peroxide for use in silicon semiconductor technology. *RCA review*, 31(2):187–206, 1970.

[154] R.A. Bowling. An analysis of particle adhesion on semiconductor surfaces. *Journal of the Electrochemical Society*, 132:2208, 1985.

[155] J.N. Israelachvili. *Intermolecular and surface forces*. Academic press, 2011.

[156] H.C. Hamaker. The london van der waals attraction between spherical particles. *Physica*, 4(10):1058–1072, 1937.

[157] D. Tabor. Surface forces and surface interactions. *Journal of Colloid and Interface Science*, 58(1):2–13, 1977.

[158] R.A. Bowling. A theoretical review of particle adhesion. *Particles on surfaces*, 1:129–155, 1988.

[159] R.S. Bradley. The cohesive force between solid surfaces and the surface energy of solids. *The London, Edinburgh, and Dublin Philosophical Magazine and Journal of Science*, 13(86):853–862, 1932.

[160] B.V. Derjaguin, V.M. Muller, and Y.P. Toporov. Effect of contact deformations on the adhesion of particles. *Journal of Colloid and interface science*, 53(2):314–326, 1975.

[161] K.L. Johnson, K. Kendall, and A.D. Roberts. Surface energy and the contact of elastic solids. *Proceedings of the Royal Society of London. A: Mathematical and Physical Sciences*, 324(1558):301–313, 1971.

[162] V.M. Muller, V.S. Yushchenko, and B.V. Derjaguin. On the influence of molecular forces on the deformation of an elastic sphere and its sticking to a rigid plane. *Journal of Colloid and Interface Science*, 77(1):91–101, 1980.

[163] M. Soltani and G. Ahmadi. On particle adhesion and removal mechanisms in turbulent flows. *Journal of adhesion science and technology*, 8(7):763–785, 1994.

[164] H.J. Butt, B. Cappella, and M. Kappl. Force measurements with the atomic force microscope: Technique, interpretation and applications. *Surface Science Reports*, 59(1):1–152, 2005.

[165] M.G.L. Gustafsson. Surpassing the lateral resolution limit by a factor of two using structured illumination microscopy. *Journal of Microscopy*, 198(2):82–87, 2000.

[166] H. Shroff, C.G. Galbraith, J.A. Galbraith, and E. Betzig. Live-cell photoactivated localization microscopy of nanoscale adhesion dynamics. *Nature methods*, 5(5):417–423, 2008.

[167] G.B. Whitham. *Laminar boundary layers*. Oxford University Press, 1963.

Publications

Some of the material presented in this thesis has been published. The details of publications are listed as follows.

Peer-reviewed journal

Xiaoyu Xi, Frederic B. Cegla, Michael Lowe, Andrea Thiemann, Till Nowak, Robert Mettin, Frank Holsteyns, Alexander Lippert. 'Study on the bubble transport mechanism in an acoustic standing wave field'. *Ultrasonics* 51(8):1014-1025, 2011.

Xiaoyu Xi, Frederic B. Cegla, Robert Mettin, Frank Holsteyns, Alexander Lippert. 'Collective bubble dynamics near a surface in a weak acoustic standing wave field'. *The Journal of the Acoustical Society of America*, 132(1):37-47, 2012.

Xiaoyu Xi, Frederic B. Cegla, Robert Mettin, Frank Holsteyns, Alexander Lippert. 'Study of bubble dynamics near a surface in an acoustic standing wave field'. *submitted to Physical Review E* , 2012.

Xiaoyu Xi, Frederic B. Cegla, Robert Mettin, Frank Holsteyns, Alexander Lippert. 'Role of the microstreaming on the ultrasonic cleaning in a weak acoustic standing wave field'. *submitted to Applied Physics Letters* , 2012.

Conference presentation

Xiaoyu Xi, Michael Lowe, Frederic B. Cegla, 'Study on bubble trajectories in an acoustic standing wave field'. *10th Anglo-French Physical Acoustics Conference, Fréjus, France*, January, 2010.

Xiaoyu Xi, Frederic B. Cegla, 'Study of bubble behavior near a solid surface in an acoustic standing wave field'. *International Congress On Ultrasonics, Edited by B.B.J.Linde, A.Markiewicz, N.Ponikwicki, University of Gadansk Publishing,*

Gadansk, September, 2011.

Robert Mettin, Philipp Frommhold, Xiaoyu Xi, Frederic B. Cegla, Alexander Lippert, Frank Holsteyns 'Acoustic bubbles: Control and interaction with particles adhered to a solid substrate'. *11th International Symposium on Ultra Clean Processing of Semiconductor Surfaces, Ghent, Belgium.*, September 2012.